Design of Resilient Silicon-Carbon Nanocomposite Anodes

A Dissertation Presented to the Faculty of the
Georgia Institute of Technology

By
Benjamin J. Hertzberg

In fulfillment of the requirements for the Degree of
Doctor of Philosophy in the School of Materials Science & Engineering

Georgia Institute of Technology
November 2011

Design of Resilient Silicon-Carbon Nanocomposite Anodes

Approved By:

Dr. Gleb Yushin
School of Materials Science & Engineering
Georgia Institute of Technology

Dr. Preet Singh
School of Materials Science & Engineering
Georgia Institute of Technology

Dr. Faisal Alamgir
School of Materials Science & Engineering
Georgia Institute of Technology

Dr. Alexander Alexeev
School of Mechanical Engineering
Georgia Institute of Technology

Dr. Paul Kohl
School of Chemical & Biomolecular Engineering
Georgia Institute of Technology

ACKNOWLEDGEMENTS

First, I would like to thank my parents, Daniel Hertzberg and Barbara Kantrowitz, for their unyielding emotional support, both in my academic career and in my personal life. Without their help, I would certainly not have been able to accomplish any of my current achievements. Above all others, I would like to dedicate this work to them.

I would also like to thank my advisor, Professor Gleb Yushin, for his support of my research, his ideas and experience, his patience, and his encouragement. His guidance helped me throughout my work on this thesis, and I am grateful for the opportunities he gave me to cooperate with other researchers in his lab. I appreciate the help given to me by the rest of my thesis committee – Professors Faisal Alamgir, Paul Kohl, Preet Singh, and Alexander Alexeev. I am thankful for their encouragement, their hard questions, and the tremendous role they have played in my education. I am also grateful to my NASA advisor, Concha Reid, for the support she and the rest of NASA's Space Power division gave me in the pursuit of my thesis.

My sincere thanks goes out to the rest of my labmates at the Yushin group – Yair Korenblit, Alexander Magasinski, Igor Kovalenko, Lu Wei, James Benson, Kara Evanoff, Sofiane Boukhalfa, and all of the other students who have worked with us. I appreciate all of the hard work they have done assisting me in my work, and that they have given me the opportunity to cooperate with them on their own projects. I am also grateful for the help and patience of the MSE administrative staff, without whom my work would have impossible. Finally, I would like to thank my friends, Peter Kingston, Greg Phillips, Giuseppe Brunello, Robert Rettew, Kalman Spiegel, and Bennett Williamson. Without their support and friendship, I would have been lost.

TABLE OF CONTENTS

LIST OF FIGURES

SUMMARY

Si-based anodes have recently received considerable attention for use in Li-ion batteries, due to their extremely high specific capacity – an order of magnitude beyond that offered by conventional graphite anode materials. However, during the lithiation process, Si-based anodes undergo extreme increases in volume, potentially by more than 300 %. The stresses produced within the electrode by these volume changes can damage the electrode binder, the active Si particles and the solid electrolyte interphase (SEI), causing the electrode to rapidly fail and lose capacity. These problems can be overcome by producing new anode materials incorporating both Si and C, which may offer a favorable combination of the best properties of both materials, and which can be designed with internal porosity, thereby buffering the high strains produced during battery charge and discharge with minimal overall volume changes.

However, in order to develop useful anode materials, we must gain a thorough understanding of the structural, microstructural and chemical changes occurring within the electrode during the lithiation and delithiation process, and we must develop new processes for synthesizing composite anode particles which can survive the extreme strains produced during lithium intercalation of Si and exhibit no volume changes in spite of the volume changes in Si. In this work we have developed several novel synthesis processes for producing internally porous Si-C nanocomposite anode materials for Li-ion batteries. These nanocomposites possess excellent specific capacity, Coulombic efficiency, cycle lifetime, and rate capability. We have also investigated the influence of a range of different parameters on the electrochemical performance of these materials, including pore size and shape, carbon and silicon film thickness and microstructure, and binder chemistry.

1. Motivation and Impact Statement

Energy technology is a critically important field of research. Environmentally and economically sustainable power generation is now a quickly growing market; the annual demand for wind power, one of the simplest forms of renewable energy, has increased annually by 30% over the past decade, and other renewable energy technologies have experienced similar increases in demand. Since most of these renewable power generation technologies can't be directly used for mobile applications, the development of lightweight, high power stable energy storage technologies is essential. Batteries, as one of the better-developed power storage systems available, are a heavily researched field in energy storage technology. The use of batteries in electric and hybrid electrical cars and buses will minimize fossil fuel consumption, reduce air pollution and reduce potential economic instabilities caused by fossil fuel shortages. Advanced battery technology is also useful for a wide variety of commercial applications beyond renewable energy, including the aerospace and defense industries. Every ounce saved by lowering the battery weight lowers the cost of a launch and allows more mass and volume on the aerial vehicle for other systems required for launch or for payloads. Some applications may require very high specific energy; others may have less strict requirements for specific energy, but demand long cycle life. It is vital that we develop more sophisticated battery technology.

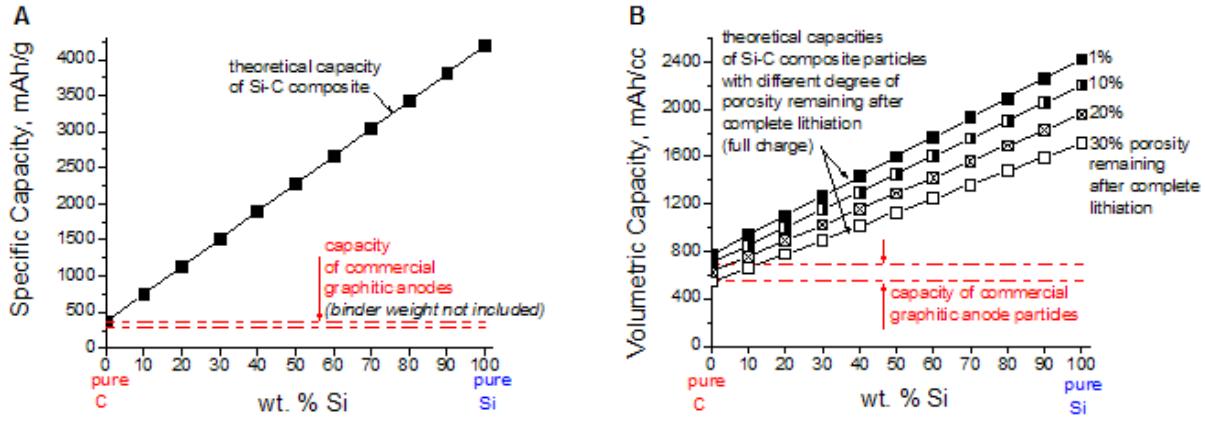

Figure 1.1. Theoretical (A) specific and (B) volumetric capacity of Si-C nanocomposite anodes as a function of weight % Si, as compared to commercial-grade graphitic anode material

Li-ion batteries have proven to be particularly attractive for high power / high energy applications. One of the promising routes to further improve the specific energy of these batteries is to develop high capacity anode materials. Commercial anodes use graphite as lithium host material and offer capacity in the 300-350 mAh/g range. However, other materials that alloy with lithium offer higher capacity. Silicon, for example, possesses a dramatically greater theoretical capacity, at 4200 mAh/g. Unfortunately, pure silicon's experimentally observed high irreversible capacity and short cycle life renders its usefulness limited. The development of novel Si-C nanocomposites may be able to overcome the limitations of pure Si and offer significant improvements in both the specific capacity and the volumetric capacity over commercially used graphite (see Figure 1.1) Si-C nanocomposites combine the excellent mechanical, electrochemical and electrical properties of carbon with the superior lithium intercalation ability of silicon. By performing systematic studies on the influence of various structural factors in Si-C composite particles on their lithium intercalation ability and cycle life, we have contributed to the development of novel high-power lightweight Li-ion batteries.

2. Literature Review

2.1 History of Lithium-ion Batteries

Lithium-ion (Li-ion) batteries have many advantages compared to older nickel-cadmium or lead-acid batteries. They exhibit an extremely high energy-to-weight ratio, and do not suffer from the 'memory effect' common to other types of batteries, where the battery loses capacity as it is repeatedly charged and discharged. They also possess an excellent specific capacity and a high open circuit potential. These properties make them useful not only for consumer electronics, but for defense, automotive and aerospace applications as well. The design of the battery components, such as the anode, cathode and electrolyte, has a dramatic effect on the battery performance, and the selection of the materials for these components has influenced the design and the performance of Li-ion batteries over time. In order to understand the need for advanced nanocomposite anodes, we must first examine the history of Li-ion batteries.

Li-ion batteries were first proposed in the 1970s, by M.S. Whittingham, then a researcher at Exxon. Dr. Whittingham developed batteries that used a titanium disulfide (TiS_2) cathode and a lithium metal anode, based on the intercalation of lithium into the cathode.[1] These batteries achieved a capacity of 480 Wh/kg, performance comparable to that of irreversible lithium

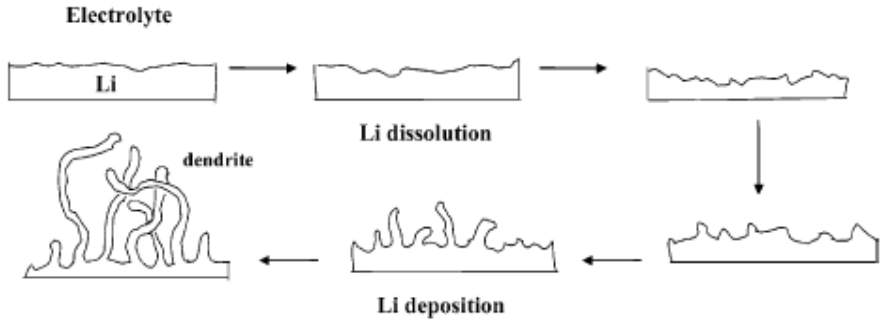

Figure 2.1. Schematic depiction of the growth of dendritic crystals on a Li surface, as the electrode repeatedly charges and discharges. [1]

primary batteries. This discovery unlocked many potential energy storage technologies, which researchers attempted to pursue. However, dendrites formed on the Li surface due to the repeated removal and deposition of Li ions during battery charge and discharge. The mechanism for dendritic formation is shown in Figure 2.1, above. As lithium is repeatedly removed from and deposited on the lithium metal electrode, it is not deposited evenly on the surface of the anode, and this disparity in deposition causes dendrites to form. This effect significantly limited the lifetime of these batteries. [1, 3] In addition, metallic Li exhibits combustion risks in general use, due to its extreme reactivity. Eventually, Li foil anodes were replaced by graphite anodes. Graphite serves as a reversible host for Li ion intercalation/deintercalation, avoiding the formation of dendrites. While the existence of a range of lithium-graphite intercalation compounds had been known since 1955 [4], it was not until 1982 that the technology for using graphite as an anode was developed, by RR Agarwal. These cells used a molten salt electrolyte, impractical for commercial applications, but were otherwise similar to the cells currently in general use. [5] In 1983, J. Goodenough was able to demonstrate the intercalation of lithium into manganese spinels, crystals exhibiting a specialized cubic close-packed crystalline lattice, which could then be used as a safe cathode material. These cathodes, composed of Mn_2O_4 and Mn_3O_4, proved themselves superior to TiS_2 due to their low cost, high electronic and ionic conductivity, and excellent structural stability. [6] With the combination of these technologies, the modern lithium-ion battery became possible.

2.2 Materials of Lithium-ion Batteries.

2.2.1. Electrolyte

A wide range of procedures were developed in the search for optimal methods for preparing lithium-ion batteries. The cathode, anode and electrolyte material must all be optimized. This optimization must balance the demands of high power capacity and low irreversible capacity with those of safety and low cost of manufacture for successful commercialization.

Extensive research has been performed, investigating the optimization of the electrolyte, which is typically composed of a Li salt dissolved in organic solvents. One important quality of the electrolyte is its ability to produce a passivating solid-electrolyte interface (SEI). Useful intercalation is only possible if the anode is well protected by a passivating film, formed at higher potentials than the graphite intercalation potential. If a SEI is not formed, the organic solvent can be decomposed at the anode during charging, reducing the conductivity of the electrolyte. In the field of liquid electrolytes, a wide range of solutes and solvents have been investigated.

The electrolyte salts, which provide Li ion transport, have been the subject of extensive investigation. Any such solute must be able to completely dissociate in the solvent used, move within the solute easily, resist oxidative decomposition at the cathode, and be inert to the various components of the battery, particularly the separator and cell packaging material. Only a handful of lithium salts meet these requirements, particularly those of high solubility and ionic mobility. The primary salts under investigation are $LiPF_6$, $LiBF_4$, $LiAsF_6$, and $LiClO_4$.

Lithium perchlorate ($LiClO_4$) was found to form a SEI with a lower impedance that that formed by $LiPF_6$ or $LiBF_4$ electrolytes, due to the lack of highly resistive LiF in the interface layer. This makes it an excellent electrolyte under controlled circumstances. [7] However, when oxidized, $LiClO_4$ produces Cl^- ions, which violently react with other organic species, including

the electrolyte solvent at high temperatures or current rates. This makes $LiClO_4$ impractical for commercial applications. [2]

Lithium hexafluoroarsenate ($LiAsF_6$) offers excellent lithium cycling efficiencies, more than 95%, considerably greater than what is possible with $LiClO_4$.[8] Unfortunately, the initial cycles of the intercalation process tend to produce reduced As^{3-}, which are highly toxic and harmful to the environment.[9]

Lithium tetrafluoroborate, $LiBF_4$, is much less toxic than $LiAsF_6$ and less dangerous than $LiClO_4$. However, it provides only moderate ionic mobility, producing poor lithium cycling efficiency, as well as substantial irreversible capacity losses.[10] However, for selected battery applications requiring operation at low temperatures, $LiBF_4$ might still be attractive. [11]

Lithium hexafluorophosphate ($LiPF_6$) combines some of the better aspects of all of the previously mentioned salts: the safety and non-toxicity of LiB_4, with the higher conductivity and better overall performance of $LiAsF_6$ and $LiClO_4$. Its combination of useful properties makes it the obvious choice for commercial lithium-ion batteries in spite of its formation of harmful compounds upon contact with water.[12, 13]

Many studies were also launched to optimize the solvent used in these batteries. This solvent must be able to dissolve the electrolyte salt completely, have a high facility for ion transport (by having a low viscosity) in a wide temperature range, and be safe and inert to all of the cell components. We must also consider the solvent's reactivity with the anode and cathode; if the chemical potential of the electrode reduction and oxidation reactions are high enough, the electrolyte will react with the electrode, decomposing and reducing the efficiency of the cell. Since higher reaction potentials improve cell performance, electrolytes which produce a passivating layer – the solid-electrolyte interface (SEI) are preferred. Without this passivating

layer, high irreversible capacity losses and anode degradation are inevitable. Additionally, since the most useful electrolyte salts are polar, a polar solvent must be selected. [14]

Carbonates, and in particular cyclic diesters, are believed to be the most promising solvents, due to their exceptional ability to form a solid-electrolyte interface and excellent ability to dissolve a wide variety of lithium salts, compared to other polar solvents.[15] The earliest subject of this investigation was propylene carbonate (PC), but its use resulted in poor battery efficiency – less than 85% – and a high degree of irreversible capacity, due to its inability to form a stable SEI.[7, 16, 17]

Ethylene carbonate (EC) is similar in composition and structure to PC, but its greater degree of molecular symmetry allows it to form a stable crystalline lattice.[18] EC's effectiveness in the creation of an effective SEI with high degree of reversibility was established in 1990.[19] The addition of the PC to EC depresses the normally high melting point of EC, allowing the electrolyte to exist as a liquid at room temperature. The addition of other solvents, such as dimethyl carbonate (DMC), can further improve its fluidity at low temperatures.[20] These mixed (EC:DMC:PC) solvent electrolytes benefit from increased electrochemical stability, high reversible capacity, fast ion transport and a low freezing point.[21, 22]

Electrolyte additives can further improve the performance of these solutions. Additives can improve the formation of the SEI, protect the cathode, stabilize the $LiPF_6$ salt in the solution, or further improve the stability and safety of the cell.[23] Additives intended to promote the formation of the SEI must help produce an ionically and electrically insulative polymer layer, with sufficient micropores to ensure the diffusion of lithium into the electrode. The most successful SEI forming additives are either polymerizable monomers possessing one or more carbon-carbon double bonds or reductive agents, whose products are adsorbed onto active sites

on the electrode surface. The most effective reductive agents are primarily sulfur-based, such as polysulfide, SO_2, or various sulfite compounds. Vinylene carbonate is one of the most effective polymerizable monomer additives, although various furan compounds have also proven effective.[24, 25] Monomers used as electrolyte additives must efficiently polymerize, and the polymers produced must have high solubility and adhesion. [23]

2.2.2. Cathode

The cathode material is also of great importance. Most of the research on Li-ion batteries has focused on improving the quality of the cathode material. Any such cathode material must be able to intercalate large amounts of Li, extract Li without irreversible capacity losses, possess good ionic and electronic conductivity, and remain electrochemically stable, even at high voltages. It should also remain structurally stable during intercalation and deintercalation, regardless of any volume changes involved. An example of open-circuit voltage performance of an appropriate cathode material is shown below, in Figure 2.2. The high voltage vs. Li of this cathode material allows for high amounts of energy to be stored in batteries that use it. As lithium is intercalated, the crystalline structure of the cathode changes from primarily cubical to primarily tetragonal. Changes such as these demand structural stability. [26]

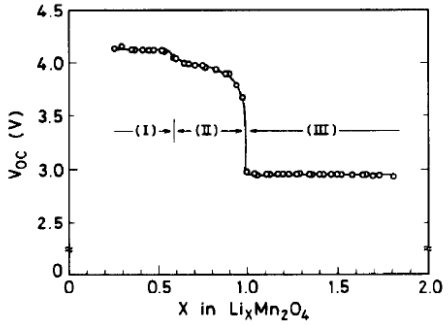

Figure 2.2: Open-circuit voltage of $Li_xMn_2O_4$ as a function of x; note change in crystal structure at x = 1.0 and ensuing change in V_{OC}. [2]

The two most common types of cathode materials in use are layered materials, such as lithium cobaltate ($LiCoO_2$) or titanium disulfide (TiS_2), and materials with a more open structure, such as spinels. The former have superior intercalation capacity, while the latter have a reduced cost.[26] One of the first Li-ion battery cathodes, TiS_2, is a semiconductor, and therefore moderately conductive without any additives. In addition, it forms a solid solution with lithium, with full reversibility of intercalation possible. Like graphite, TiS_2 has a hexagonal close-packed lattice based on S ions, though the octahedral sites are occupied by Ti ions. This material must be highly ordered, to maximize its Li intercalation ability, as the Li ions are intercalated into the unoccupied interstitial sites. $LiCoO_2$ and $LiNiO_2$, used later on, have a similar structure but are capable of intercalating considerably more Li, and have a significantly higher potential, thereby storing more energy. A research team headed by J. Goodenough discovered that CoO_2 could intercalate Li electrochemically and that that Li could then be removed efficiently.[27] Subsequently, a team lead by G.G. Amatucci discovered in 1996 that, when fully intercalated, $LiCoO_2$ assumes a face-centered cubic lattice, even though it occupies a hexagonal close-packed configuration similar to TiS_2 once the Li has been fully removed. These phase changes limit the rate of Li intercalation, produce poor stability at low Li contents. They also cause conductivity changes, which further limits the power delivery capability of the batteries.[28, 29] These factors, combined with the cost of cobalt, have driven the development of alternative cathode materials based on more open structures than layered oxides like $LiCoO_2$, such as spinels.

Mn_2O_4 spinel was first investigated as a Li-ion battery cathode material by a team headed by M. Thackeray in 1983, it showed great promise, due to its low cost, consistently good electronic and ionic conductivity, and a highly stable three-dimensional structure. xlix The

material can survive repeated intercalation of Li without disintegration by intercalating Li ions into the tetrahedral interstitial sites. It can also intercalate a second Li ion into the octahedral sites, though the distortion frequently produces a phase change to a rock salt structure. This material tends to exhibit capacity fade, which may be caused by the oxidation of the manganese atoms from Mn^{4+} to Mn^{3+}, potentially causing migration from the cathode to the anode and preventing further Li intercalation, thereby creating significant irreversible capacity and reducing the cyclability of the battery. However, this problem can be overcome by chemically modifying the material, converting it to $LiMn_{2-y}M_yO_4$, where M is Cr, Co, Ni, or Cu, or by coating it with a metal oxide layer, such as V_2O_5, $LiCoO_2$, or Al_2O_3. These modifications can reduce the dissolution of manganese into the electrolyte, preventing the migration of the material.[30]

Another promising cathode material is the polyanion-based $LiFePO_4$. This material is a phospho-olivine (a Li metal phosphate with an olivine structure), and is capable of lithium intercalation at a high capacity. This material was first developed by a team headed by A.K. Goodenough in 1997.[31] Significantly, the material is capable of Li intercalation without any loss of capacity over hundreds of cycles, and produces an even higher voltage than an oxide-based cathode could. Li ions are stored in the interstitial sites between crystal cells, rather than within the crystal cells themselves. The olivine structure possesses one-dimensional channels which enable the easy diffusion of lithium ions through the cathode. Once the Li atoms have been removed electrochemically, this produces a shift in crystal structure from the orthorhombic structure of fully intercalated $LiPO_4$ to the trigonal quartz-like structure of $FePO_4$. Despite this phase change, the material's intercalation process is fully reversible.[32] With an even higher capacity than $LiCoO_2$ and considerably greater cost-efficiency and safety of use, $LiFePO_4$ is the

most effective currently utilized Li-ion battery cathode material, used in any application where safety and high capacity are paramount.

2.2.3. Anode

The anode material is also of great importance, but considerably less effort has been put into the development of novel anodes. State of the art commercial batteries still use the same material for anodes as the first batteries introduced on to the market – graphite.[33, 34] Graphite anodes are capable of intercalating a substantial amount of lithium, with a theoretical capacity of ~372 mAh/g, which corresponds to 1 Li per 6 C atoms. In selected graphitic anode materials, performance of up to ~350 mAh/g can be attained. Graphitic anodes demonstrate minimal fading with cycling, form a good solid-electrolyte interface, and intercalate Li without dangerous expansion or phase changes. A wide variety of graphitic carbons have been used as anodes. Their performance was found to depend on their microstructure, texture, crystallinity, and morphology. The lithium ions intercalate into the void space between close-packed graphite planes; as a result, the ability of the graphite to intercalate lithium is limited by its crystallinity. If the graphite has a reduced degree of crystallinity, it will have less close-packed graphite planes and therefore be more limited in its ability to intercalate lithium.[34]

A team led by C. Lampe-Onnerud found that the crystallinity of the material influenced its capacity significantly, but in unpredictable ways. Moderately crystalline graphites, with a crystal size below 20 nm, exhibited high capacity and minimal losses with cycling. At the same time graphite flakes, with a much larger crystal size (>100 nm) only initially exhibited high capacity but after the 20^{th} cycle started to quickly lose discharge capacity. The capacity fading can be explained by the further mechanical exfoliation of the flakes by the slow insertion of the solvent molecules between the graphene layers during the rapid diffusion of Li ions along the

long grains in the charge process.[35] A team led by M. Endo investigated the effects of crystallinity and found that graphites with a crystal size greater than 20 nm or less than 3 nm exhibited the best performance. The study implied that two different intercalation processes, one that operates best at low levels of crystallinity and one that operates best in more crystalline samples, are at work in graphitic crystals of different crystal sizes. As a result, at intermediate sizes, neither process is capable of going to completion, causing the capacity to be at a minimum. This team also analyzed the effects of morphology on the performance of carbon fiber anodes. Heat-treated carbon fibers tend to exhibit a plate-like structure in the center, with graphene planes arranged semi-parallel to each other, and with more irregularly arranged planes surrounding these samples. Untreated carbon fibers tend to exhibit a more layered structure. The radially aligned structures of the heat-treated fibers tend to exhibit superior electrochemical properties; this suggests that the exposure of additional edge planes to the electrolyte facilitates the intercalation of lithium.[36]

Recently, extensive research has gone into developing of pure metals (such as Al, Mg, Sn and others) or semiconductors (such as Si or Ge) as anode materials. Such materials possess substantially higher volumetric and gravimetric capacity than purely graphitic anode materials. Developing batteries with superior capacity can potentially unlock new applications in a wide variety of fields, including aerospace and automotive technologies. Si in particular has great potential, having a theoretical capacity of 4200 mAh/g (up to 22 Li atoms per 5 Si atoms), more than 10 times that of graphite.

Research on this topic began in the early 70s, when several research groups analyzed the intercalation reactions of a variety of pure metals with lithium. One of the most promising of these early investigations was that lead by S.C. Lai, and published in 1977. The research focused

on a molten salt Li-Si battery anode, and uncovered the range of Li-Si alloys produced by intercalation and the amount of energy involved with each phase transformation, as well as the reversibility of the transformation. This investigation revealed the high energy density potential of a Li-Si battery, sparking interest in the development of Li-Si batteries.[37] Unfortunately, the challenges of maintaining mechanical integrity of the Si electrodes due to the dramatic expansion of the material during battery operation were soon realized to be the major obstacle towards commercialization of this technology. When Si is fully intercalated with lithium, the numbers of atoms present increases 440%, and consequently the volume of particles increases by approximately 4 times, producing substantial stresses within the material.[38]

Extensive research has been done to analyze the source of the failure experienced by a pure silicon anode. An investigation, published in 2004 and lead by J.H. Ryu, found that the Li deintercalation from the lithiated Si particles produces a dramatic increase in resistance, of more than an order of magnitude from the minimum resistance of the intercalation process. This prevents the complete deintercalation of lithium from the electrode, leading to irreversible capacity losses.[39] Several mechanisms were suggested to contribute to the observed conductivity losses within the electrode, such as the pulverization of macroscopic Si particles due to the uncompensated stresses exceeding the fracture toughness of the material and the failure of the polymer binder to maintain anode integrity during the discharge and the resulting particle shrinkage, leading to the loss of the electronic contact between the particles.

It is possible to partially overcome this problem by using a conductive additive, such as nano-scale carbon black, which improves the de-alloying kinetics and prevents the agglomeration of Si particles. The additive can also somewhat reduce the impact of expansion and contraction on the binder matrix by buffering the mechanical stresses produced.[20] An

alternative method for improving the capacity is to reduce the Si particle size to nanoscale proportions; this substantially reduces the increase in mechanical stresses and contact resistance. A study published by W.R Liu in 2005 found that reducing the size of the particles from 20 μm to 3 μm significantly improved the performance of the anode, though the capacity remained low.[40] Other recent studies have indicated that the thickness of the crystalline sample has a tremendous impact on the cyclability of the material. A study published by Ohara et al. in 2004 demonstrated the impact of thin film thickness: when analyzing a flat Si thin film deposited on copper, a reduction in thickness from 150 nm to 50 nm reduced the rate of capacity loss by a factor of more than 10. This strongly suggests an upper limit to the size of particles or films to avoid disintegration during the process of Si intercalation and deintercalation.[41]

A study by Huggins and Nix, published in 2000, establishes a model that explains this behavior. It suggests that particles must have a size under a certain critical radius, dependent on the degree of intercalation to be recovered from. At smaller particle sizes, the strains produced by intercalation can be accommodated elastically, rather than by plastic deformation, allowing for the full recovery of the original, stable structure. For full intercalation (to $Li_{22}Si_5$) the critical size is 60 nm. This explains the results of the Ohara study, cited above.[42] The critical size below which fracture does not occur varies as a function of the degree of lithiation (represented here as the strain parameter e, the degree by which the anode particle expands during lithiation) and the ratio of the fracture toughness to the biaxial elastic modulus K/B is shown in Figure 2.3 below. We see that the critical particle size decreases dramatically at small degrees of lithiation, but that the decrease in the critical size is smaller once the anode particle approaches full lithiation. [42]

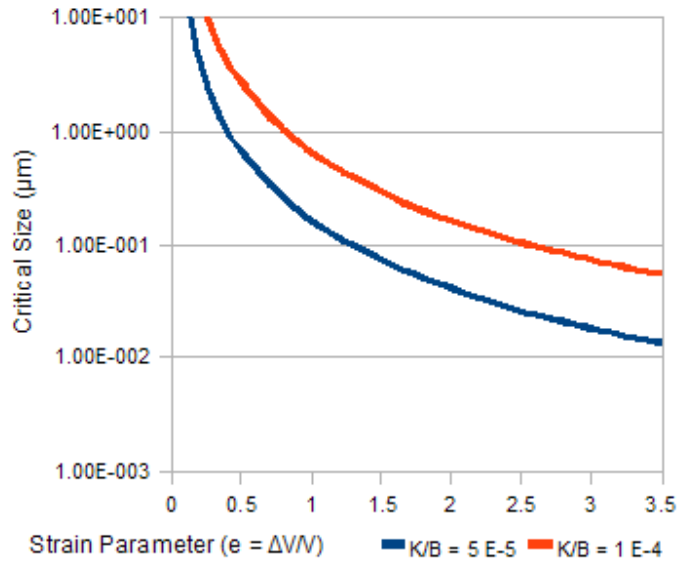

Figure 2.3: Effect of final alloy composition, as defined by strain parameter of lithiated alloy, and ratio of fracture toughness to elastic modulus, on critical particle size required to prevent fracture, h_c.

These methods, while effective in improving the cyclability of the anode material, ultimately do not exploit the full potential of silicon's high intercalation capacity. Even with a conductive additive, silicon particles can generally achieve less than half of the theoretical capacity; in the case of microparticles, 20-25% is more common.[20] While Si nano-particles reduce fading somewhat, their expansion still disrupts their electrical contact with the binder around them, causing a rapid loss of capacity. Thin films, while providing both high capacity and cyclability, impose significant restrictions on the gravimetric capacity of the battery itself, since the total capacity of the anode will be relatively small.[40] New approaches are needed to substantially improve the capacity of the battery anode.

One possibility for improving the performance of the anode is to use a structured composite particle as the anode material. Si-C composites have thus far produced the best results, due to the softness and compliance of C, which allows the composite particle to change shape

and size without failure. C also possesses the ability to intercalate Li into itself without serious expansion, and is highly conductive. Combining the properties of the two materials can yield superior results compared to the results of either material by itself. These composite materials can be produced by pyrolysis or chemical vapor deposition (CVD), by ball or mechanical milling, or by some combination of these methods. Ball milling gives the advantage of ensuring homogeneity throughout the sample, as well as giving control of structure, particle size and composition. The earliest ball milling composite materials were produced by a team lead by Wang, which published its results in 1998. These materials were produced by the milling of graphite and silicon followed by mixing the resulting powder with PTFE to produce an anode. This process created nano-Si particles encapsulated in amorphous carbon. However, these composites were unable to charge up to their full theoretical capacity and maintain stability, and showed a very high irreversible capacity due to the disintegration of the Si active mass and the irreversible insertion of Li.[43] Other, similar attempts at producing composite anode materials through ball milling also failed, as they were unable to accommodate the microstructural changes produced through cycling, leading to fading and eventual failure of the anode.[44]

The earliest pyrolysis-based composite materials were produced by the thermal decomposition of complex silane-based polymers at very high temperatures. This decomposition produced polymers with capacity above that of carbon by itself, but the reversible capacity was only 550 mAh/g, and a high irreversible capacity was exhibited.[45] Materials produced through high-temperature polymer decomposition tended to be amorphous Si-C-O glasses, with only limited ability to intercalate lithium compared to pure silicon, and additionally with limited conductivity. A conductive additive is necessary in these composites to enable sufficient conductivity.

One effective solution was achieved by the use of nanocomposites produced by the vapor deposition (via pyrolysis of silane gas) of nano-Si particles on graphite. A study published in 2005 by Holzapfel et al. demonstrated the superiority of this approach: the anode produced exhibited more than 900 mAh/g of reversible capacity after 100 cycles, with a fade rate (after the initial formation of the solid electrolyte interface) of less than 1%, and a total irreversible capacity of 26%. The effectiveness of this approach can be attributed to the small size of the nano-Si active particles – less than 50 nm in diameter.[46] Even better results can be achieved by using CVD to coat the particles with a layer of carbon, thereby reducing the capacity loss from the formation of the solid electrolyte interface, and improving the electrical contact with the anode material matrix. A study published by Liu et al in 2005 reinforces this idea: the study found that carbon-coating silicon nanoparticles suppressed capacity fading, both that produced by the increase in contact resistance and by the total mechanical failure of the electrode structure.[47]

Several innovative investigations have examined alternative nanocomposite materials for use in lithium-ion batteries. One common focus of investigation is silicon nanowires. An investigation by C.K. Chan et al in 2007 demonstrated that thin nanowires – below the critical size threshold at which fracture occurs during lithiation – could reversibly intercalate and deintercalate lithium. The anodes used, composed of silicon nanowires grown via a vapor-liquid-solid (VLS) method with gold nanoparticle catalysts, exhibited a much higher reversible capacity than spherical carbon-coated nanosilicon particles, with a reversible silicon delithiation capacity of ~3200 mAh/g at C/20. The nanowires retained their high capacity even at higher cycling rates, with a silicon delithiation capacity of ~2100 mAh/g at C/1. The direct, 1-dimensional nature of the electron transport reduced the impedance of the system, and the spacing between nanowires

permitted easy relief of lithiation stresses. These experiments also demonstrated that silicon nanowires undergo structural changes during repeated lithiation and delithiation, becoming less crystalline, gaining a larger diameter, and developing a rougher surface. Despite the extreme structural changes involved, the nanowires avoided fracture, due to their small size.[48] Manipulating the crystal structure of the nanowires to produce a crystalline core surrounded by an amorphous shell improves the performance of the nanowires, permitting capacity retention of 90% over 100 cycles, with an initial capacity of ~1000 mAh/g. Preventing full lithiation via a voltage cutoff preserves these crystalline cores, improving electronic conduction within the nanowire and preventing dramatic structural changes.[49] While these nanowires present a promising avenue for investigation, and demonstrate the value of internal porosity to a nanocomposite electrode, their cost of production and the cell fabrication and safety issues associated with nanowires present barriers to commercialization.

Binder research has been a major subject of lithium-ion battery research. One potential cause of failure in Li-ion batteries with Si anodes is the failure of the binder due to particle expansion; as previously mentioned, even when nano-Si particles are used which do not fracture during lithiation, the repeated expansion and contraction of the particles will cause the binder to fail, resulting in a loss of electronic contact and a drastic increase in impedance. One of the first investigations of the possibilities inherent in advanced binders was performed in 2005 by Liu et al. The primary binder material used for older anodes was poly-vinylidene-fluoride (PVDF). However, this study found that a mixture of styrene butadiene rubber (SBR) and sodium carboxylmethyl cellulose (CMC) demonstrated significantly superior results. This composite binder was more rigid and tolerated greater degrees of strain, exhibited better adhesion, and absorbed much less solvent. When used to produce an electrode with micro-Si particles, the cell

exhibited a capacity of 800 mAh/g for up to 40 cycles; C-coated μ-Si particles exhibited even better performance, with a capacity of 1000 mAh/g for more than 50 cycles. This improvement in performance was assumed to be the result of the improved strain capacity and adhesion of the composite binder, although the aqueous nature of the binder slurry may have also contributed to its improved performance by more evenly distributing the components of the electrode.[50] A second, later study, specifically focusing on CMC as a binder material was conducted by Li et al in 2007. These cells used μ-Si powder as well, but without a carbon coating. These cells were able to achieve an equivalent capacity for a longer number of cycles – 1000 mAh/g for 70 cycles. Pure CMC binders were demonstrated to have superior performance compared to CMC-SBR composite binders, despite the high stiffness and brittleness of the polymer. No simple explanation was found for the improved capacity retention, efficiency, and reversibility of CMC-based electrodes, but it was suggested that surface modification of the Si active material by the binder might play a part, as such changes to the particles' surface chemistry could improve the quality of the solid-electrolyte interphase (SEI).[51]

Subsequent studies have further experimented with CMC as a binder material. One study, led by Beattie, used mathematical modeling to attempt to derive a way of compensating for the extreme volume expansion of lithiated silicon. It was suggested that cell failure was a result of the movement of the active particles, leading to their electronic isolation from the binder, as a result of their contact with each other during charge and discharge. The study found that in an electrode with sufficiently high binder content (66 vol% binder and conductive additives), the active particles could fully lithiate and delithiate without coming into contact with each other, thereby preventing a loss of electronic contact. This binder was able to achieve up to 350 cycles while retaining capacity over 400 mAh/g. This study confirmed that electronic isolation was a

major factor in electrode failure, and that this problem could be combated by well-tailored binders.[52] Other studies focused on the manipulation of the binder-active particle interface; as suggested previously, the surface chemistry of the binder-Si interface can have a significant impact on cell performance. One study, led by Mazouzi, found that modified aqueous processing could significantly improve the performance of the electrode. Reducing the pH of the aqueous solution used for slurry casting by addition of an acidic buffer (either citric or sulfuric acid) was found to significantly improve the performance of the electrode. The electrode exhibited a discharge capacity of 960 mAh/g for more than 700 cycles. XPS analysis of the buffered and pure slurries demonstrated that the nano-Si in the buffered solution exhibited considerably higher levels of R(O)OSi groups compared to the pure solution. This was concluded to be a product of increased grafting of the Si surface to the carboxyl groups of the CMC, as a result of the acid added to the solution. The increased number of covalent bonds was presumed to be the source of the performance improvement, as increased adhesion between binder and active material could certainly increase the performance of the electrode.[53]

This strongly suggests that the best results for the production of nanocomposite anodes can be achieved by using nano-Si active particles or thin films, using chemical vapor deposition to produce a carbon coating, and by using a tailored binder and electrolyte. Nanocomposite electrodes with internal porosity exhibit the best results. However, there have been very few systematic studies on the effects on the effects of microstructure, morphology, and internal structure on the effectiveness of these particles.

2.3 XPS Characterization of Li-ion Batteries

During the first charge of an Li-ion battery, the liquid electrolyte undergoes reduction at the anode along with Li^+ ions, affecting the character of the cell. This phenomenon was first

discovered by Peled in 1979, when it was determined that nonaqueous electrolytes would become solid at the interface between electrode and electrolyte, while still acting as an electrolyte. This electrolyte layer was found to impact various kinetic and electrical parameters of the cell.[54] Ideally, the decomposed electrolyte forms a stable, passivating layer on the electrode surface, called the Solid-Electrolyte Interphase (SEI). This layer will be composed of both organic and inorganic components, from the organic solvent and the inorganic salts of the electrolyte. In order for the battery to charge and discharge in a stable, efficient fashion, the SEI must prevent further transfer of electrons between the electrode and the electrolyte thereby preventing further electrolyte decomposition while allowing the transfer of ions into the electrode.

As discussed previously, cyclic carbonates have been found to produce an adequate SEI in Li-ion batteries. During initial intercalation of lithium into the SEI, and potentially for several cycles afterwards, the electrolyte and salt are decomposed via several simultaneous complex processes, producing a number of different organic and inorganic components in different layers. A number of different models have been produced to try to understand the composition of the SEI. These models suggest that the dense inner layer is composed primarily of inorganic species produced by salt reduction, while the outer layer is a porous organic or polymeric layer formed by solvent decomposition.[55, 56] When resistance changes in the SEI are measured via electrochemical impedance spectroscopy (EIS), the thickness of the SEI has been found to vary from a few Å to tens or hundreds of Å.[57]

The SEI has a strong influence on both the kinetic and electrical properties of the electrode. A chemically or structurally unstable SEI will lead to continuous decomposition of electrolyte as the SEI flakes off and regenerates cycle after cycle, reducing the efficiency of the

cell significantly.[52] An electrically conductive SEI will cause the continuous growth of the SEI, increasing its ionic impedance dramatically. A SEI with low porosity will also have high impedance. The importance of all of these factors means that producing electrodes which develop a high-quality SEI is essential for optimizing the performance of a Li-ion battery.

One of the major factors causing loss of capacity in Li-ion battery anode materials is the increase in impedance produced by the build-up of thick SEI films. During charge and discharge of nano-Si based electrodes, the lithium lost at each cycle is typically stored in a trapped species at or near the surface of Si grains. These trapped species can accumulate in the pores of the electrode or at the surface of active grains. When these trapped species continue to accumulate cycle after cycle, they can make the SEI thicker and drastically increase the impedance of the cell, reducing its effective capacity. This effect has been demonstrated previously by Guyomard et al. Analysis via electrochemical impedance spectroscopy (EIS) has determined that after a certain number of cycles, the SEI becomes thick enough to significantly impact the polarization of the electrode during lithiation. As the polarization induced by the SEI increases, more lithium-rich phases of silicon fail to form, limiting the cell's capacity. The absence of an increase in polarization during delithiation suggests that the loss of capacity is not produced by a loss of electrical contact, but rather by the increased impedance of the SEI. This hypothesis is reinforced by NMR and SEM analyses of the SEI. Comparison of NMR spectra between lithiation and delithiation showed that the lithium lost at each cycle is trapped at the surface in the form of various lithium-containing species, rather than in the form of Li trapped in disconnected active material particles. SEM analysis showed the electrode to have developed a thick SEI layer, although the electrode itself was intact.[58] The thickness of the SEI must remain stable to avoid a significant increase in the impedance of the cell.

The SEI has a complex structure. The foundational layer of the SEI, and the one that has the greatest role in electrode passivation, is a dense inorganic matrix primarily composed of LiF and Li_2CO_3. This layer is thin, and close to the electrode. Beyond this first layer is a porous layer composed of various polymeric and organic components, such as oxalates and semicarbonates, which tend to be highly soluble and passivate the SEI poorly. Large crystals of LiF may also be interspersed through the SEI.[59] The material is a thin film (typically <10 nm) electrodeposited on the electrode surface, frequently intercalated into the surface of a graphitic carbon electrode. Being virtually impossible to remove intact, the SEI must be analyzed in situ. Analyzing the composition of the SEI is a complex task. Analysis in situ is complicated by the fact that the components of the SEI are highly sensitive to contaminants, humidity, and air. Lithium alkyl carbonates are converted by contact with CO_2 or water to lithium carbonate.[7, 60] Caution must be used to ensure that the sample is not exposed to air before or during analysis.

Surface analysis techniques are typically used in SEI analysis, since the SEI is primarily a surface phenomenon. Spectroscopic methods, including x-ray photoelectron spectroscopy (XPS), Fourier-transform infrared spectroscopy (FTIR), and Raman spectroscopy are the most common. XPS analysis functions by projecting a high-energy beam of X-rays (~1200-1500 eV) onto a sample. The x-ray beam causes core electrons to be ejected as photoelectrons, which are then captured and analyzed on the basis of their energy and rate of ejection from the incident area. Electrons with greater kinetic energy are ejected from orbitals closer to the nucleus. XPS can detect elements as light as lithium in concentrations as low as 0.1 atomic %, with errors of approximately $\pm$10%.[61] As the depth of the volume it measures is limited to 10 nm, XPS is particularly valuable for the examination of SEI, which is rarely thicker than that. XPS is also useful for its ability to measure the chemical state of the elements it analyzes, which are

distinguished in the shifts in electron binding energy produced from a high-resolution scan of the range of energies associated with the C1s orbital, for example, we may distinguish atoms in the C-C, C-O, or C=O chemical states. These properties make XPS ideal for analyzing the properties of the SEI. However, XPS has certain limitations. Due to the highly energetic X-ray beam used for characterization, the SEI may be damaged or chemically altered during analysis. Also, if the composition of the SEI is similar to that of the underlying substrate, distinguishing between the two may be difficult. Furthermore, XPS data analysis is complex it depends upon the deconvolution of complex high-resolution spectra, which demands a sophisticated understanding of the system and good reference values, which are inconsistent throughout the literature.[62] Despite these limitations, we have found XPS to be the most effective method for determining the chemical composition of the SEI.

Deconvolution of high-resolution XPS spectra reveals the presence of multiple peaks, corresponding to different chemical states. The states we have identified, based on a search of the literature, are identified below.

Carbon scan bond states:

Bond Type	Bond Energy (eV)	Properties
C-C	284.3	Graphitic or disorganized carbon
C-OH	286.3	Associated with presence of polymers or oligomers within SEI
C-O	287.8	Associated with lithium alkyl carbonate, lithium carbonate
$C-O_2$	289	Associated with oxalates or semicarbonates
$C-O_3$	291.3	Associated with lithium carbonate
C-F	292	Associated with alginate & poly(acrylic acid) binders

Phosphorus scan bond states:

Bond Type	Bond Energy (eV)	Properties
P-O	135.7-135.0	Associated with range of phosphates
P-F	138.6	Associated with lithium hexafluorophosphate

Fluorine scan bond states:

Bond Type	Bond Energy (eV)	Properties
Li-F	686.2	Associated with lithium fluoride
P-F	688.4	Associated with lithium hexafluorophosphate

Oxygen scan bond states:

Bond Type	Bond Energy (eV)	Properties
C-O	533	Associated with range of different carbon-oxygen bonds; doesn't change depending on bond oxidation state
O-H	535.3	Associated with water, semicarbonates

It can be difficult to distinguish the various carbonaceous components of the SEI from one another. Lithium alkyl carbonate ($ROCO_2Li$) and lithium diethylene carbonate ($(CH_2OCO_2Li)_2$) both contain C-O_3 and C-O bonds, while poly(ethylene oxide) contains both C-OH and C-O bonds. We can distinguish the relative content of these components by measuring the relative content of the various chemical states present – a high ratio of C-OH to C-O states indicates a high content of polymeric species, while a high ratio of C-O_3 to C-O states indicates a high level of lithium carbonate and low levels of $ROCO_2Li$ and $(CH_2OCO_2Li)_2$. [62]

All of these different chemical components will have different effects on the electrochemical performance of the electrode the SEI passivates and the cell as a whole. We will review these components to develop a better understanding of which components best improve

the performance of the SEI. The SEI must passivate the electrode efficiently in order to minimize impedance. Lithium carbonate (Li_2CO_3) has been found to be a highly effective passivating component of the SEI. Li_2CO_3 is produced by the reduction of cyclic carbonate electrolyte components at low potentials predominantly ethylene carbonate. It can also be formed by the reaction of $ROCO_2Li$ compounds with low concentrations (up to several hundred ppm) of H_2O.[63] Li_2CO_3 passivates the electrode surface more effectively than ROCO2Li or other carbonate decomposition products, due to its ability to form networks with other, similar decomposition products. The small organic groups of Li_2CO_3 let it form more complex and more tightly-fitting networks compared to $ROCO_2Li$, which may have larger organic molecules attached to them, preventing the development of complex networks via steric hindrance.[64]

A high content of polymeric species in the SEI can also have a positive effect on the performance of Li-ion batteries. Polymeric species tend to have low steric hindrances, and therefore can form dense, highly passivating films. The impact of the content of polymeric species in the SEI has been studied through analysis of vinylene carbonate (VC) electrolyte additives. When added to the electrolyte, VC deposits poly(VC) radical anions onto the surface of the anode during initial lithiation, which then initiate a polymerization process during the normal SEI formation. This increases the content of polymeric species in the SEI and improves its passivation ability. Cells using vinylene carbonate electrolyte additives in conjunction with graphitic anodes demonstrate significantly improved cycle life, as the additional passivating effect of the polymer-enhanced SEI prevents exfoliation of the graphite and the development of an excessively thick SEI. Vinylene carbonate has similarly beneficial effects when used with other types of anodes.[65, 66]

Lithium fluoride is produced by the decomposition of $LiPF_6$ electrolyte salts, rather than the electrolyte itself. This decomposition can be spontaneous, or can be prompted by interaction with other electrolyte or SEI components. It is typically incorporated into the inorganic underlayer of the SEI. LiF is highly insoluble in typical electrolytes, potentially resulting in strong passivation of the electrode.[67] The impact of LiF on the impedance of the electrode is less clear. In some circumstances, cells with high LiF content may possess low impedance; in other cases, high LiF content is directly correlated to an increase in impedance. The impedance produced by the development of LiF may be a product of their position within the SEI. When LiF is produced on an area of the electrode where lithium is more easily intercalated, such as the edge plane of a highly oriented graphitic electrode material, a significant increase in impedance is likely. When LiF is distributed only to less critical areas of the electrode, the impedance does not significantly increase.[68]

There are a range of potential non-polymeric organic components of the SEI. These include lithium diethylene carbonate, $(CH_2OCO_2Li)_2$ and lithium alkyl carbonate, $ROCO_2Li$. $(CH_2OCO_2Li)_2$ is typically produced via the two-electron reduction of ethylene carbonate (EC), and is found primarily in the SEI of cells using EC-based electrolytes. $ROCO_2Li$ includes a wide range of potential components, such as CH_3OCO_2Li or $C_2H_5OCO_2Li$. These components are typically considered to be produced as a byproduct of two-electron reduction reactions, rather than directly by redox reactions, and can be found in the SEI of any cell using a carbonate-based electrolyte. $(CH_2OCO_2Li)_2$ and $ROCO_2Li$ components are typically present in the highly porous outer layer of the SEI. [39] These organic components are also more likely to dissolve in the electrolyte than inorganic lithium salts, such as LiF or Li_2CO_3. These factors are due to the size and shape of the salt molecule; the larger the size of the salt molecule, the more soluble and less

passivating it becomes, due to the delocalization of electrons. Salt molecules with a linear or planar molecular shape will promote enhanced packing within a crystal lattice, producing reduced dissolution in the electrolyte. $(CH_2OCO_2Li)_2$ and $ROCO_2Li$ components are typically more bulky, producing a greater degree of dissolution. As a result, they tend towards high solubility and poor passivation These materials are therefore more likely to exhibit poor passivation due to their high steric hindrance.[67]

From this information, we can determine the impact of various components on the effectiveness of the SEI as a passivating film. The porous organic outer layer can be considered the least passivating element of the film, due to the high steric hindrance of the components making it up. Due to its high thickness, this layer is likely to create a high impedance, and may be a major contributor to the failure of nano-sized Si anodes. Lithium fluoride is also a potential contributor to the failure of the SEI; while an effective passivating agent, lithium fluoride can contribute to SEI impedance. Lithium carbonate is an excellent passivating agent, which does not appear to contribute a high level of impedance. Polymeric components, similarly, contribute to SEI passivation without dramatically increasing impedance. We can therefore conclude that a highly passivating SEI with low impedance will have a high content of lithium carbonate and polymeric species, with moderate levels of lithium fluoride and minimal quantities of non-polymeric organic species.

3. Project Overview & Goals

3.1 Research Effort Objectives

While calculations and some preliminary data suggest that nanoparticles and nanosized Si coatings below the critical size do not fracture during Li insertion and extraction, the absence of systematic studies has hampered the optimization and widespread use of high capacity anodes. Very little is known as to how and the performance and long-term stability of Si nanoparticles and thin films, and of nano-Si/C composite particles, are affected by various physical parameters. [i] It has been shown that carbon-Si nanocomposites with internal porosity can serve as a high capacity anode. During the anode charging process, the Li ions intercalate with the C and alloy with the amorphous Si, ultimately forming $Li_{22}Si_5$. The alloying process is accompanied by the expansion of the amorphous alloy. Internally porous electrodes permit the overall volume of the particle to remain virtually constant during this process, as the Si expansion is accommodated by the pore space. If the carbon structure is rigid enough, the coating is of optimized morphology and thickness, and the C-Si interface is designed appropriately to withstand the interfacial stresses, the Li insertion process could be fully reversible, such that the extraction of Li from the composite brings the porous particle into the initial state. Without this pore space, reversible intercalation and deintercalation would be impossible, as the particle would expand dramatically, breaking electrical contact with its surroundings.

We have synthesized silicon-carbon composites by low-pressure silicon and carbon deposition on porous ceramic templates with varying size, surface area, geometry and microstructure, as well as commercial carbon materials. The produced nanocomposite samples can be further coated by carbon to improve the quality of the SEI layer and the overall electrode conductivity.

We have systematically investigated the effects of modifying various parameters of these porous Si-C nanocomposites, which will allow us to predict their stability and performance when used as high capacity composite particles. These parameters include the Si and C microstructure, the particle size and shape, and its physical and mechanical properties. We have also experimented with the Li insertion/extraction rate. The final goal of the project is to identify conditions that will allow for complete intercalation and deintercalation of Li without causing particle failure or cracking.

The detailed list of objectives is given below:

Objective 1:

1. Analyze the influence of the thickness of the Si layer and of the internal pore curvature on the stresses generated during lithium insertion and extraction and the electrochemical stability and intercalation capacity of the Si-C composite anodes at different charge-discharge rates.
2. Analyze the impact of C coating thickness on the stresses generated during lithium insertion and extraction and on the electrochemical stability and performance of C-coated nano-Si particles at different charge-discharge rates.
3. Develop an accurate estimate of the mechanical properties of silicon thin films and nanoparticles during various stages of lithiation.
4. Develop a computer model based on FEM (finite elements modeling) which will accurately predict the stresses produced during lithiation of Si thin film- and Si nanoparticle-based nanocomposites.

Objective 2:

1. Analyze the influence of the microstructure and crystallinity of the deposited Si on the stability of the composite particle during cycling and, as a result, the performance and stability of the anode.
2. Analyze the influence of the microstructure and crystallinity of the deposited external C layer on the stability of the composite particle during cycling and, as a result, the performance and stability of the anode.

Objective 3:

1. Analyze the influence of the binder on the surface chemistry of nanocomposite particles, and ergo on the quality and stability of the solid-electrolyte interface (SEI) layer formed on the surface of Si-C composite particles and on the reversible and irreversible capacity and cycle lifetime of the anode.
2. Analyze the influence of the surface stresses in Si-C composite particles on the surface chemistry of the SEI, and therefore on the reversible and irreversible capacity and cycle lifetime of the anode.

In order to meet the described objectives, we need a method of producing Si-C composite materials with different degrees of internal porosity, pore shape & size, and microstructure. We further need to be able to characterize the material synthesized and anodes produced. These synthesis and characterization methods are described in the sections below.

4. Nanocomposite Anode Materials

4.1 Overview

In order to develop a theoretical understanding of the intricacies of advanced anode materials, we must first synthesize such materials to experiment upon. We have developed these materials as a first step towards the rational design of tailored nanocomposite materials, optimized for the best possible performance. The materials being used as a target of research must be examples of cutting-edge nanocomposites, representing a range of different possible configurations. These materials must feature both an external carbon coating and internal void space, both features which dramatically improve the performance of Si-C nanocomposites. The material must have pores of the desired shape and size, on which carbon and silicon layers or particles of uniform size and controllable microstructure can be deposited, using chemical vapor deposition. One possibility is to use a sacrificial ceramic template, such as porous alumina, on which Si and C thin films can be deposited. This template material can then be removed without destroying the deposited laminate material. Figure 4.1 provides the schematic process flow for the synthesis of composite particles with cylindrical pores.

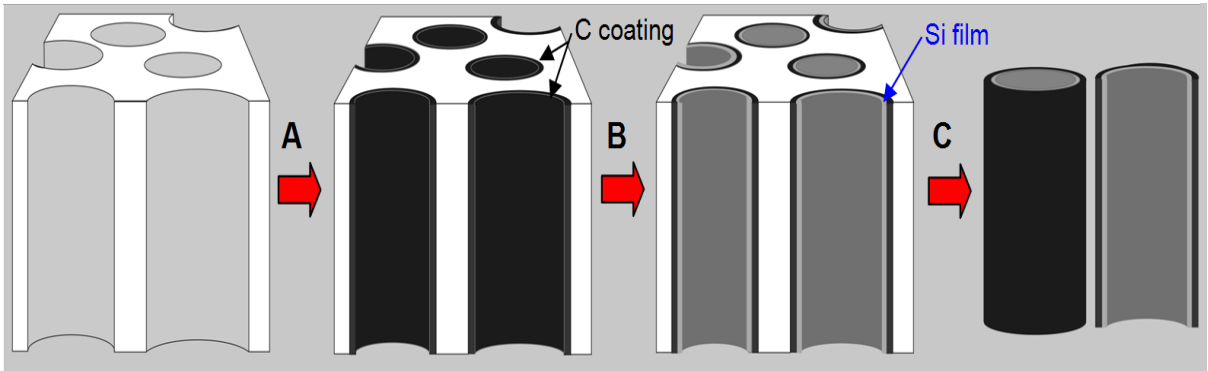

Figure 4.1: Process flow for the synthesis of tubular carbon particles with Si coating the internal pore wall: (A) alumina template is coated with CVD carbon, (B) Si is CVD deposited on the oxidized C surface, and (C) template is removed/etched. The resulting particles have a hard carbon shell and thin amorphous Si inner walls

Alternatively, the nanocomposite material could be produced via self-assembly, rather than templating. We have found that nanocomposites based on Si nanoparticles are particularly appropriate for this approach. Large-scale porous Si-C composite can be formed when coating PureBlack® carbon nanoparticles with Si and C. Examining the produced Si-C nanocomposite samples under SEM, We have found that the coating process caused the carbon nanoparticles to agglomerate into large and mechanically stable spherical porous particles several microns across (Figure 4.2). The mechanism behind the self-assembly of these nanoparticles (Figure 4.2A-B) into nanocomposite porous spheres (Figure 4.2C) is not yet clear, but it could be related to surface energy minimization. These nanocomposites can then be mixed with a binder material, as conventional active nanoparticles might be, and cast onto copper foil as a slurry to produce an electrode. These materials have the advantage of being potentially commercially viable, due to the reduced cost of self-assembly as a production method compared to templating from sacrificial carbons.

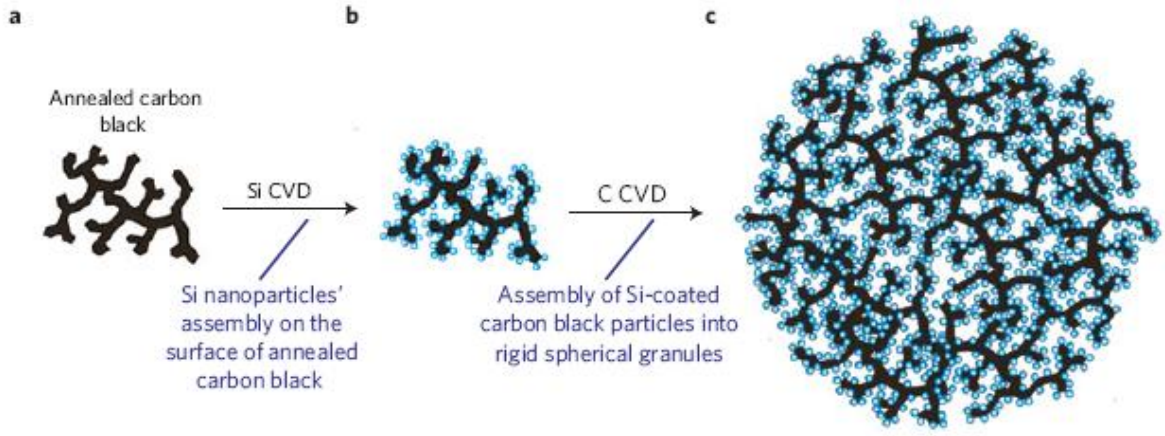

Figure 4.2 (A) Annealed carbon black particles, which are then (B) coated with silicon nanoparticles and subsequently (C) are coated with a carbon thin film and self-assemble into rigid spheres with open interconnected pore spaces

The results of my study of these two types of nanocomposites can be related to a wide range of alternative materials. Precise control over pore size and film thickness in the ceramic template-based nanocomposites lets me easily analyze these properties, and the thin film nature of the active material lets me more easily analyze its microstructure and crystallinity and identify the impact of these factors on anode performance. The self-assembled particles let me more easily analyze the impact of SEI on anode performance - surface analysis of the ceramic template-based nanocomposites will reveal little of the surface properties of the internal surface of the pore, due to the limited depth of most surface analysis techniques. They can also potentially prove useful for analyzing the impact of binders on anode performance, since the template-derived composites may require relatively little binder.

4.2: Porous Alumina Template Nanocomposites

Approach

Silicon-carbon composites have been synthesized by low-pressure silicon deposition on porous ceramic templates with varying size, surface area, geometry and microstructure. The produced nanocomposite samples can be further coated by carbon to improve the quality of the SEI layer and the overall electrode conductivity. We have studied the stability of the produced electrodes depending on the silicon (and carbon) coating thickness, curvature, interface properties and the microstructure of the silicon and carbon components.

The porous ceramic material we have used as a sacrificial template is porous alumina. This template is etched away after the deposition process is complete, producing a porous carbon particle with a Si-coated internal surface, which can serve as a high capacity anode material. During the anode lithiation process, the Li ions intercalate with the C and alloy with the

amorphous Si, ultimately forming $Li_{22}Si_5$. The alloying process is accompanied by the expansion of the alloy material within the pore. The particles will be designed such that the overall diameter of the particle remains virtually constant during this process, as the Si expansion is accommodated by the pore space. These in-house synthesized carbon materials will allow us to finely tune the substrate parameters for systematic and fundamental studies, as well as optimization of the performance of the materials. The knowledge gained in the course of these studies will further the development of advanced battery anodes, producing vital knowledge for the development of new materials based on this technology.

Experimental Methods

The primary sacrificial ceramic template material used in my experiments for the in-house formation of porous carbon-silicon nanocomposites is porous alumina membrane filters (Anopore ®). These filters have a 200 nm diameter pore size, with a uniform, capillary pore structure, and a 60 micron thickness. The pore density is 10^9 pores/cm^2. The crystal structure of the alumina oxide is initially gamma-phase, though it transforms to alpha-phase after being heated above 400 C. The heating was found not to significantly affect the membrane morphology and pore size.

Carbon deposition was done at 700 C using atmospheric pressure chemical vapor deposition, using propylene as a precursor. Silicon deposition was achieved through low pressure chemical vapor deposition (~1 Torr), using 5 % silane and 95% helium as a precursor. The deposition was performed at a temperature of 500 C in order to produce a uniform nanostructured coating, as determined using scanning electron microscopy (SEM). Carbon was initially deposited to produce a conductive, mechanically stable support structure, followed by

the deposition of silicon. A third, thinner layer of silicon was deposited to further improve conductivity and the formation of the SEI layer. The rate of deposition of C and Si under the described conditions has been calculated at approximately 1 nm/min. After coating by carbon and silicon, the alumina templates were etched in a 10% solution of hydrofluoric acid for 1 week, to produce tubular silicon-carbon nanocomposites.

These nanocomposite membranes were attached to copper foil by embedding under pressure into a thin layer of PVDF dissolved in NMP. Prior to being assembled into 2016 lithium-ion coin cell batteries, the electrodes were dried in air at 80 C and in vacuum at 100 C for 24 hours, using a vacuum chamber attached to the glovebox. 1.5 mm thick lithium foil was used as a counter electrode. A Celgard 2325 membrane was used as a separator, and a standard Li-ion battery electrolyte was used (lithium hexafluorophosphate salts, dissolved in ethylene, dimethyl, and diethyl carbonate (1 M in 1:1:1 solution). Pouch cells were also constructed, using an additional lithium counter electrode.

The assembled cells were tested using Arbin and Solartron potentiostats. The standard battery test protocol included constant current and constant potential segments. In the constant voltage part of the test the potential of either 0.1 V (charge) or 1.99 V (discharge) was applied to the cell until the current dropped to 5% of the constant current rate. The first cycles were performed with a constant current regime calculated to charge and discharge the battery within 20 hours (C/20) in order to form a good quality SEI. Rapid charge/discharge (C/1) and electrochemical impedance spectroscopy (frequencies between 100 kHz and .01 Hz, 10 mV amplitude) were also used to further characterize the performance of the anode material. After cycling, the samples were disassembled and examined using both SEM and transmission electron microscopy (TEM).

Results

We have successfully produced tubular silicon-carbon nanocomposite particles and converted them into Li-ion battery anodes in both coin cells and pouch cells. The samples have an outer C layer approximately 60 nm thick, a Si layer ranging between 0 and 40 nm thick, and an inner C layer approximately 10 nm thick. Horizontal and vertical cross-section images of one of the produced samples can be seen in Figure 4.3a-b.

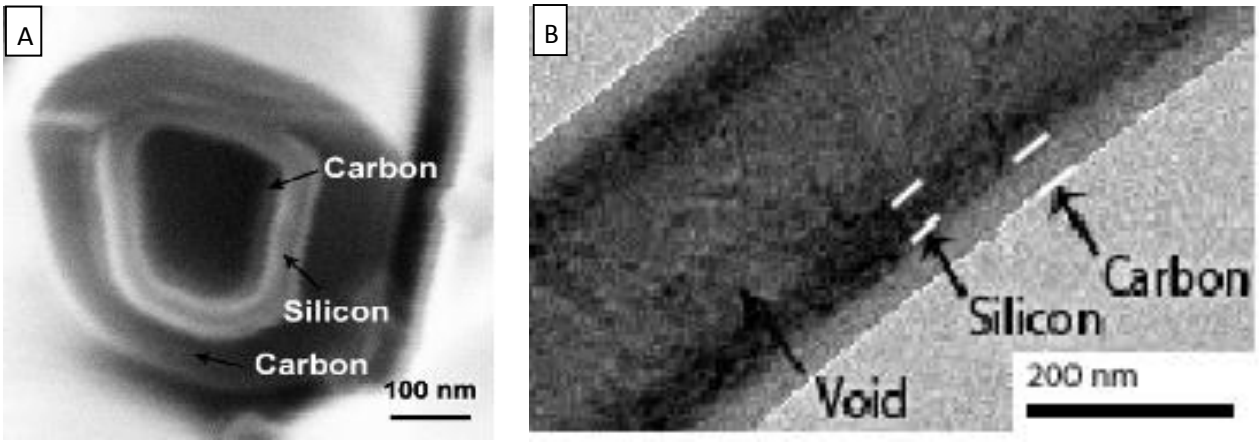

Figure 4.3*:* a) Scanning electron micrograph horizontal cross-section image of sample; b) Transmission electron micrograph vertical cross-section image of sample

TEM and SEM studies have demonstrated the deposited layers of Si and C to be uniform in thickness and composition. After the deposition of the initial Si and C layers, a thin (~10 nm) layer of C is deposited, in order to improve solid-electrolyte interface (SEI) formation, and the ceramic template is then removed via etching in hydrofluoric acid (HF), resulting in a vertically aligned array of carbon/silicon nanocomposite particles with a predefined pore shape and size. Using this method, we have produced aligned nanocomposite particle electrodes with specific Si

content ranging from 51% to 35%, 33%, 27%, 23%, 16%, 9%, and 0%, with correspondingly changing void space volumes.

Tested at C/20, we find that irreversible capacity losses after the first cycle are low, and tend to decrease with increasing silicon content. Similarly, Coulombic efficiency tends to increase with increasing silicon content. In some samples, the fading rate drops as low as .1% per cycle. This data is shown in Figure 4.4a-c. Since I was primarily interested in revealing the microstructural changes in the composites and not in the cycle-life, I typically performed no more than 10 to 20 cycles for each test. The relationship between the theoretical specific capacity and the experimentally determined specific capacity is shown in Figure 4.4d. As we increase the Si content of the anode, the cell tends to exhibit improved Coulombic efficiency after the first two cycles due to the higher Si capacity and accordingly smaller contribution of the losses at the particles' surface. As expected, increased Si content produces an increase in Li intercalation/deintercalation capacity. The increase in capacity with % Si tends to be linear with increasing Si content. Most of the samples were tested in 2 or 3 separate cells, and exhibited similar performance trends.

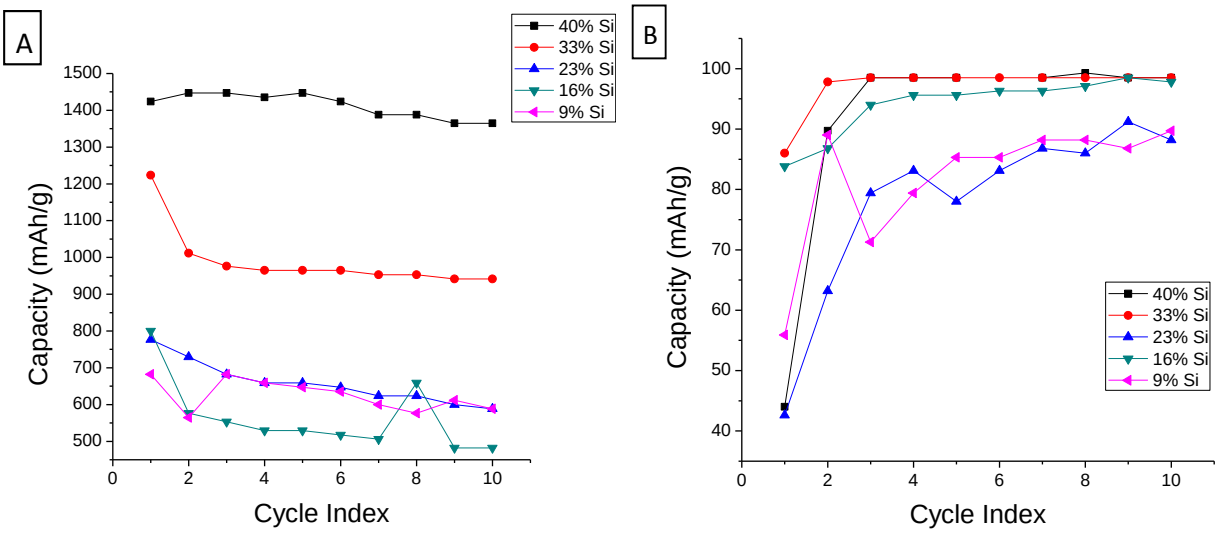

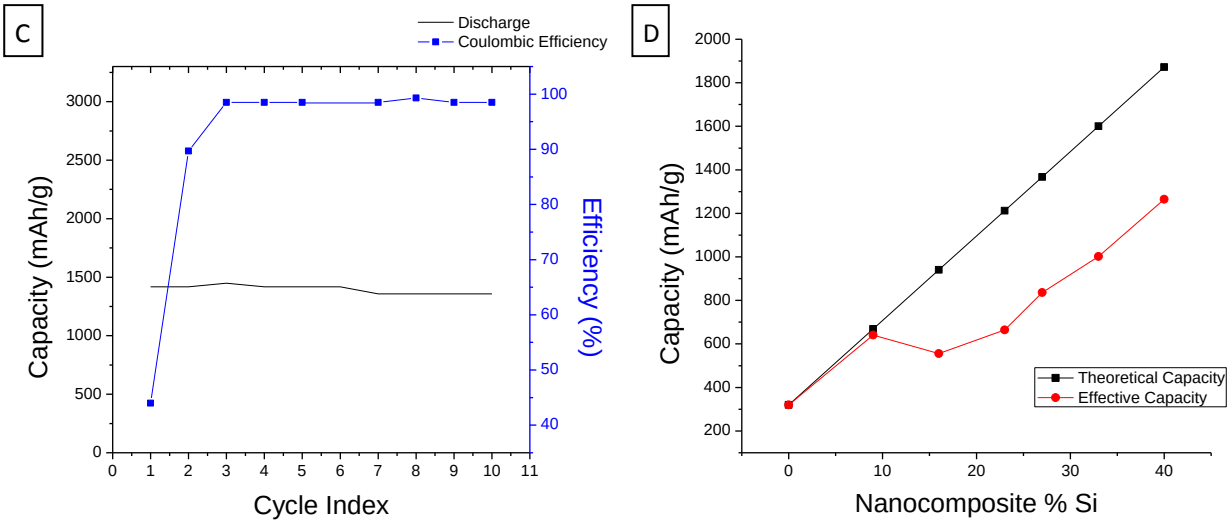

Figure 4.4: a) Reversible discharge capacity over 10 cycles under a C/20 discharging rate for select samples. b) Coulombic efficiency of all samples shown in (a). c) Discharge capacity and Coulombic efficiency data for 40% Si sample shown in (a). d) Comparison of theoretical capacity of samples to experimentally derived capacity (averaged between cycles 3 and 5) at C/20.

Interestingly, we see a drop in the intercalation capacity between 9% Si and 16% Si – for a Si layer between 5 and 8 nm thick. For 9% Si samples, the capacity is roughly equivalent to the theoretical capacity; for 16% Si and higher, the capacity is approximately 60% of theoretical. This phenomenon may suggest an abrupt change in the behavior of the material during the first intercalation/deintercalation cycle, when the thickness of the Si layer exceeds 5 nm. Samples with Si content greater than 46% failed rapidly, with their capacity dropping rapidly. We believe this is due to excessive expansion of the lithiated thin film, bursting the pore which normally contains it.

We hypothesized that thin (5 nm) Si films remain in good contact with C surface during the insertion and extraction of Li (Figure 4.5), while thicker (9 nm) Si may experience partial delamination due to stresses at the interface between Si and C. In the idealized case (Figure 4.5), the expansion of the Si during Li insertion is contained within the pore of the nanocomposite

particle, allowing the void space to compensate for the volume change. If the expansion is compensated by the void space, the solid-electrolyte interface remains intact, and the particle's contact with the current collector remains uninterrupted. However, if delamination between the Si and outer C surface takes place, part of the inner Si tube may become inactive, lowering the total capacity value. In addition, this delamination is expected to create a new interface between the electrolyte and the Si, which may lower the Coulombic efficiency.

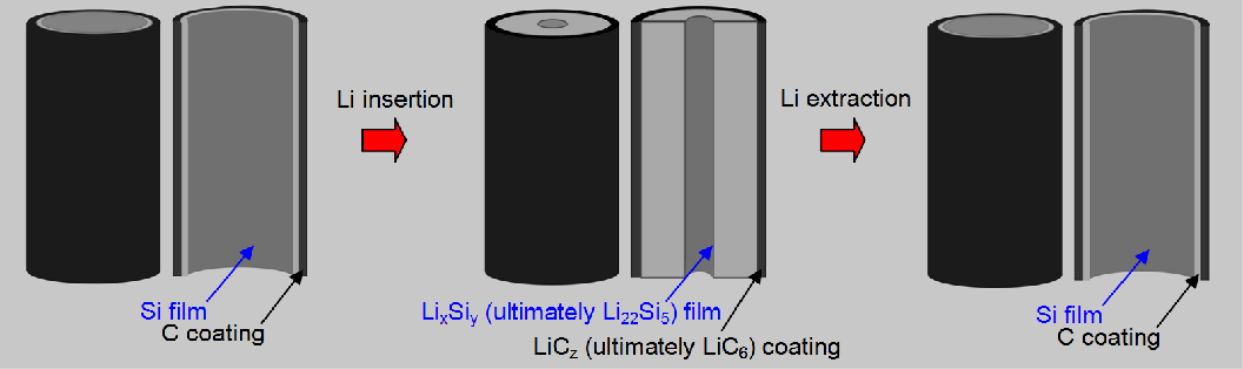

Figure 4.5. Schematic of idealized nanocomposite particle lithiation and delithiation process, showing return of particle to its original configuration.

TEM microscopy of the lithiated samples (Li inserted into Si) revealed that, independent of the Si thickness, Li insertion transforms the nanocrystalline Si into an amorphous Li_xSi phase (Figure 4.6a), but remains constrained by the carbon outer structure, as predicted (Figure 3). However, when Si thickness exceeds 9 nm the film delaminates upon Li extraction. This process is most clearly seen for thicker films (Si wt. % 33 and above, Figure 4.6b)

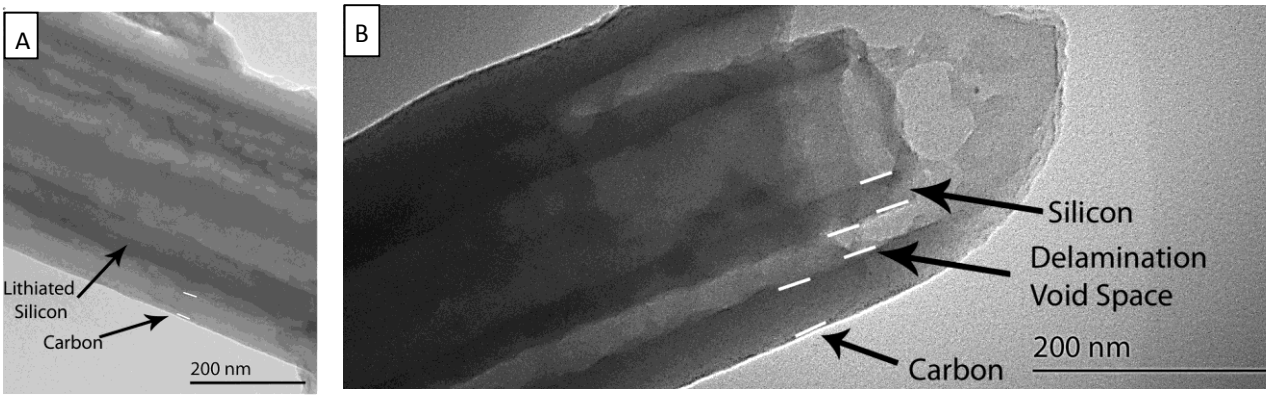

Figure 4.6. Transmission electron micrographs of a) lithiated and b) delithiated 33% Si porous alumina template nanocomposite particles. These samples have been cleaned of most of the solid electrolyte interface to assist in clear imaging.

This observed delamination effect accounts for the drop in capacity of samples with Si films thicker than 5 nm. TEM images also confirm that 5 nm Si samples do not undergo delamination after repeated cycling (shown in Figure 4.7 below). We have concluded that the stress produced by the alloying and expansion process induces this delamination, and that this stress is influenced both by the thickness of the silicon layer and by the presence of defects in the silicon.

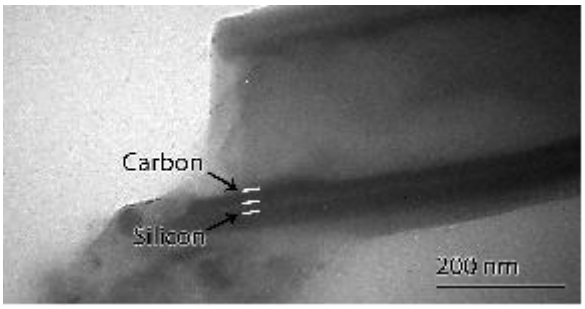

Figure 4.7: TEM micrograph of 9 wt% Si nanocomposite sample (5 nm Si film) after cycling, showing absence of delamination

Annealing our 33 wt% Si samples at 850 C for 2 hours results in the strengthening of the C and Si, due to the healing of defects such as dislocations and vacancies. After annealing, we found the capacity of the samples improved (Figure 4.8a). Interestingly, TEM images showed a

reduced void space between the outer C and inner Si cylinders after cycling. These results are shown in Figure 4.8b, below.

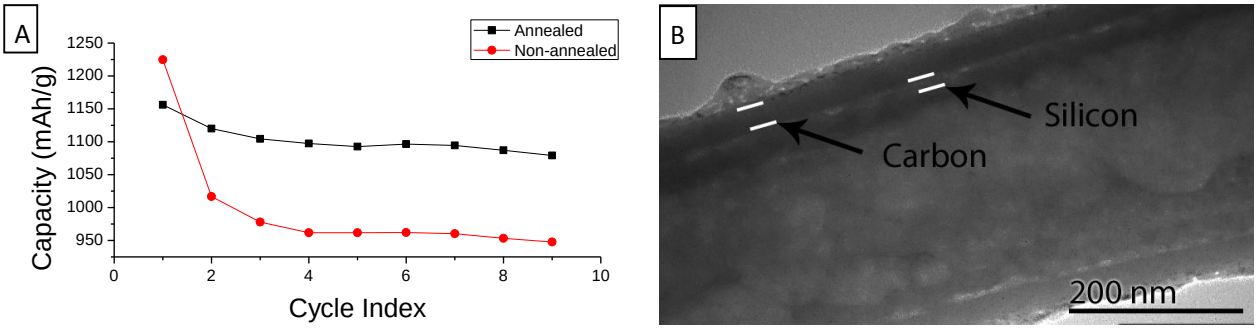

Figure 4.8**:** a) Capacity of annealed and un-annealed 33% Si nanocomposite samples; b) TEM micrograph of annealed 33% Si sample after cycling

Our observations suggest that annealing improves the mechanical and electrical properties of the Si-C composite, and that there may be a correlation between defect population and delamination, allowing us to more easily model the sample and understand changes in its structure.

In order to better understand this effect, we have examined the impact of the microstructure of C and Si on the performance of our materials. We examined the impact of the crystallinity of the Si thin film (the active material) independent of thickness using X-ray diffraction. We also used Raman spectroscopy to analyze the microstructure of the C outer film.

We compared the crystallite sizes of the Si thin film before and after annealing, as determined via XRD. The X-ray diffraction patterns are shown at right, in Figure 4.9. The Si <111> peak showed significantly smaller width after annealing; the crystallite size increased from 14 nm to 40 nm. An increase in crystallite size such as this can be a product of a substantial reduction in internal stresses within the Si thin film. This reduction in internal stresses could be a factor in the improved capacity of the annealed samples - as our previous XRD data indicated,

samples with higher crystallite size tend to be less susceptible to delamination, and our TEM imagery indicates that the annealed samples undergo less delamination during cycling than the less-annealed nanocomposites.

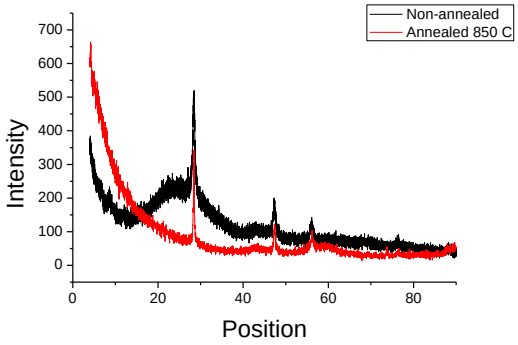

Figure 4.9: XRD patterns of annealed and unannealed Si nanocomposites

Raman spectroscopy is a spectroscopic technique that uses lasers to detect vibrational and rotational modes within a sample, and which serves as a valuable method of surface analysis. It functions by focusing a laser in or near the visible range onto a surface, the energy of which is then altered by inelastic scattering. Molecular vibrations alter the energy of the laser photons, and the resulting beam, no longer monochromatic, can be analyzed to find the various vibratory modes within the system. This provides valuable information on chemical composition and bond states within the sample, as well as microstructure. In particular, the microstructure of carbon can be interpreted via Raman spectroscopy; this technique functions by examining the relative intensities of the G (graphitic) and D (disordered) bands, occurring at 1350 and 1600 cm^{-1} respectively. The lower the ratio of the integrated intensities of I_D to I_G, the more ordered (graphitic) the microstructure of the carbon is. The data gathered via Raman spectroscopy and the relative intensities of the D and G bands are shown below, in Figure 4.10.

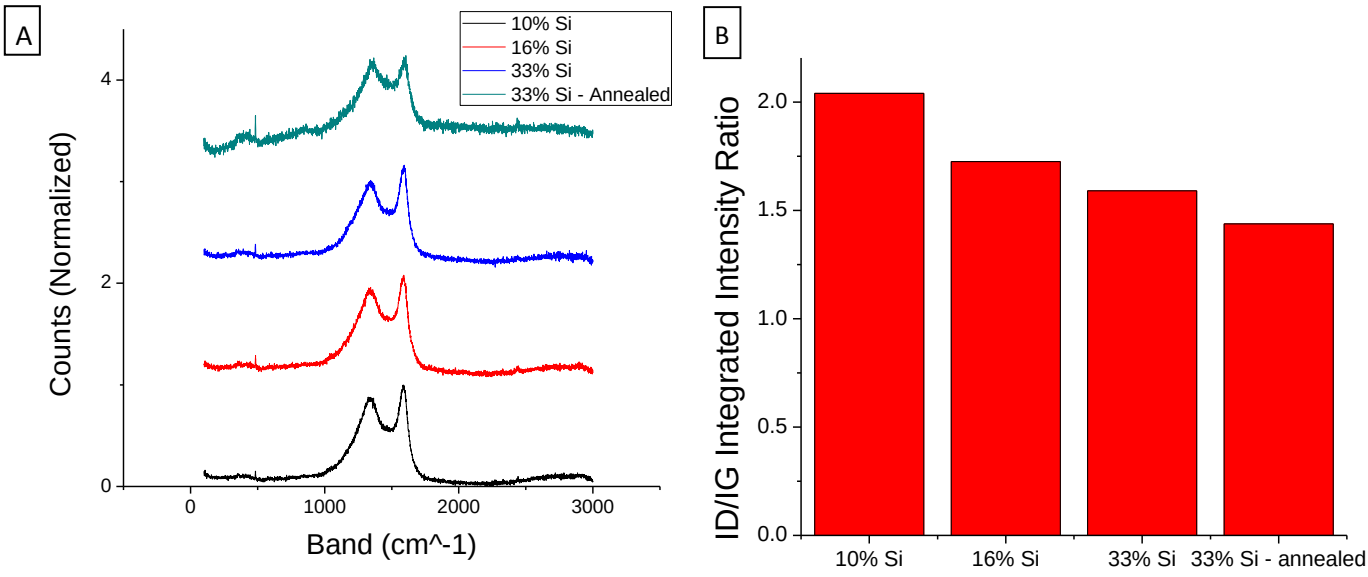

Figure 4.10. a) Raman spectroscopy patterns from nanocomposite samples; b) Ratio of integrated intensities of D and G bands from spectroscopy patterns of nanocomposites

These Raman spectra support the idea that the outer C layer becomes increasingly graphitized as the thickness of the Si thin film increases. One possible explanation for this effect is that thin films of Si may, upon cooling after deposition, produce internal stresses and defects in the C outer shell. Thicker films will produce lower stresses in the shell, since the stresses of cooling are compensated by the development of defects within the film itself. Similarly, we can see that annealing increases the degree of graphitization of the outer C layer. Increased graphitization typically corresponds with a higher diffusion coefficient, and therefore reduced impedance. It may also improve the quality of the interface between Si and the outer C coating.

I have also analyzed these samples at high rate cycling conditions – using C/1 charge and discharge rates instead of C/20. Under these conditions, and using an electrolyte with 5 wt% vinylene carbonate to improve the formation of the SEI, I have found that the capacity is reduced to approximately 80% of the C/20 capacity, roughly 750 mAh/g, but the fading rate remains low. More importantly, the Coulombic efficiency exceeds 99%. Even efficiency as high as 99% will

dramatically impair the functionality of a balanced full cell within less than 100 cycles due to the irreversible loss of lithium. However, these cells show a Coulombic efficiency of 99.6% for the first 50 C/1 cycles, and in excess of 99.9% for cycles 50-800. This high efficiency may be a product of the excellent mechanical stability of the composite particle, produced by the rigid carbon outer shell. The particle's high stability can prevent degradation of the SEI from rapid volume changes. These results are presented at right, in Figure 4.11. Using high charge and discharge rates appears to have minimal effects on the performance of these batteries – even under extreme conditions, they retain excellent performance.

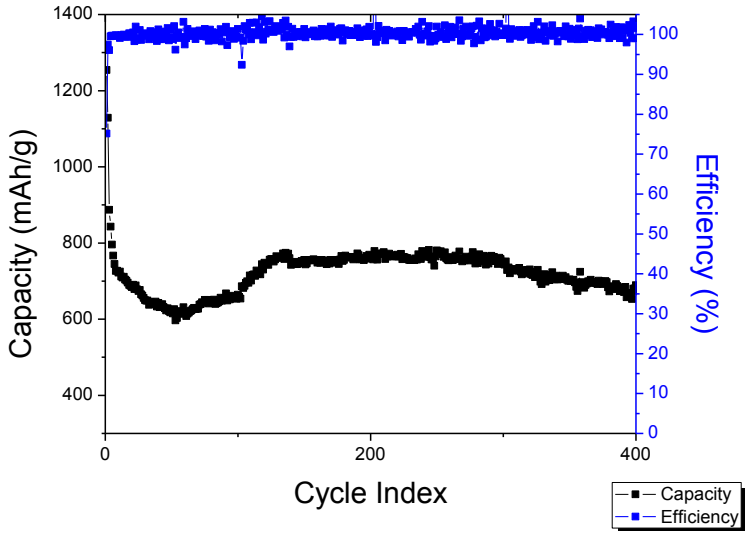

Figure 4.11. Capacity & Coloumbic efficiency of 33 wt% Si nanocomposite particles cycled at C/1

These samples have been tested using EIS (electrochemical impedance spectroscopy). This tool measures the dielectric and electrochemical properties of a cell by applying an alternating current at a varying frequency to it. As the frequency changes, the impedance - the the cell's resistance to the AC - changes as well. The response of the impedance to changing frequency can be characterized as a complex function, with both imaginary and real impedance

components; it can be effectively described graphically as a Nyquist plot, which compares imaginary impedance (often produced by capacitance) on the y-axis and real impedance

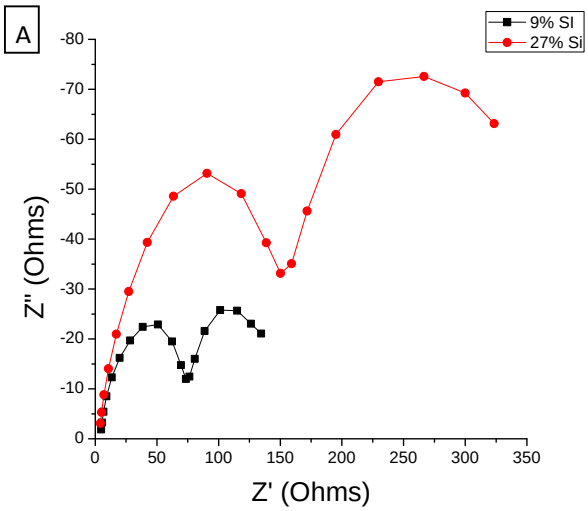

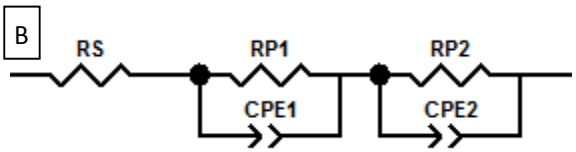

C

% Si	Rs (Ω/g)	CPE-T (F/g)	CPE-P	Rp (Ω/g)
27	3283	4.81E-002	0.696	2.56E+005
9	4487	7.54E-002	0.682	9.96E+004

***Figure 4.12*:** a) Nyquist plot of impedance of nanocomposites; b) Equivalent circuit model of nanocomposite; c) Impedance circuit element values of nanocomposite samples

(effectively the DC resistance of the system) on the x-axis. One example of one of these plots is shown in Figure 4.12a. In order to model the different components of impedance in this system, we created an equivalent circuit model, shown in Figure 4.12b.

Each of the parallel elements of the model shown in Figure 4.12b represents one of the electrodes of the cell. In this model, R_S is the cell resistance, representing the intrinsic resistance of the electrolyte and current collector, R_P is the polarization resistance (sometimes called the charge-transfer resistance), representing the resistance to the intercalation, plating or alloying of lithium ions with the electrode, and CPE is a constant phase element, representing the capacitance of an electrical double layer - the layer of charged particles present at the surface of the electrode. The CPE's electrochemical properties can be characterized as two separate components: CPE-T, representing the capacitance of the system in farads - heavily dependent on

the surface area of the samples - CPE-P, a power factor representing the deviation of the system from the ideal behavior of a capacitor. CPE-P is 1 in a true capacitor; lower values indicate a less homogeneous system. We tested two different nanocomposite samples using this methodology, testing them after 1 C/20 cycle (to ensure the proper development of the SEI. Examining the behavior of the nanocomposite electrode using this model, we find several difference between the two samples. First, we find that the cell resistance increases with increasing %Si, presumably due to the higher natural resistivity of Si compared to C. The double-layer properties of the sample do not change significantly with increasing % Si; within the range of structural properties examined in this test, the surface area of the electrodes does not change significantly. The polarization resistance does change significantly - it more than doubles at the increased %Si. This may be due to the delamination effect observed at higher %Si; alternatively, it may be due to a lower diffusivity of lithium within the Si thin film as the crystallite size drops.

We have also tested the impedance properties of the system at C/1 charge and discharge rates, as a function of the number of cycles. The impedance properties of the system whose electrochemical performance is displayed in Figure 4.11 are given in Figure 4.13, below. Examining the properties of this system, we found that the capacity of the electrode did not change significantly after the first cycle - the structure of the electrode remains roughly stable after initial lithiation and delithiation. The cell and polarization resistance, however, steadily increases with increasing cycle index after the 300th C/1 cycle, when the capacity of the electrode starts dropping. This suggests that the cell is losing capacity due in large part to an increase in the impedance. This increase might be caused by a number of factors, including structural destabilization (possibly related to the delamination effect noted above) or the development of an insulating SEI, preventing efficient Li ion alloying.

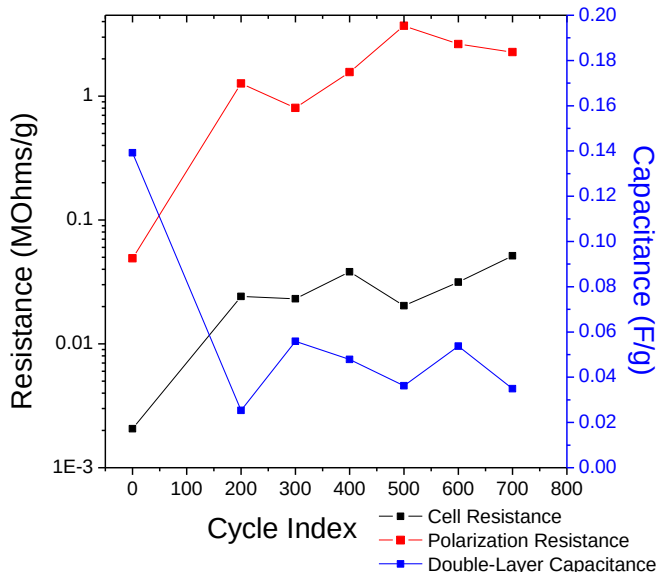

***Figure 4.13*:** Impedance circuit element values of 35% Si nanocomposite sample

We investigated the delamination effect we observed previously and its effect on the electrode performance. When delamination does not occur, these materials are capable of achieving theoretical capacity comparable to theoretical performance; when delamination does occur, performance is limited to 60% of theoretical levels or less. We hypothesized that this loss of performance was a product of the development of a thick, insulating SEI between the carbon and silicon thin films - during delamination, the electrolyte could infiltrate the gap between the Si film and the outer C wall, and then decompose during charge and discharge into a thick insulating layer. This insulating layer would prevent direct electrical contact between the Si film, which provides most of the capacity of the anode, and the conductive C backbone. Due to the semiconducting nature of the Si film, even partial delamination would drastically increase the resistivity of the contact between Si and C and therefore substantially increase the impedance and decrease the capacity of the material. This effect could explain the link between delamination and the drop in capacity already noted.

We initiated a series of experiments in order to test this hypothesis. We tested the impact of delamination and SEI development by sealing the top of the pores of the nanocomposites with a layer of polymer or amorphous carbon. With the top of the pore sealed, lithium ions would only be able to alloy with the Si film by diffusing through the C side-wall or through the top covering. The electrolyte would not be able to enter the pore, preventing the development of SEI inside of it. This would improve electrical contact between the Si film and the outer wall. An example is shown in Figure 4.14, below.

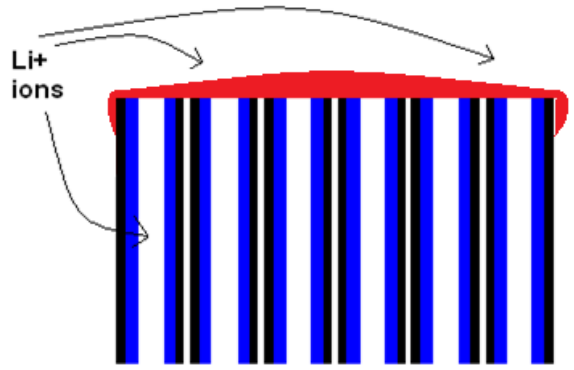

***Figure 4.14*:** Structure of coated nanocomposite particles

We subsequently tested this hypothesis by casting a thin layer of PVDF over our samples before testing them. We found a significant improvement in performance at slow charge/discharge rates, shown below in Figure 4.15a. The PVDF-coated samples exhibited dramatically improved lithium capacity, compared to the 960 mAh/g performance of the uncoated samples (60% of theoretical capacity). The PVDF-coated samples exhibited the best performance, with a capacity of ~1600 mAh/g – roughly equal to the theoretical capacity. The Coulombic efficiency of the coated samples, shown in Figure 4.15b, does not exhibit an improvement over the performance of the uncoated samples, which possess 99% efficiency. The PVDF-coated sample in fact exhibits poorer CE, with a value of 98%.

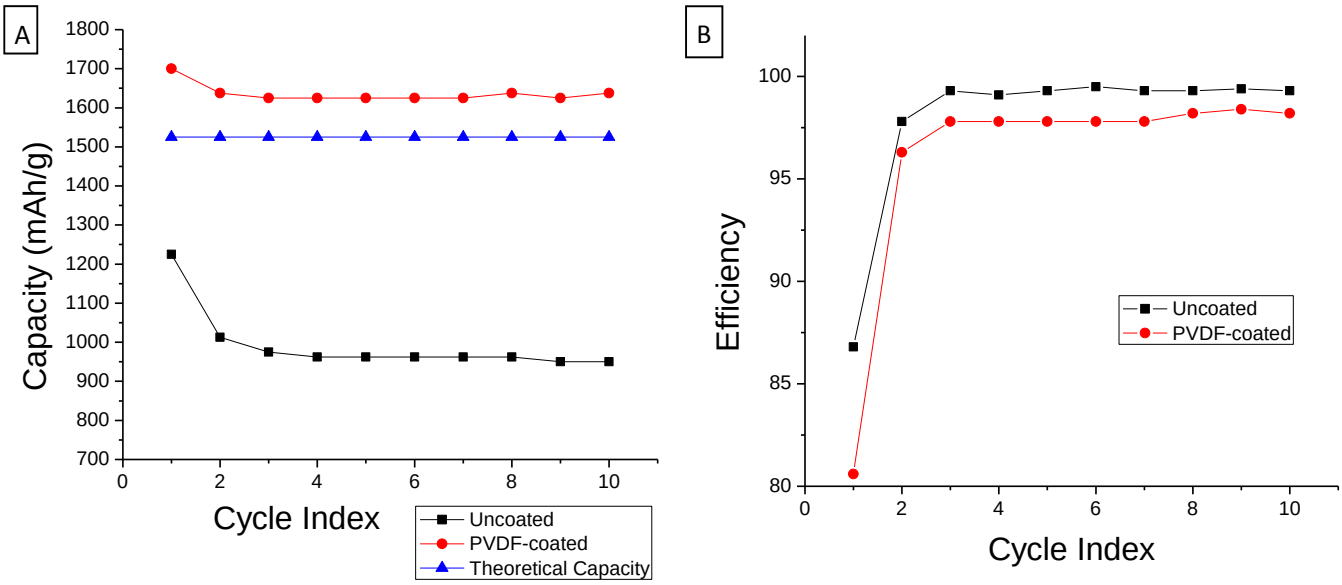

Figure 4.15: a) Capacity of 33% Si nanocomposite samples cycled at C/20 with various forms of surface modification; b) Coulombic efficiency of same

We have also tested these samples at higher charge-discharge rates - using C/1 instead of C/20. These results are shown below, in Figure 4.16. At these rates, the samples exhibit performance inverse of that exhibited at slower charge/discharge rates - the capacity of the surface-treated samples drops, while their efficiency increases compared to the uncoated samples. The uncoated samples exhibit a capacity of ~750 mAh/g, compared to ~150 mAh/g for the PVDF coated samples. The efficiency of the surface-treated samples, however, increases compared to the uncoated samples. This effect might be explained if we assume that delamination still occurs, even in a sealed pore - at slow charge-discharge rates, the lithium can still access the silicon by diffusion through the outer C wall, even with the Si film partially detached. Diffusion through solid C is slower than diffusion through the liquid electrolyte, however, and at faster rates, the bulk of the silicon remains inaccessible and inactive due to the increased impedance to lithium ion conduction. This behavior lends credence to our hypothesis.

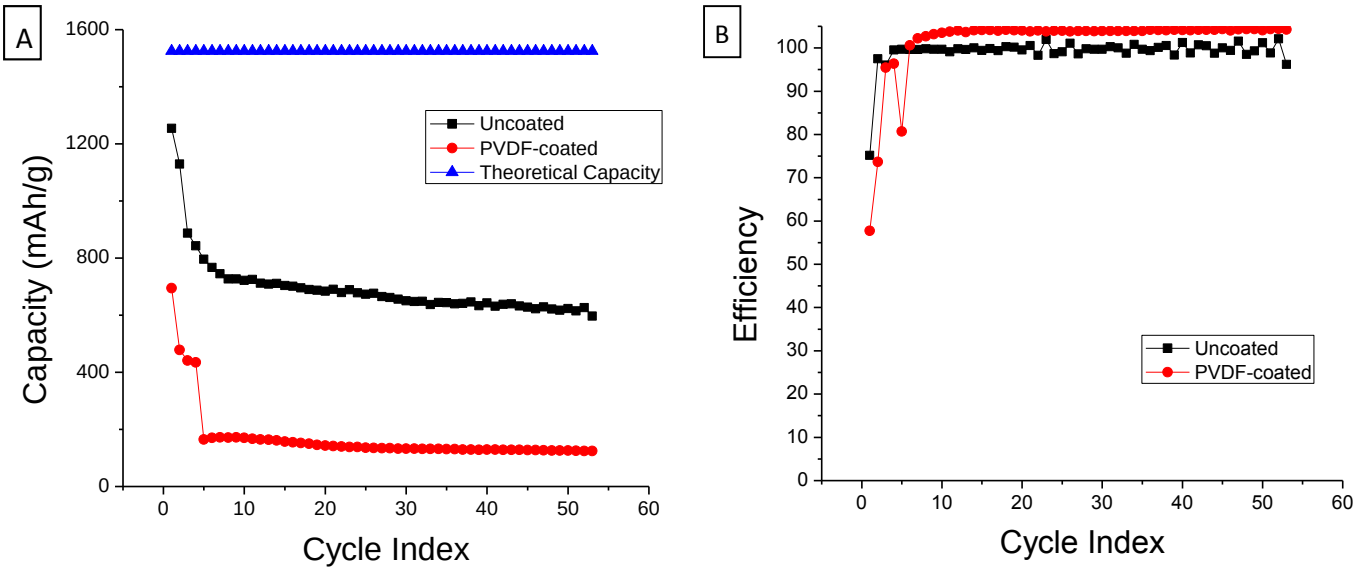

Figure 4.16: a) Capacity of 33% Si nanocomposite samples cycled at C/1 with various forms of surface modification; b) Coulombic efficiency of same

We have tested the impedance properties of several of these surface-treated samples using EIS at C/20 rate, as described previously. We tested samples at C/20, after 10 cycles. The spectrographs derived from these tests are shown in Figure 4.17a; the impedance measurements derived from them are shown in Figure 4.17b of these tests.

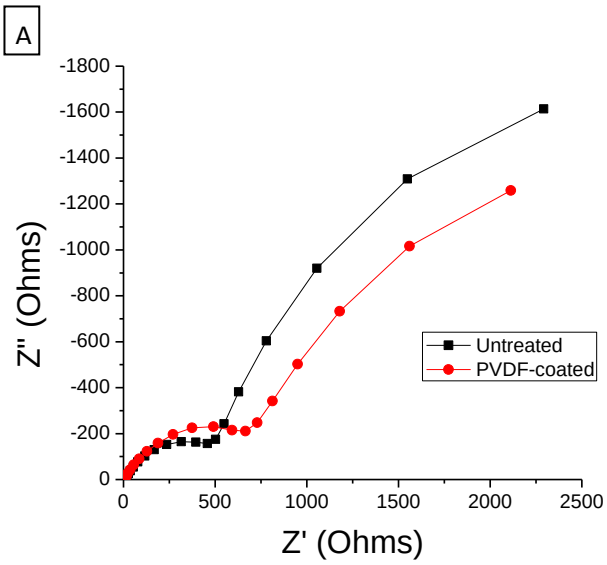

B

Sample ID	Rs (Ω/g)	CPE-T (F/g)	CPE-P	Rp (MΩ/g)
Untreated C/20	41798	.369	0.59	5.73
PVDF-coated C/20	42600	.223	0.62	6.50

***Figure 4.17*:** a) Capacity of 33% Si nanocomposite samples cycled at C/1 with various forms of surface modification; b) Coulombic efficiency of same

The cell and polarization resistance of the samples do not decrease significantly after being coated, compared to the untreated sample. The specific capacitance, however, does decrease, consistent with a decrease in specific surface area. Capacitance being heavily dependent on surface area exposed, the decrease in area caused by the pores being sealed would certainly produce a drop in capacitance. The biggest difference in the impedance properties of the new material is a substantial increase in the impedance of the second half of the Nyquist plot. This kind of behavior is often associated with an increase in impedance to ion diffusion. When the diffusion coefficient of a system increases, precipitous increases in impedance become more common at lower frequencies. This effect may be a product of the closure of the pore as well - without an open pore, Li ions must diffuse directly through the carbon sidewall, which reduces their rate of diffusion - diffusion through a solid material is generally slower than diffusion through a liquid electrolyte.

We have also examined our surface-treated samples post-lithiation via TEM, in order to directly examine the delamination process. A micrograph of the fully cycled PVDF-coated tube cross-section is shown in Figure 4.18, below. We can see from this micrograph that delamination certainly still occurs - as in previous samples, the Si thin film delaminates from one side of the C outer wall and shrinks in diameter. Despite this delamination, the C/20 capacity remains high. This suggests that our hypothesis is correct - it is not the delamination that causes a loss of capacity at slower charge/discharge rates, but the SEI that develops between the two thin films. The decomposing electrolyte prevents electrical contact within the delaminated area, deactivating part of the Si thin film. However, at faster charge-discharge rates, the process of

delamination can contribute directly to a loss of capacity - diffusion through solid C is too slow a process at these high rates, and as a result, the delaminated areas of the Si thin film remain inactive at these high rates. An open and fully accessible pore would appear to be necessary at these higher rates, unless the Si thin film is thin enough and crystalline enough to avoid delamination - in this case, an open pore might be unnecessary, although we have not had an opportunity to test this concept.

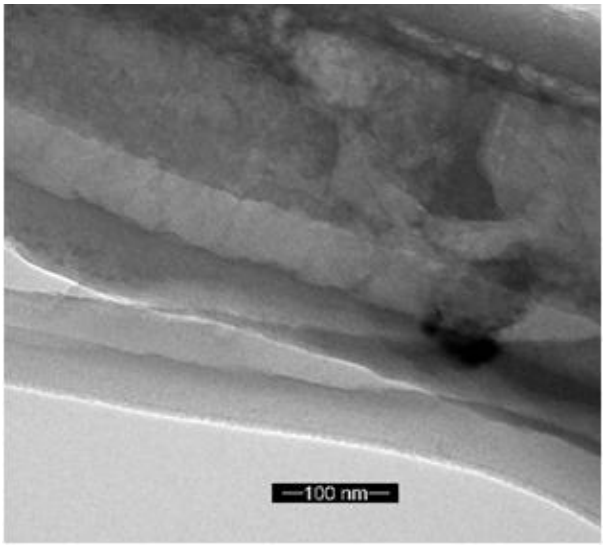

***Figure 4.18*:** TEM micrograph of PVDF-coated nanocomposite tube, after charge/discharge

4.3 Granular Nanocomposites

Approach

In our review of the literature, we concluded that the ideal nanocomposite would require must possess pores which can provide the volume needed for Si expansion, compensating for the stresses produced during expansion, and allowing for the fast transport of Li ions. An outer layer of C may improve the quality of the solid-electrolyte interface (enhancing the Coulombic efficiency) and improve the overall structural integrity and electrical conductivity of the composite. The composite particles must retain their original size and shape during cycling, in

order to minimize damage to the binder and the electrode, as well as conserve space within the cell. Nanocomposites produced by pyrolysis, mechanical milling and mixing, or combinations of these methods produce dense active materials without the ability to absorb the strains produced during charge and discharge. A chemical vapor deposition method may therefore be better suited to produce nanocomposites with the desired microstructure.

Unfortunately, template-based processes such as those discussed previously are prohibitively expensive for commercial applications. An alternative method must therefore be found for producing nanocomposites with tailored structural and microstructural properties which can be manufactured inexpensively. While chemical vapor deposition is the ideal method for producing this type of material, the uniform deposition of Si nanoparticles or thin films within C structures less regular than those produced via templating is difficult, due to the comparatively tortuous diffusion pathways within such maerials. The small scale of the films or particles being deposited makes development of optimized composite particles even more difficult – as established previously, the films or particles deposited must have extremely small dimensions for optimal stability, ~5 nm for a film (given a ~ 200 nm diameter pore) or 10-30 nm for a nanoparticle. Dimensions greater than these risk delamination at the C/Si interface or particle fracture during charge/discharge. In the case of a nanoparticle sample of these dimensions, the size of the pore should be between 34-102 nm to enable complete compensation of the particle's expansion.

Bottom-up assembly may offer a promising solution for low-cost synthesis of nanocomposite active material than templating. Self-assembly permits the development of sophisticated nanocomposites from basic components, producing materials with new properties.[69] Small nanoparticles are known to produce systems with controllable pore sizes

via self-assembly.[70] These ordered systems can potentially possess the kind of regular pores we need for commercially viable Si-C nanocomposites. This effect is produced by strong interactive forces between these nanoparticles, which produce ordered agglomerates. These agglomerates can potentially be used to produce Si-C nanocomposite active materials for Li-ion batteries via conventional slurry-casting methods.[71] Depositing Si nanoparticles on basic components which then self-assemble into larger, granular particles permits us to ensure even distribution of Si active material throughout the final granular particle. In addition to functioning as an effective high-capacity anode material, these granular agglomerates possess micron-scale dimensions which reduce the cost and complexity of handling and electrode manufacture compared to nanoparticles. Self-assembly processes are therefore a highly attractive alternative to the previously described methods of electrode fabrication.

This process involves chemical vapor deposition of Si, using similar conditions to those employed to produce our template-based nanocomposites. The initial substrate is carbon black nanoparticles, which develop a somewhat dendrite-like structure during high-temperature annealing. (Figure 4.19a) Small Si nanoparticles are deposited onto the carbon black nanoparticles via decomposition of SiH_4 gas at low pressure. Control of the deposition time, temperature and pressure permits us to control the size of the Si nanoparticles deposited.[72] The nanoparticles are deposited onto the branching structures, effectively creating pores for the expansion of the Si nanoparticles. (Figure 4.19b) After Si deposition, a carbon thin film is deposited onto the nanocomposites using the atmospheric-pressure decomposition of propylene. During this second deposition, the nanocomposite particles then self-assemble into large, porous, spherical granules. (Figure 4.19c) The size of the composite granules is determined by the size of the initial carbon black particles and by the parameters of the carbon CVD. This process

allows us to inexpensively produce Si-C nanocomposite particles within the parameters previously described as ideal.

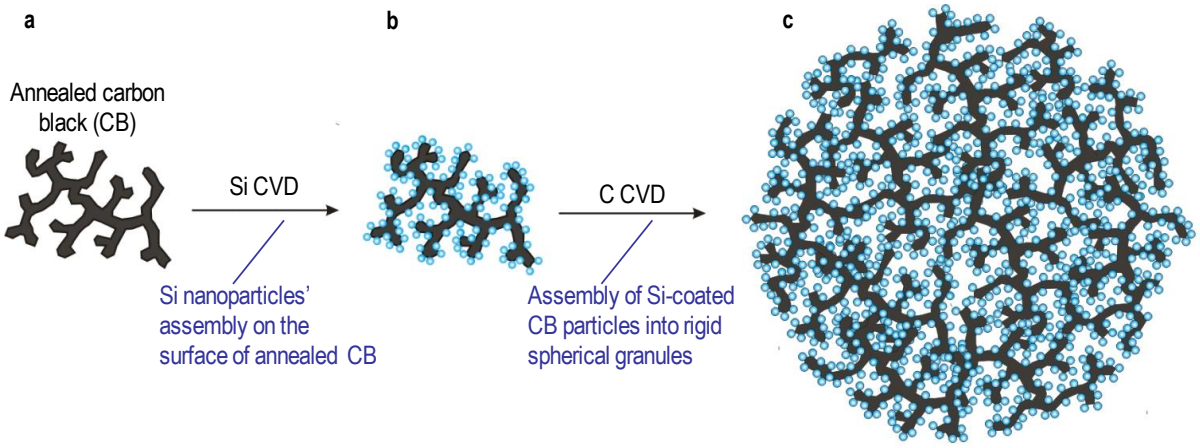

Figure 4.19. Schematic of Si-C nanocomposite granule self assembly. a) PureBlack nanoparticles with dendritic chain structure; b) PureBlack after decoration with Si nanoparticles; c) Nanocomposite particle after self-assembly, forming granule with interconnected pores

Experimental Methods

The dendritic annealed carbon black particles were selected as a substrate for Si nanoparticle deposition due to their open structure, low apparent density and high specific surface area. In the final nanocomposite particle, these factors contribute to the development of semi-regular pores with sufficient void space to buffer the expansion of the Si nanoparticles. Furthermore, these particles are low-cost, partially compensating for the expense of the chemical vapor deposition process. The annealing process (>2000° C) improves the graphitization and purity of the nanoparticles, minimizing side-reactions and increasing their Coulombic efficiency.

Si was deposited onto our annealed carbon black samples at ~1 Torr in a horizontal tube furnace (inner tube diameter ~28 mm) at 500° C. The precursor gas mixture used was 5% SiH_4, 95% Argon (Airgas, USA), using a flow rate of 50 sccm for 1 hour. Carbon deposition was performed at atmospheric pressure in a similar horizontal tube furnace (inner tube diameter ~20

mm) heated to 700° C. Pure propylene (C_3H_6) precursor gas was used, having been introduced at a flow rate of 50 sccm for 30 mins. In order to minimze the backflow of air into the system, a bubbler filled with mineral oil was placed at the exhaust end of the system. Before and after both sets of CVD experiments, the tube furnace was purged with high purity Ar at a flow rate of 50 sccm, thereby avoiding oxidation of the samples if they are exposed to air while at high temperatures. In order to further minimize the risk of oxidation, the samples were taken out of the furnace at temperatures below 50° C.

The samples were characterized via a range of different methods. The wt% of Si and C deposited on the substrate was estimated using a high precision analytical balance (AND GH-120, A&D Company, Japan), as well as by using a thermo-gravimetric analysis system (Q50, TA Instruments, USA), which measures the mass change during C and Si oxidation in air at high temperatures (>600^{O} C). TEM imaging was carried out using a Philips CM200UT microscope (Philips, Netherlands). This device has a 0.18 nm point resolution, operates at 200 kV. Additionally, it is equipped with an EDX detector. Further high resolution TEM observations were carried out using on a Titan S/TEM microscope (FEI, Netherlands), equipped with a SuperTwin objective lens with a Cs of 1.2 mm. In contrast to the previous model, this microscope has a point resolution of 0.245 nm, an information limit of 0.08 nm. It also operates at 200 kV. X-ray diffraction (XRD) spectra were acquired using a Panalytical X'Pert PRO Alpha-1 diffraction system (Pananalytical, Netherlands). This device is equipped with an incident beam monochromator, and uses only Cu Kα1 radiation, thereby improving the quality of the data collected. An accelerating voltage of 45 kV and a 40 mA current were used, along with a 0.03 degrees 2θ-step and a hold time of 200 sec. Spectral analysis was performed using X'Pert HighScore Plus software (Panalytical, Netherlads). X-ray photoelectron spectroscoply (XPS)

characterization was performed using a Thermo K-Alpha XPS system (Thermo Scientific, USA) equipped with a Al Kα radiation as a source, with an energy resolution of 1 eV for the survey scans and 0.1 eV for high-resolution scans of individual characteristic peaks. The X-ray gun produced a 400 μm spot size, and an electron flood gun was used to minimize charging. The system vacuum level was below 10-8 Torr during the data collection. An emission angle of 90o was used. After being cycled, the cells were disassembled in a glove box and the removed electrodes were stored in DMC to avoid exposure to oxygen. While the samples were being loaded into the machine, additional DMC was poured on top of the sample to prevent oxidation before the test.

Transmission electron microscopy (TEM) reveals these nanoparticles deposited on the surface of the annealed CB to have a spherical shape with a diameter of ~25 nm. (Figure 4.20a). High-resolution TEM of these nanoparticles shows them to have a disordered microstructure (Figure 4.20b-c) – to be expected of nanoparticles deposited at a relatively low temperature. The interface between the Si particles and the annealed carbon surface shows a high contact angle, resulting in nearly spherical particles. The shape of the particles is most likely caused by the high Si-C interfacial energy – during the vapor decomposition process of CVD, once a stable nucleus has formed, growth can occur either by deposition of new atoms onto the surface of the substrate or onto the nucleus itself. High interfacial energy between the substrate and the deposited phase makes it more likely that new atoms will stick to the nucleus than the substrate, resulting in a high contact angle and highly spherical deposited particles. This may be a product of the highly graphitic surface of the carbon black, which has limited surface functionalization. The low deposition temperature also may have improved the smoothness of the deposited nanoparticles by reducing the surface mobility of Si atoms. These studies also reveal the post-deposition

carbon black structure to have the characteristic crystal structure of graphite, with a (002) interplanar spacing of .334 nm, as predicted theoretically. Energy-dispersive spectroscopy (EDS) demonstrated the particles to have a high degree of purity, lacking elemental spectra other than C, Si, O, and Cu (the latter provided by the copper substrate. This spectrum is shown in Figure 4.20d.

The surface forces may also be responsible for the granulation process. In a slurry, wet granulation occurs when a liquid binder wets small active particles during the agitation process, causing them to self-assemble into larger spheres, due to a combination of viscous and capillary forces. As the slurry dries, the binder solidifies, causing the granular shape of the agglomerates to become permanent.[71] When applied in Li-ion battery electrodes, the agglomerates must be designed with the intention of producing granules with high electrical conductivity, mechanical stability, and permeability to Li-ions/electrolyte. Graphitic carbon is an ideal binder material, and additionally helps prevent excessive oxidation of the Si nanoparticles. It can be produced either via chemical vapor deposition or by use of a liquid-phase hydrocarbon which is later dried, annealed and graphitized. Conventional wet granulation methods operate by introducing droplets of liquid binder, which penetrate into the powder surface and form nuclei, which then coalesce and bind the particles together into larger agglomerates. However, this process often produces a non-uniform distribution of binder, resulting in a similarly non-uniform range of granule sizes and densities. Therefore, graphitic carbon deposited via CVD is more likely to prove effective as a binder material.[71]

We found that the high temperature of carbon deposition dramatically improves the crystallite size of the deposited Si nanoparticles. X-ray diffraction (XRD) analysis of the produced samples showed the average grain size of the Si nanoparticles to be ~30 nm after C

coating (Figure 4.20e), indicating the deposited nanoparticles to have a large crystal grain size. The carbon black particles also improve in crystallinity somewhat after Si and C deposition, due to the high temperature of the process. This high crystallinity was confirmed by TEM studies (Figure 4.20f). The Si nanoparticles display a much more ordered crystal structure and a lower defect population.

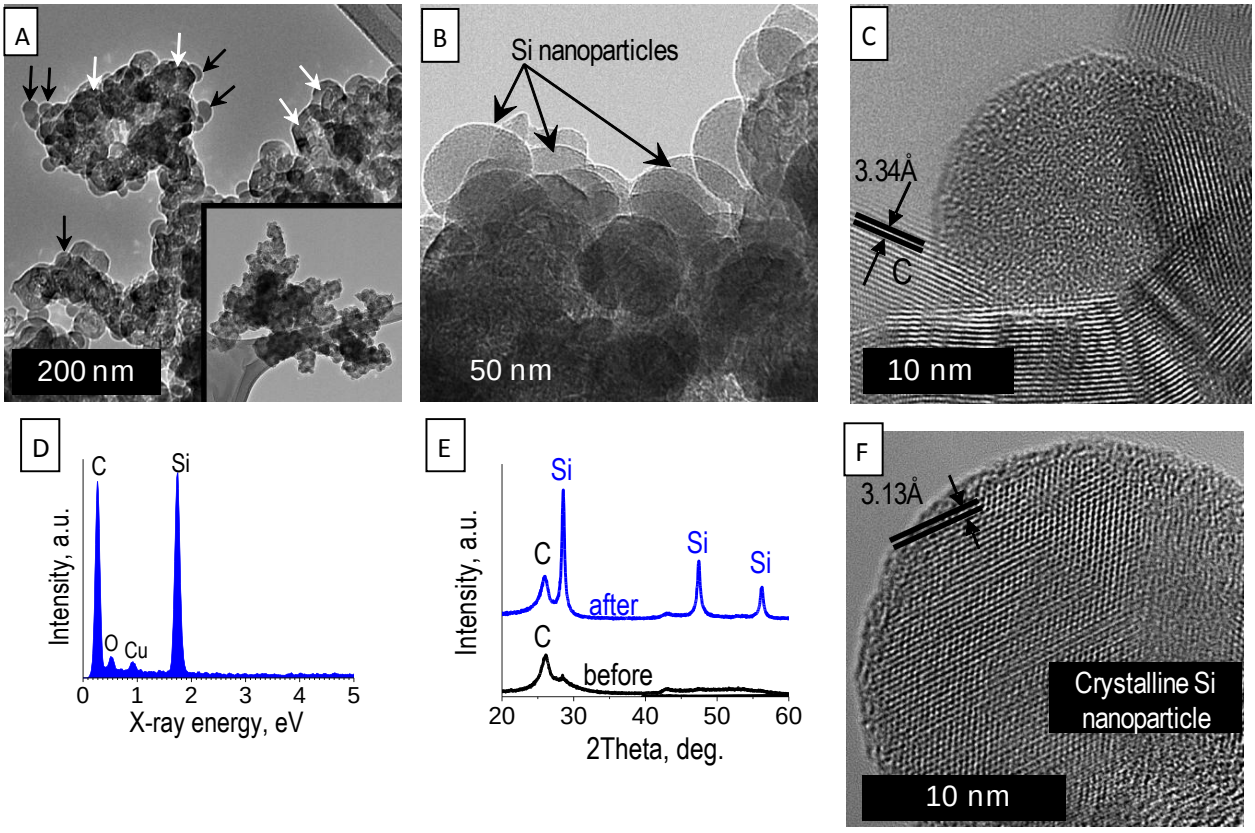

Figure 4.20: Structure of C - Si nanocomposites before and after granule self-assembly. a-c)**,** TEM micrographs recorded at different magnifications. In a), black arrows indicated spherical Si nanoparticles, while white arrows indicate the carbon black backbone. In c), we compare the highly ordered graphitized structure of the carbon black (after heat treatment) with the relatively disordered structure of the Si. In d), the EDS spectrum of the composite is shown, displaying the C, O, Si and Cu Kα lines. e) shows XRD spectra of Si-coated CB before and after C deposition at 700 °C for 30 min. In f), we see the HRTEM of the Si nanoparticle after the exposure to 700 °C, showing its improved crystallinity.

Examining the spherical granules produced during C deposition under SEM (Figs. 4.21a-b) shows the particle surface to be rough, with surface roughness of ~0.5-1 μm (Figs. 4.21b,c). The Si nanoparticles are still clearly visible through the C coatings. (Figure 4.21d) The diameter of the spheres produced ranges from ~15 to 35 μm, with an average particle size of ~26 μm. (Figure 4.21e) The granule size can be controlled by changing the deposition conditions, permitting optimization for specific applications.

It is believed that this CVD-induced granulation process is assisted by the complex process of propylene decomposition, which produces a number of intermediate products. During decomposition, several higher molecular weight compounds are formed, including toluene, ethylbenzene, styrene, naphthalene, biphenyl, and others. These intermediate compounds are adsorbed onto the substrate surface, rather than simply being produced and consumed in the gas phase.[73] These adsorbed decomposition products may act as a liquid agglomeration binder before they are carbonized. No further agitation proved necessary to create nanocomposite granules with an even distribution of size and density.

The bottom-up nature of granule assembly preserves the high specific surface area (SSA) of the activated carbon nanoparticles. Using N_2 gas sorption measurements (Figure 4.21f), we were able to show that the decrease in SSA was limited. The Brunauer-Emmett-Teller (BET) SSA of the particles after self-assembly was ~24 m^2/g, ~72% of the SSA before carbon deposition and self-assembly (33 m^2/g). The pore size distribution shows pores with diameter ranging between 30 and 100 nm (Figure 3g), within the range we previously indicated as ideal. These pores permit the full expansion of Si during Li alloy formation without increasing the overall volume of the particle. These pores are visible in the SEM micrographs of the granule

surface (Figure 4.21c,d). After C-coating, the pores are still visible, but the individual Si particles are not easily visible (Figure 4.21h).

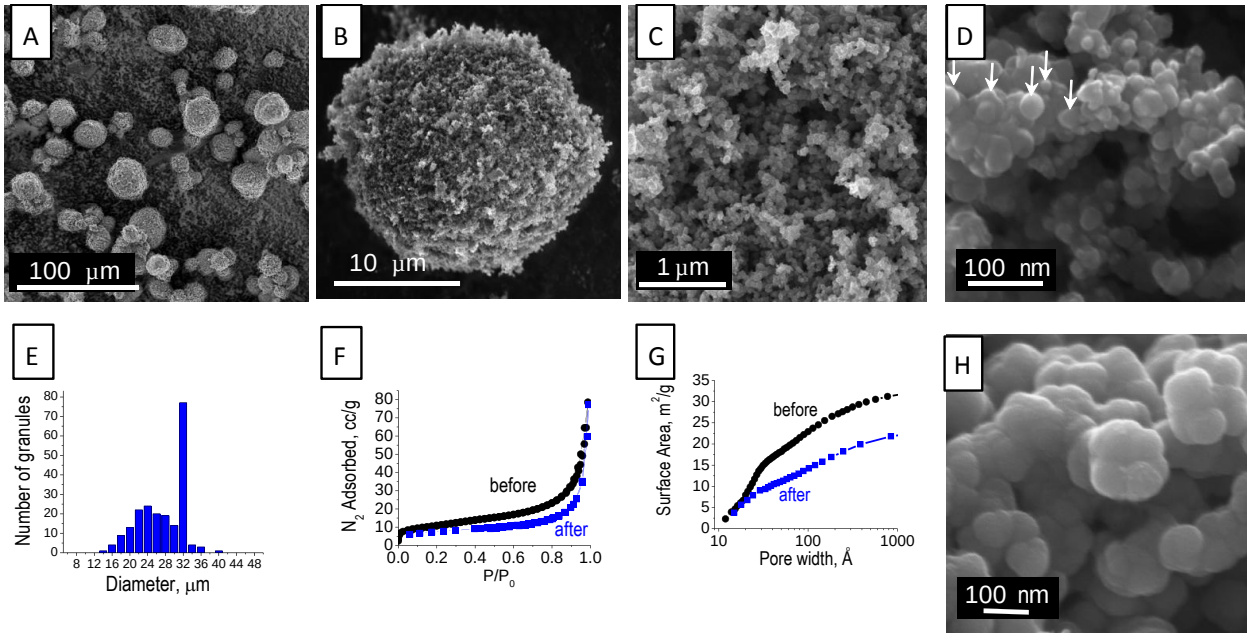

Figure 4.21: Structure of the C - Si nanocomposite spherical granules after self-assembly during C CVD. In a-d), SEM micrographs recorded at different magnification. The white arrows in d) point to C-coated Si nanoparticles visible on the surface of the granules. In e), the size distribution of the spherical granules synthesized at 700 °C. f) and g) show N2 sorption isotherms and BJH cumulative specific surface area for nanocomposites before and after C CVD. In h) a high-magnification SEM micrograph of the surface of the spherical granules produced during C-coating of pure CB, shown for comparison with d).

The surface area, pore size and particle size data described above was determined by analyzing nitrogen adsorption and desorption isotherms collected at 77 K using relative pressures of 0.0002-0.99 P/P_0, via a TriStar II 3020 (V1.03) surface area and porosity measurement system (Micromeritics Inc. , USA), effective for measurements of specific surface area (SSA) and pore size distribution (PSD) in the range of 2-100 nm. These analyses were performed on 50-100 mg of each powder, which was prepared by drying the powder under a vacuum at 80^{O} C for at least 12 h, followed by degassing under a N_2 gas flow at 300^{O} C for at least 2 h prior to weighing and gas sorption measurements. SSA and PSD were calculated using the Brunauer-Emmett-Teller

and Barrett-Joyner-Halenda methods, respectively. Micromeritics DataMaster software was used to perform the calculations. Isotherm measurements in the relative pressure range of P/P_0 from 0.05 to 0.3 was used for multi-point BET calculations. Our SEM studies were performed using a LEO 1530 SEM microscope (LEO, Japan, now Nano Technology Systems Division of Carl Zeiss SMT, USA). The in-lens secondary electron detector was used for these experiments. The experiments were performed using an accelerating voltage of 10 kV and a working distance of 8-9 mm.

Our working electrodes (anodes) were fabricated by casting a slurry containing an active material (C-Si composite granules or graphite or annealed CB), a binder (20 wt. % for annealed CB and for C-Si composite granules and 10 wt. % for graphite) and N-Methyl-2-pyrrolidone (NMP) on a 18 μm thick rough Cu foil (Fukuda, Japan). The electrodes were degassed in vacuum at 70 °C for 24 hours inside an Ar-filled glove box with < 1 ppm. of oxygen and water (Innovative Technology, Inc., USA) and were not exposed to air prior to assembling into the cells, in order to minimize water contaminations of the electrolyte. The commercial electrolyte we used was composed of 1M $LiPF_6$ salt in ethylene carbonate-diethyl carbonate-dimethyl carbonate mixture (EC:DEC:DMC=1:1:1 vol %) (Novolyte Technologies, USA). Lithium metal foil (~1 mm thick) was used as a counter electrode. The electrochemical measurements were performed suing 2016 stainless steel coin cells we assembled in the glove box. In order to improve electrical contact, the working electrode was spot-welded to the coin cell. The charge and discharge rates we used during measurements were calculated assuming the theoretical capacities for C and Si, given the composition of the active material (either C or C-Si mixture). Coulombic efficiency was calculated as

$$100\% \cdot \left(\frac{C^{dealloy}}{C^{alloy}}\right),$$

where C^{alloy} and $C^{dealloy}$ are the Li insertion/extraction capacity of the anodes.

Results

The nanocomposite samples we tested were ~50 wt% Si, with a theoretical capacity of ~2225 mAh/g (assuming a Si theoretical capacity of 4200 mAh/g, with full lithiation to $Li_{4.4}Si$). The specific reversible deintercalation capacity of the sample for the first C/20 charge/discharge rate is ~1950 mAh/g. (Figure 4.22a,c). This capacity is over 5 times higher than the theoretical capacity of graphite (376 mAh/g), and over 10 times that of the annealed carbon black (Figs. 4a,b, S2). The specific capacity of the Si nanoparticles is at least ~3650 mAh/g, an extremely high value, indicating that alloys with high Li content are being formed within the nanocomposite particles. This suggests that there is sufficient pore space to permit the full expansion of the lithiated Si nanoparticles. This also suggests that the Si nanoparticles are highly accessible to Li insertion. The irreversible capacity losses in the first cycle (Figure 4.22a) are a product of SEI formation, and are fairly low (~15%), particularly when compared to the irreversible capacity losses incurred during cycling of carbon black (Figure 4.22b). Cycled repeatedly at C/20 rates, the material exhibits Coulombic efficiency of approximately 97%, and a capacity fading rate of ~0.4% per cycle. While the efficiency is below acceptable levels, this degree of capacity loss is on par with conventional graphitic materials, and indistinguishable from the capacity losses produced by dendritization of the Li counter electrode surface. (Figure 4.22c)

Cycled at faster speeds, the samples demonstrated exceptional high-rate capability, despite the low diffusivity and generally slow kinetics of Si. The specific discharge capacity of

the composite anodes was 1590 (82% of the C/20 capacity) and 870 (45% of the C/20 capacity) mAh/g at C/1 and 8C respectively. This excellent capacity retention far exceeds the performance of graphitic anode materials at similarly high rates, despite graphite's high Li-ion diffusivity and low overall capacity. Cycled at C/1, the cell retained a capacity of ~1500 mAh/g for over 100 cycles. At an 8C rate, with a specific current of 2.98 A/g, graphitic carbon exhibited a deintercalation capacity of ~40 mAh/g, 13% of the C/20 specific capacity. At the same specific current value, the 50% Si nanocomposite material exhibited capacity of more than 1500 mAh/g, over 37 times higher than graphitic carbon. This suggests that neither Li-ion access nor volumetric capacity are issues in these materials.

Analyzing the differential capacity vs. voltage curves derived from charge and discharge of our nanocomposite, we see two broad lithiation peaks at 0.21 and 0.06 V, and a narrower delithiation peak at 0.5 V (Figure 4.22d). Normally, a C delithiation peak would be visible at 0.2 V, but in this case it is too small to be visible, due to the minimal contribution of carbon to the overall anode capacity. In micron-scale Si powder or nanowires, a delithiation peak is typically observed at 0.3 V, but is not present in the capacity vs. voltage curves for our samples.[74, 75] This suggests that there is no transition between amorphous and crystalline phases in the nanoSi particles in our composites. From the increase in the height of the 0.5 V delithiation peak after the first cycle, we can surmise that the Li extraction kinetics improve after repeated cycles. Amorphous Si-Li alloy formation begins once Li is inserted into the crystalline Si, at 0.1 V. This is in agreement with previous examples of nanowire lithiation. The lithiation peak at 0.21 V is a product of the phase transition between different amorphous Si-Li phases.[74]

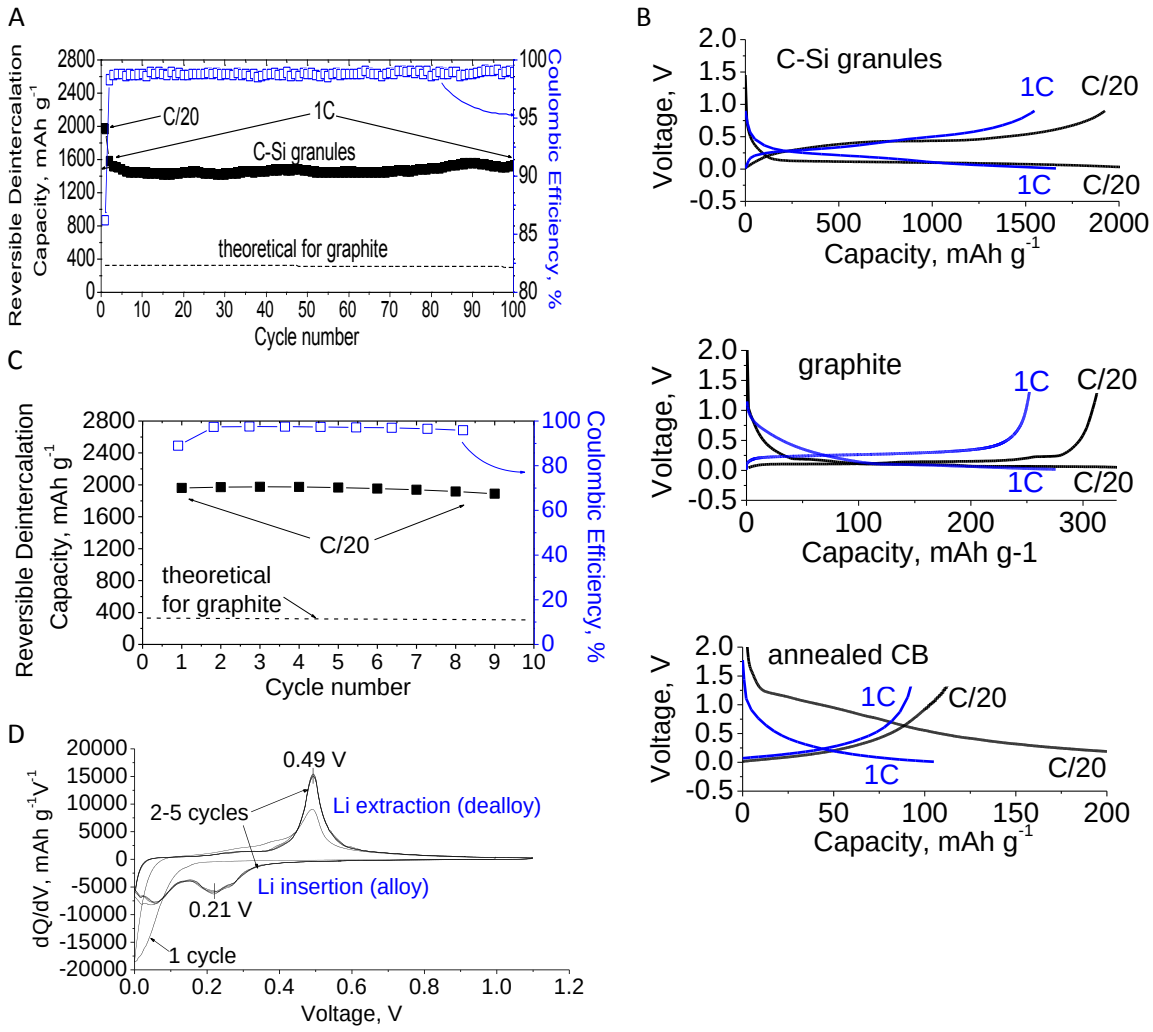

Figure 4.22: Electrochemical performance of the C - Si self-assembled nanocomposite spherical granules. In a), the reversible Li deintercalation capacity and Coulombic efficiency of the C-Si granule electrode vs. cycle number is shown. In b), Galvanostatic charge-discharge profiles of the C-Si granule electrode at rates of ~C/20 and 1C are shown, compared to that of the annealed CB and commercial graphite – based electrodes between 0 and 1.1 V. c) shows the C/20 performance of the C-Si granules d) shows the differential capacity curves of the C-Si granule electrode in the potential window of 0-1.1 V.

The pores in the composite granules produced by self-assembly permit efficient and stable anode performance by buffering the expansion of Si during Li insertion, as previously discussed. We have performed SEM studies of the anode particles after cycling, in which we can see the exceptional robustness of the granules. (Figure 4.23) The granular anode particles remain

intact, even after many cycles. One potential factor permitting these materials to accept such high stresses is the relatively disordered structure of the self-assembed granule. While the pore size is fairly consistent, the pores themselves are complex and branching. As a result, if the path of Li-ions is blocked or impeded in one pore by a fully lithiated Si nanoparticle or by an area of exceptionally thick solid-electrolyte interphase (SEI), the interconnected aperiodic network of pores will permit the ions to migrate through another channel, allowing the particles to rapidly charge more easily. In the case of highly ordered 1D channels, a blocked pore could potentially cause dramatically increased impedance. A limited degree of disorder is an advantage in some other composite materials, such as some photonic crystals and catalytic structures. [76, 77]

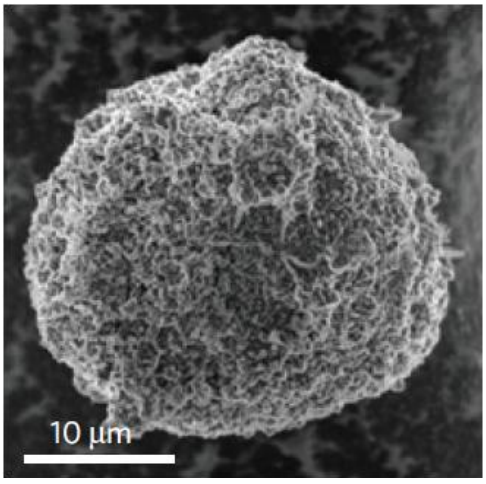

Figure 4.23: SEM micrograph of C-Si self-assembled granule after cycling

We can develop a better understanding of the evolution of the SEI through XPS analysis. For this purpose, we have performed XPS analysis of our samples after different numbers of cycles. These samples were initially cycled at C/20 between 0.01 and 1.99 V for 2 cycles, and were then cycled at C/2 for an additional 200 cycles. Samples were tested via XPS at 10, 30, 50, 100 and 200 cycles. Examining the C1s high-resolution scan, we find that the final carbon

chemical state composition of the electrode at 100 and 200 cycles is similar to its initial state at 10 cycles – at 100 and 200 cycles, the C-H to C-O content ratio is slightly higher than it is at 10, suggesting a slight improvement in the chemical stability of the final SEI, but the differences are fairly small. However, there is a dramatic change in the chemical state composition at 30 and 50 cycles from the initial state. At 30 cycles, the C-O_3 to C-O and C-H to C-O content ratios both drop significantly, suggesting the SEI becomes substantially richer in semicarbonates and other, less stable SEI components, rather than relatively inactive polymeric compounds and lithium carbonate. At 50 cycles, the changes occurring in the SEI reverse themselves – the C-O_3 to C-O ratio spikes up to almost double its initial value, and the C-H to C-O ratio increases as well, albeit not as dramatically. These changes stabilize between 50 and 100 cycles, leaving the SEI in the state it initially occupied at 10 cycles, indicating long-term chemical stability. This data is summarized in Figure 4.24a.

Examining the high-resolution scans of other elements, we see similar effects. The O1s scans reveal that there is a dramatic increase in semicarbonate content between 10 cycles and 30 cycles. This increase in semicarbonate content could be a product of the decomposition of stable SEI compounds into relatively unstable forms. This effect eventually reverses itself, leaving the oxygen chemical state content of the SEI at its initial, 10 cycle composition by 200 cycles. The F1s high-resolution scan shows a substantial decrease in LiF content between 10 and 30 cycles. It is unlikely that LiF could decompose into another form due to its exceptional stability, so we can assume that this drop is a result of the SEI getting thicker – in a typical SEI, LiF is primarily at the bottom of the film, in contact with the surface. An increase in SEI thickness would also produce an apparent drop in LiF content. The LiF content apparently increases between 30 and 50 cycles; this increase may be caused by the opposite effect, as the SEI becomes thinner. By

200 cycles, the LiF content of the SEI has returned to its initial levels. The P2p high-resolution scan repeats this pattern – a drop in phosphate content between 30 and 50 cycles, and a spike in phosphate content between 50 and 100 cycles, followed by a return to the initial values at 200 cycles. These spectra are shown in Figure 4.24b-d. From this data, we may speculate that the SEI becomes significantly thicker between 10 and 30 cycles, and develops a higher content of less stable compounds. Between 30 and 100 cycles, these compounds slowly disappear, eventually leaving the SEI substantially thinner than it was initially. By 200 cycles, the SEI has returned to its initial, stable composition and thickness.

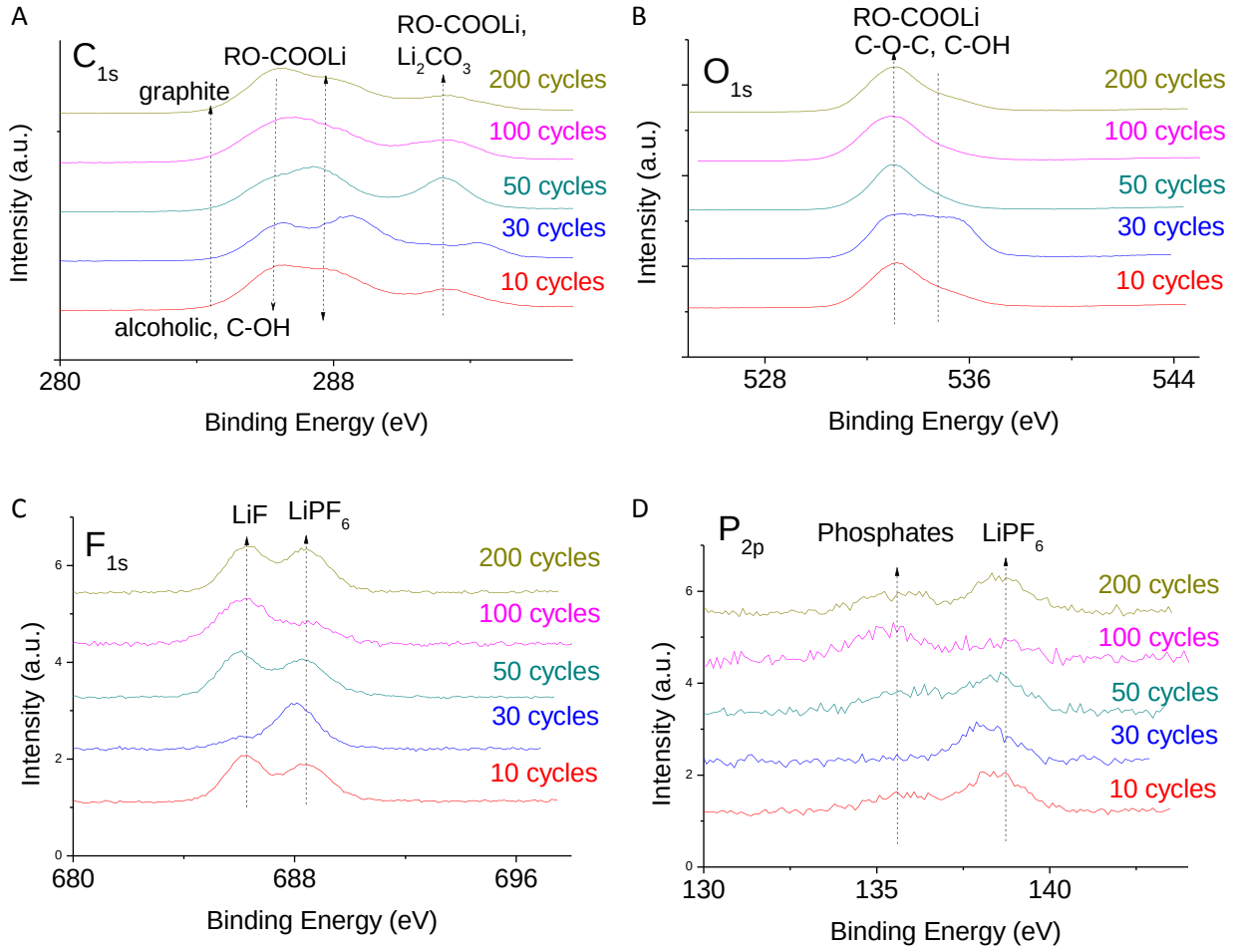

Figure 4.24: High-resolution XPS spectra for self-assembled granular Si-C nanocomposite; a) C1s, b) O1s, c) F1s, d) P2p, after 10, 30, 50, 100 and 200 cycles

Conclusions

We have developed methods for producing and characterizing template-based and self-assembled nanocomposite particles, and examined their electrochemical performance for energy storage applications. We have analyzed the effects of annealing and surface coating on the performance of these materials. We have demonstrated that it is possible to apply the rational electrode design methods we developed in our studies of nanocomposites derived from sacrificial templates to more commercially useful materials. These nanocomposite materials possess exceptional potential possessing high capacity and rapid charge-discharge capabilities, and can be produced and handled easily and safely.

5. Novel Binder Materials for Si-Based Anodes – XPS Studies

5.1 Overview

The surface chemistry of an electrode has a significant impact on the electrochemical performance of a cell. In particular, the physical and chemical stability of the SEI is important – when the SEI is unstable, the electrode's electrochemical performance can suffer significantly, as impedance increases and Coulombic efficiency decreases. We have analyzed the impact of several parameters on the stability of the SEI for conventional and nanocomposite electrodes, including the effect of a range of different binder chemistries. We have also analyzed the effect of surface stresses produced by Si nanoparticle lithiation and expansion in materials with advanced binders. The results of these studies can be applied to improve design of a range of other nanocomposite materials.

5.2 Impact of Binders on SEI Performance

Approach

As previously discussed in our literature review, the expansion and contraction produced during lithiation and delithiation of Si nanoparticles produces unique demands on the binder materials used in an electrode to hold the active anode materials together. The binder used in most research studies and commercial products is poly(vinyldene fluoride) (PVDF), which attaches to Si particles only via weak van-der-Waals forces, and which therefore fails to accommodate the large changes in particle diameter and interparticle spacing producing by the expansion and contraction of the particles. As a result, it will rapidly become ineffective in holding the particles together and ensuring electrical conductivity within the anode, without which battery operation will inevitably fail.[78-81] Development of improved binder materials is necessary to make stable high-capacity anodes possible.

Most of the studies to date have been focused on the variants of PVDF or carboxymethylcellulose (CMC)-based binders. Some of these experiments have shown progress - heat treatment of PVDF-based Si-C anodes (with 80 wt% Si) in argon at 300-350^{o} C has been found to significantly improve the binder's adhesion to both Si particles and to the Cu foil current collector, thereby significantly improving the stability of the battery during cycling.[82] Modified PVDF binders have also proven valuable - a PVDF-tetrafluoroethylene-propylene (PVDF-TFE-P) binder used with a C-$Si_{0.64}Sn_{0.36}$ composite anode, heat treated at 110^{o} C for 24 hours in Ar, enabled stable performance with 800 mAh/g capacity up to 40 cycles . The modifications to the binder improved its performance via cross-linking, increasing its strength and elastic modulus. An adhesion-promoting agent (3-aminopropyltriethoxysilane) was used to improve adhesion between the binder and the composite active particles.[83]

CMC has also been studied as a binder material for Si-based anodes, as CMC binders typically exhibit better performance than PVDF binders. A combination of a commercial adhesive and sodium CMC (Na-CMC) in a 2:1 ratio has proven somewhat successful in C/nano-Si batteries, exhibiting 500 mAh/g capacity with less than 20% degradation after 50 cycles. [84] Similarly, a 1:1 combination of Na-CMC and commercial butadiene block co-polymer (SBR) latex performed well when used with 1-3 micron C-coated Si particles (62 wt% Si, 30 wt% C, 8 wt% binder) Under constant lithiation to 1000 mAh/g, the electrodes demonstrated stable performance for 50 cycles. [50] A similar mixed binder has been used to produce C/nano-Si composite anodes prepared via a direct mixture of C and nano-Si (Si:C≈1:9) These electrodes exhibited stable performance for up to 150 cycles, with discharge capacity decreasing from an initial value of 700 mAh/g to 550. Only 2 wt% binder was used in this case; the effects of larger

binder content were not investigated, under the assumption that this would hinder the diffusion of Li^+ ions. [85]

Studies have compared the performance of Na-CMC by itself and SBR/Na-CMC (1:1) binders. Macroscopic (8 μm, 325 mesh) Si powders were used, with conductive additives (Si:C:binder= 80:12:8). In this study, the lower potential was limited to 170 mV (vs. Li/Li^+). Pure CMC binders exhibited superior performance, with electrode deintercalation capacity maintaining ~56% of its initial 1600 mAh/g capacity after 80 cycles. In some of the CMC samples, the electrodes exhibited oscillating charge/discharge behavior, with specific capacity fluctuating betweeen 1300 and 1100 mAh/g during 70 cycles.[51] In subsequent studies, it was suggested that extreme Na-CMC binder content (~70%) might provide sufficient buffering to permit full expansion of Si particles. Anodes containing 20 wt% Si, 10 wt% conductive additives, and 70 wt% Na-CMC exhibited only 25% capacity fading between the 3rd and 200th cycle. However, the overall anode capacity was below 400 mAh/g due to the low volumetric capacity of Si within the electrode. When higher Si and C and lower binder contents were employed (33 wt. % Si, 33 wt. % C, 33 wt. % binder), significantly higher capacity was realized (1200 mAh/g), but this high capacity faded rapidly (25% in 25 cycles.[52] When the pH of the Na-CMC is optimized to improve particle dispersion, it has proven possible to achieve up to 700 cycles when intercalation capacity is capped at 960 mAh/g (approximately 1/3 of the total capacity of Si) to minimize the stress and volume changes within the electrode. [53]

Na-CMC has certain limitations as a binder for Si anodes, however. First, it is insoluble in organic solvents. Aqueous solvents, while environmentally friendly, can increase surface oxidation of Si and affect the Coulombic efficiency and long-term stability of the anode. More problematically, the mechanical properties of Na-CMC cannot be altered by chemical

modification, making it impossible to tailor the binder for optimal use with Si anodes. As a result, high stability can only be achieved when Li insertion capacity is limited to control the volume changes of the Si particles. In order to tap the full potential of Si binder materials, we must explore new binder chemistries.[53] One potential factor in the excellent performance of CMC as a binder is its high density of carboxyl groups. It has been proposed that these groups permit a degree of self-repair in the adhesion between the silicon and carbon surfaces, as the adhesion between the two can reform if it is broken.[86]

Two other binder materials for Si-based anodes will be discussed here: polyacrylic acid (PAA) and alginate (derived from brown algae). Both of these materials offer improved anode stability, optimizable mechanical properties, and other valuable qualities. Both of these materials are soluble both in water and in a variety of ecologically friendly organic solvents, such as ethanol. Both of these materials have a higher concentration of carboxyl functional groups than CMC, allowing for better adhesion. The spacing between these groups, as well as the mechanical properties of the binder, can potentially be controlled via copolymerization with other monomers, as can swelling and solubility in a solvent. There are several additional advantages to alginates as a binder material. Alginate is derived from marine plants (algae), which are grown on non-agricultural land, such as salt water or waste-water land. They can yield high biomass with relatively little area to grow on. As such, they can be produced more cheaply and ecologically than normal polymer binders. Alginates are produced from algae via baking brown seaweed in a hot soda (Na_2CO_3) solution, which typically produces alginate in a sodium salt form.

Chemically speaking, PAA and alginate are dissimilar. PAA has a relatively simple chemical structure, repeating a single unit of acrylic acid as a monomer (Figure 5.1a). Alginic

acid, however, is a linear copolymer of (1-4)-linked β-D-mannuronic acid (M) and α-L-guluronic acid (G) residues (Figure 5.1b). The properties of alginic acid polymers can be manipulated by varying the compositions and sequences of M and G monoblocks – a property used by brown algae to improve their survivability in a range of natural conditions. For example, algae growing in coastal areas have a higher content of G monoblocks compared to algae growing in streaming waters. This higher content of G acid makes alginate gels more rigid. Other tools, such as ion exposure or enzymatic post-modification, can alter the structure of the polymer, making it highly versatile. PAA binders can also be manipulated to control their properties - potentially, PAA binders could even be produced with block and graft copolymer architecture, allowing the fabrication of electrodes with a three-dimensionally controlled structure.[87, 88]

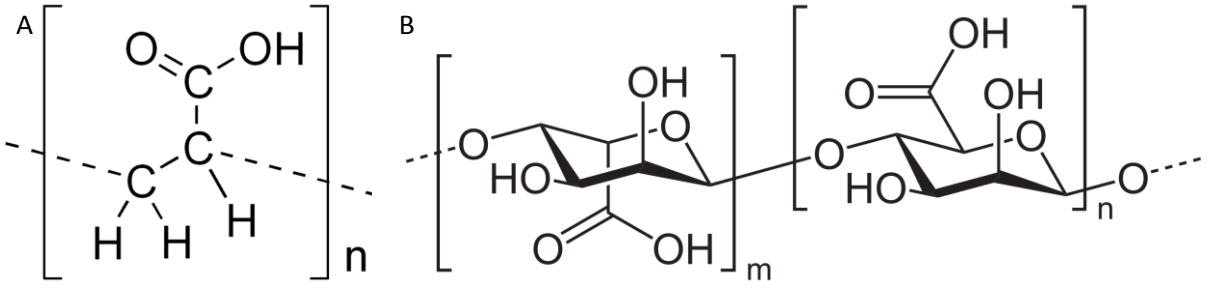

Figure 5.1: Comparison of monomeric structure of a) poly(acrylic acid) and copolymer blocks of b) alginate.

The precise control over functional group distribution and the controllability of mechanical properties make these materials a valuable source of new solutions to the problems associated with Si-based anodes. These new materials can potentially provide new methods for preparing and optimizating electrodes for specific processes. Furthermore, these materials can serve as model systems and thereby provide valuable information on the effects of binder properties, such as elasticity, electrolyte swelling, surface chemistry, adhesion strength, and others.

Experimental Methods

The primary active material of our electrodes was Si nanopowder, purchased from Hefei Kaier Nanotechnology Development Co., China. In order to remove the thick SiO_2 passivation layer on the nanoparticles (up to 70 wt%, according to energy dispersive spectroscopy (EDS) spectra), the nanoparticles were purified using a 50% HF solution. The nano-Si used in combination with the alginate electrodes was purchased from a different source (NP-Si-L50, 98 % purity, MTI Corporation, USA). Some of the nano-Si samples were then coated with carbon. This process was implemented by dispersion of the nanoparticles in tetrahydrofuran in an ultrasonic bath (Branson, USA). After dispersion, the particles were mixed with polycarbonate (PC) (Mw=64,000, Sigma-Aldrich, USA) in a solution in THF, ensuring thorough mixing via continuous flask rotation (100 rpm). In order to achieve a uniform coating of PC on the particle surface, the THF solvent was slowly replaced with ethanol, causing a uniform PC coating to form on the powder surface. After being removed from solution via high-speed centrifuge (5000 rpm, Fischer Scientific, USA), the PC layer on the particle surface was graphitzed by annealing under Ar flow (50 sccm) for 2 h at 800 °C.

The samples were characterized via scanning electron microscopy (SEM) and EDS studies, which were performed using a LEO 1530 SEM microscope (LEO, Japan, now Nano Technology Systems Division of Carl Zeiss SMT, USA). In-lens secondary electron detectors were used for imaging, and most of the imaging took place at an accelerating voltage of 6 kV and a working distance of 5 mm. Nuclear Magnetic Resonance was used to characterize the ratio of M-to-G monoblocks in the alginic acid used as a binder in this experiment. These tests were performed by dissolving our sodium alginate samples in D_2O and freeze-drying them twice to

remove any excess exchangeable protons. The final concentration of alginate in D_2O used for the NMR measurements was 5 g/L. The 256 spectra examined were collected on a Bruken Avance 500 NMR spectrometer at 80^o C and averaged. The HOD signal in the spectrum was suppressed using the WATERGATE pulse sequence. These studies reveal this ratio to be 1.13. This ratio was calculated based on integration of the peaks at 4.7, 5.3 and 5.7 ppm (Figure 5.2).

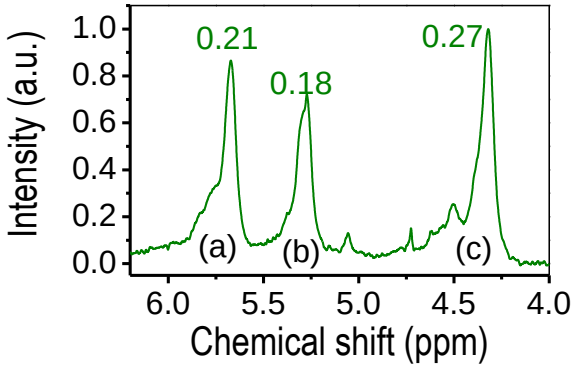

Figure 5.2: 1H-NMR spectrum of Na-alginate; numbers above peaks correspond to peak integrated intensities

We used PAA (Sigma-Aldrich, USA) with molecular weight of 100000 g/mol dissolved in ethanol and sodium alginate dissolved in H_2O as binders. PVDF dissolved in N-Methyl-2-pyrrolidone (NMP) (9305, Kureha, Japan) and Na-CMC with Mw = 500000 g/mol (Alfa Aesar, USA) dissolved in H_2O (with small quantities of ethanol used as a surfactant) were used as alternative binders, for purposes of comparison with PAA. All of the electrodes (other than those based on sodium alginate) contained 15 wt. % of binder, 43 wt% of Si and 42 wt% of C, either entirely as conductive additives – specifically, high-temperature annealed carbon black (Superior Graphite, USA) – or as a combination of surface coating (17 wt%) and additives (25 wt%). The electrode slurries were mixed at 600 rpm using a laboratory stirrer, after an ultrasonic bath was used to ensure effective nanoparticle dispersion. The sodium alginate electrode contained 15 wt% of binder, 64% of Si, and 21% of carbon conductive additives. After mixing, the slurries

were cast onto an 18 µm Cu foil (Fukuda, Japan) in a 150 µm thick layer. Subsequently, the cast electrodes went through a multi-stage drying process: first being dried in air at room temperature , followed by drying at 60^{O} C for at least 4 hours. Subsequently, they were degassed in vacuum at 70^{O} C for 2 hours inside an Ar-filled glove box with <1 ppm of oxygen and water (Innovative Technology, Inc., USA), avoiding exposure to air prior to cell assembly.

We used a commercial electrolyte, composed of 1M $LiPF_6$ salt in a mixture of ethylene carbonate – diethyl carbonate – dimethyl carbonate (EC:DEC:DMC = 1:1:1 vol. %) (Novolyte Technologies, USA). The counter electrode used was lithium metal foil (1 mm thick, Alfa Aesar, USA). We used 2016 stainless steel coin cells for electrochemical measurements. We spotwelded the Cu foil current collector to the coin cell to improve the electrical contact. We calculated charge and discharge rates assuming a theoretical capacity of 4200 mAh/g for the Si and an experimentally determined capacity of 150 mAh/g for the C, determining the capacity of the electrode based on the ratio of Si to C in it. We cycled the cell between 0.01 and 1 V vs. Li/Li^{+}.

We calculated Coulombic efficiency as $100\% \cdot (\frac{C^{dealloy}}{C^{alloy}})$, where C^{alloy} and $C^{dealloy}$ are the capacity of the anodes for Li insertion and extraction. We used Arbin SB2000 (Arbin Instruments, USA) and Solartron 1480 (Solartron Analytical, USA) multi-channel potentiostats for electrochemical measurements. When specific capacity is reported, we report only the contribution from Si; the contribution of C is subtracted from the results. The actual specific capacity is ~50% lower, due to the inert nature of the binder and the low capacity of the C.

We studied thin films of all three binders (PAA Na-CMC, and PVDF) deposited on Si wafers via ellipsometry. We also studied films of PAA at lower molecular weight than those we used for the cells – Mw = 2000 g/mol and 5000 g/mol. These studies were performed with a COMPEL

automatic ellipsometer (InOmTech, Inc., USA) at an angle of incidence of 70^{o}. We used Si wafers without a coating as a reference sample. These test allowed us to analyze the swelling of polymer binders in carbonates. The binder films were deposited on the Si wafer using a dip-coating method, producing an initial film thickness of 30-70 nm. The wafers were tested by being placed in a closed chamber with an open container filled with pure DEC - the effects of EC were neglected, since EC is solid and less volatile. We performed film thickness measurements periodically, until the carbonate absorbed by the film was in equilibrium with the DEC vapor in the atmosphere, at which point the changes in ellipsometric parameters ceased. The thickness of the film was determined by fitting the ellipsometric data, assuming the refractive index of the binder to be 1.5

We measured the mechanical properties of the three binders via atomic force microscopy (AFM). These studies were performed using a Dimension 3100 (Digital Instruments Inc., USA) microscope. We collected force-distance data using silicone cantilevers with a spring constant of 40 N/m with approaching-retracting probing frequency of 1-2 Hz. We derived force-volume measurements from this data, which were then used to obtain the distribution of stiffness over the surface of the sample. We performed these measurements on samples in both dry and wet states – wet samples were immersed in DEC before measurements. We used PVDF in a dry state as a reference, and normalized the stiffness data against this standard.[89]

X-ray photoelectron spectroscoply (XPS) characterization was performed using a Thermo K-Alpha XPS system (Thermo Scientific, USA) equipped with a Al Kα radiation as a source, with an energy resolution of 1 eV for the survey scans and 0.1 eV for high-resolution scans of individual characteristic peaks. The X-ray gun produced a 400 μm spot size, and an electron flood gun was used to minimize charging. The system vacuum level was below 10^{-8} Torr during

the data collection. An emission angle of 90^{o} was used. After being cycled, the cells were disassembled in a glove box and the electrodes were removed and stored in DMC to avoid exposure to oxygen. While the samples were being loaded into the machine, additional DMC was poured on top of the sample to prevent oxidation before the test.

Results and Discussion

Our SEM studies show a broad size distribution in the Si nanopowder, with particles ranging in size from 20 nm to 1 micron. However, the average size of the particles was 100-400 nm. (Figure 5.3a) The Si nanoparticles used in our alginate electrodes had a smaller particle size, ranging from 20 to 100 nm, with an average of ~37 nm. (Figure 5.3b) Carbon coating proved to be both conformal and uniform throughout the powder (Figure 5.3c). The content of deposited C was 25-30 wt. %, according to both our estimates from the mass change of the powder and EDS measurements performed during microscopy. Oxygen was additionally detected by EDS (Figure 5.3d-e), and is assumed to come from the remaining oxide layer (post HF etching) and the physisorbed water.

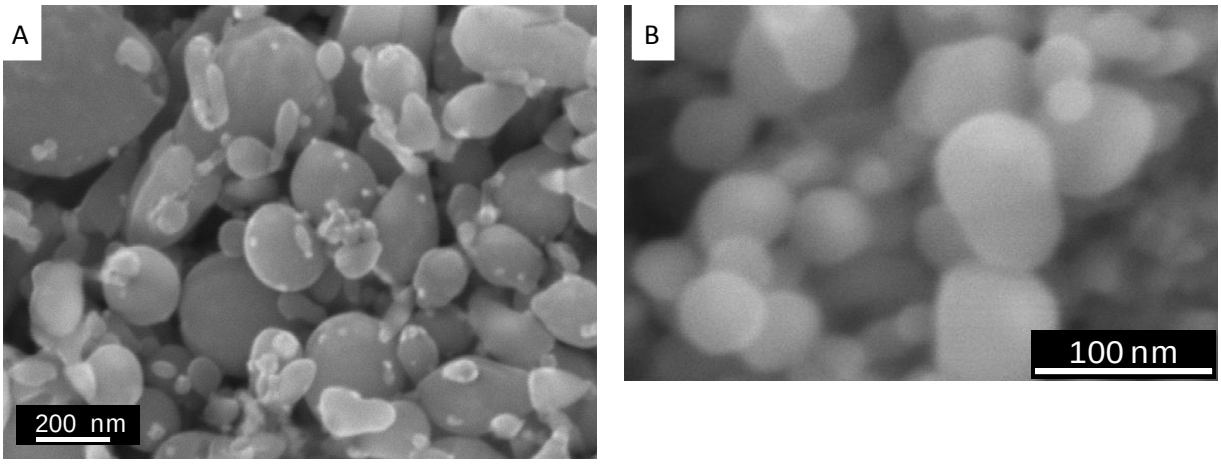

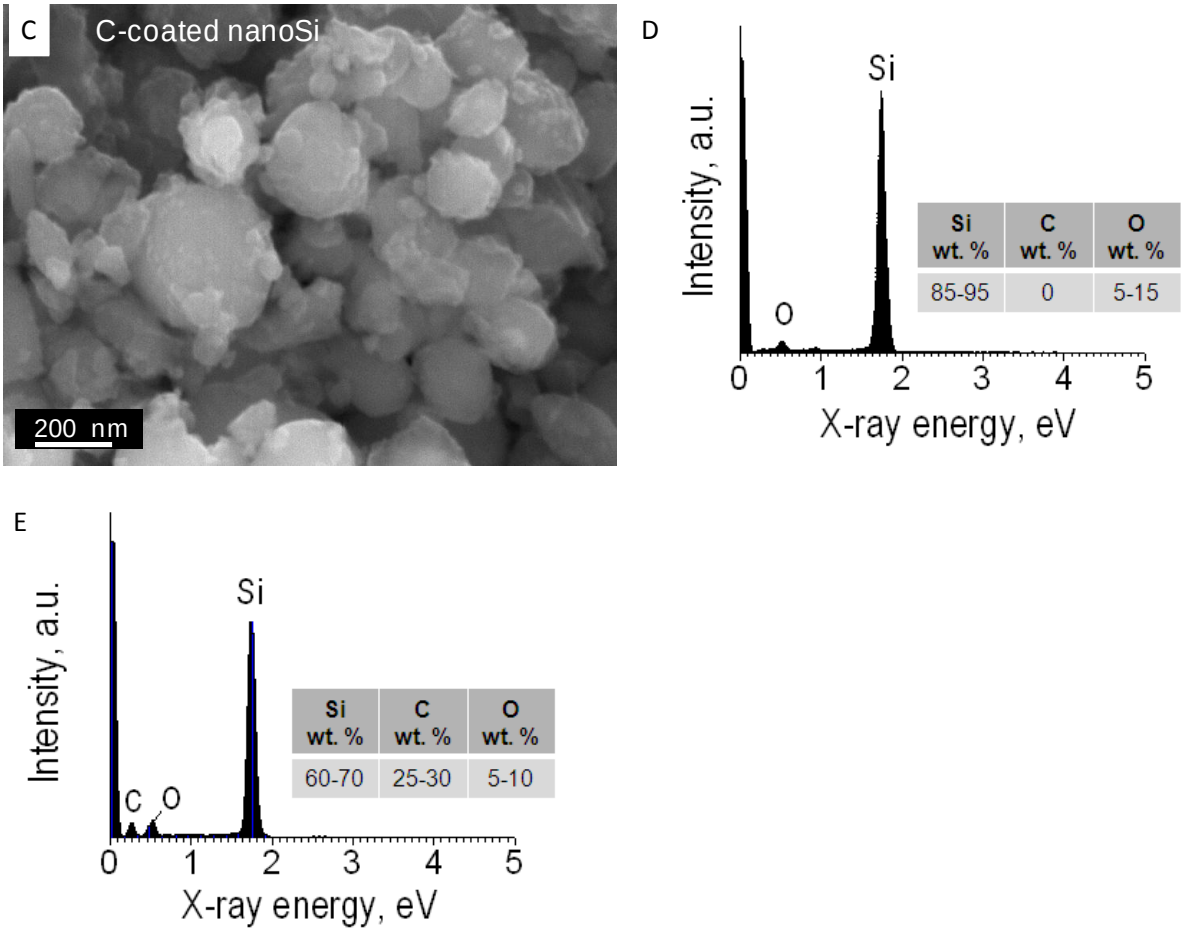

Figure 5.3: Structure of nano-Si, before and after carbon coating. a) High-magnification SEM of nano-Si used in PAA and CMC electrodes; b) High-magnification SEM of nano-Si used in alginate electrode; c) nano-Si from a) after carbon coating; d) EDS spectrum from nano-Si before coating; e) EDS spectrum of after coating

We consider 4 factors to be of the most importance in determining the performance of a polymer binder: (i) the strength of the adhesion between the electrode and the current collector foil, (ii) the interface between the polymer and the active particles, (iii) the interaction of the binder with the electrolyte, and (iv) the mechanical properties of the binder. Alginate, Na-CMC and PAA polymers exhibit superior performance in areas (i) and (ii), due to their high content of carboxy functional groups. These functional groups interact strongly with the passivating SiO_2

on the Si nanoparticles or the similar Cu oxide layer on the current collector via hydrogen bonding.

However, we have yet to fully understand the effects of the interface between the binder and the Si, or the effects of binder-electrolyte interaction and the influence of mechanical properties. In terms of mechanical properties, Alginate has the highest reported fracture strength, σ_b, at 147 MPa. For PAA, σ_b is reported to be about 90 MPa, while the σ_b of Na-CMC is reported to be 30 MPa, and PVDF has only a slightly higher σ_b, at only 37 MPa. PVDF has the highest degree of elasticity, exhibiting 50% elongation at fracture, while alginate exhibits ~33% elongation at fracture. Na-CMC exhibits only 6% elongation, and PAA is estimated to have similarly brittle mechanical behavior. [90-93]

Our analysis of the swellability of the binders under analysis in DEC vapor allowed us to evaluate the binder-electrolyte interaction. These samples were dried, and then placed in an ellipsometer with an atmosphere saturated with DEC vapor, causing them to slowly and measurably swell during testing. We see the changes in polymer film thickness measured via ellipsometry for alginate, PAA, Na-CMC and PVDF upon exposure to DEC vapor in Figure 5.4. Since the solubility (and swellability) of the polymer in a solvent depends on polymer molecular weight, we studied several PAA samples, including those with Mw substantially lower than the ones used in the binder. However, the PAA films showed only very limited swellability (~1%), without a strong dependence on Mw. The alginate film actually reduced in thickness slightly – possibly due to a shift in the refractive index of air or the displacement of absorbed water. The minimal swellability of Alginate and PAA indicates a limited degree of polymer/electrolyte interaction. Similarly, the Na-CMC film exhibited limited swellability in DEC vapor. We believe this indicates that the mechanical properties of these binders will not change significantly during

cycling. However, the PVDF binder film absorbed large quantities of carbonate vapor, exhibiting a change in thickness of up to 20%. As a result, we expect that there may be a significant change in the mechanical properties of PVDF during cycling, as a result of absorption of electrolyte.

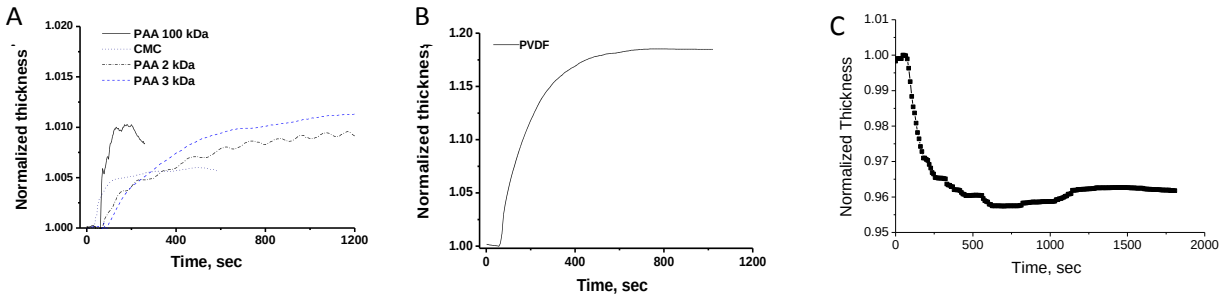

Figure 5.4: Ellipsometric data for a) CMC and PAA of varying molecular weights; b) PVDF; and c) Alginate

Our AFM studies have allowed us to confirm our ellipsometric measurements. We studied the stiffness of PVDF, CMC, PAA and alginate, both dry and after immersion in DEC using AFM indentation measurements. We found that, in a dry state, alginate, PAA and Na-CMC exhibit significantly higher stiffness than PVDF (Figure 5.5), as predicted by the literature. The Young's modulus of PAA is reported to be ~4000 MPa, and Na-CMC and alginate exhibit a similar level of stiffness in our studies. Conversely, PVDF exhibits a much lower degree of stiffness, similar to the value reported in the literature – 650 MPa. [90, 91, 93] The alginate, PAA and Na-CMC films treated with DEC did not change in stiffness dramatically; the alginate film, in particular, did not change at all. However, the stiffness of the PVDF film did decrease significantly after absorption of DEC, as we expected from our ellipsometry measurements. We expect that, in the electrolyte solution, the PVDF binder will exhibit significantly reduced resistance to elastic and plastic deformation. This may explain the poor performance previously noted in Si anodes using PVDF binders, since the binder would deform easily during silicon lithiation and delithiation, leading to fracture and a loss of electrical contact.

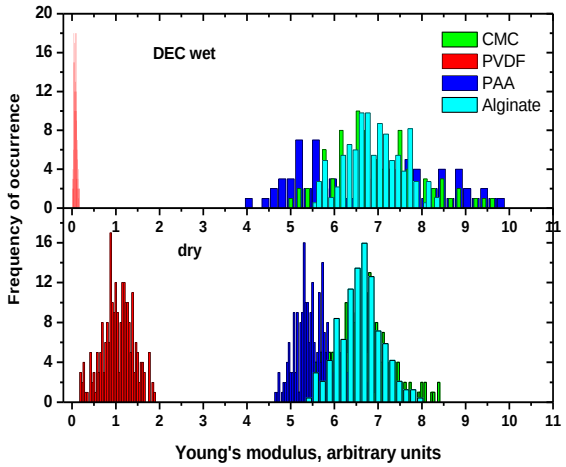

Figure 5.5: Mechanical stiffness measurements of PVDF, CMC, PAA and alginate binders, both dry (bottom) and after wetting with DEC (top)

In Figure 5.6, we see voltage vs. capacity profiles for the first two full cycles of our Si anodes, comparing the performance of the PAA and alginate binders to the Na-CMC and PVDF binders, for both the C-coated Si and the non-coated samples. These samples were cycled to effectively 100% of their theoretical capacity (to 0.01 mV vs. Li/Li+) to test the endurance of the binder under extreme conditions. In all of these samples, we see a relatively flat capacity vs. voltage curve, indicating the absence of major phase changes. This suggests that the transformation from crystalline Si nanoparticles to amorphous Li_xSi is gradual, with no abrupt phase changes. The Li insertion curve for the second and subsequent insertion curves exhibits similarly gradual changes. These effects are characteristic of Si nanoparticles – unlike micron-size powders, Li insertion curves for nano-Si cover a wide range of potentials, reaching 0.2 V or lower potentials after 30% or more of maximum capacity.[94] These results are likely a product of the lack of crystalline phases in the lithiated nano-Si, and will result in a slightly lower terminal voltage in batteries with nanoparticle anodes. All of the investigated anodes exhibit similar insertion and extraction profiles, which are much like those reported in the literature. The

profiles exhibit non-horizontal plateaus, covering a wide range of potentials. The alginate, PAA and CMC samples exhibit better capacity and capacity retention than the PVDF sample. Carbon coating also generally improves these properties – improving the first cycle capacity and increasing capacity retention between the first and second cycles. This suggests that these electrodes possess limited capacities at higher rates, inferior to the nanostructured electrode materials discussed previously. While our intercalation capacity was high, our deintercalation capacity for most of the materials fell well short of the theoretical value of 4200 mAh/g, corresponding to the $Li_{22}Si_5$ phase. The alginate electrode, however, exhibited specific Si capacity of ~3000 mAh/g, close to the maximum theoretical capacity. While it has been suggested by several groups that this theoretical value is impossible to achieve at room temperature, this hypothesis may be inapplicable for nano-Si particles – other possibilities may account for the relatively low capacity.[95, 96] These may include loss of electrical contact upon delithiation, Li^+ ion impedance by the binder, or the presence of the passivating oxide layer.

While the alginate-based anodes exhibit capacity close to the theoretical value, the nano-Si anodes we produced with both PAA (Figure 5.6a,b) and Na-CMC (Figure 5.6c,d) binders exhibit capacity of ~2000 mAh/g, and the PVDF-based anodes exhibit significantly lower capacity. Binder choice also had a dramatic impact on the stability of the first two cycles. The capacity of both the pure Si and C-coated Si anodes with PAA binder increased after the first cycle, suggesting an activation of additional Si nanoparticles which were inaccessible during the first cycle. The volume changes may be responsible, having exposed previously inactive Si to the electrolyte after the initial lithation and delithation. The alginate electrode does not exhibit this behavior, suggesting that all of the active material was accessible, but the degradation in capacity is not signification.

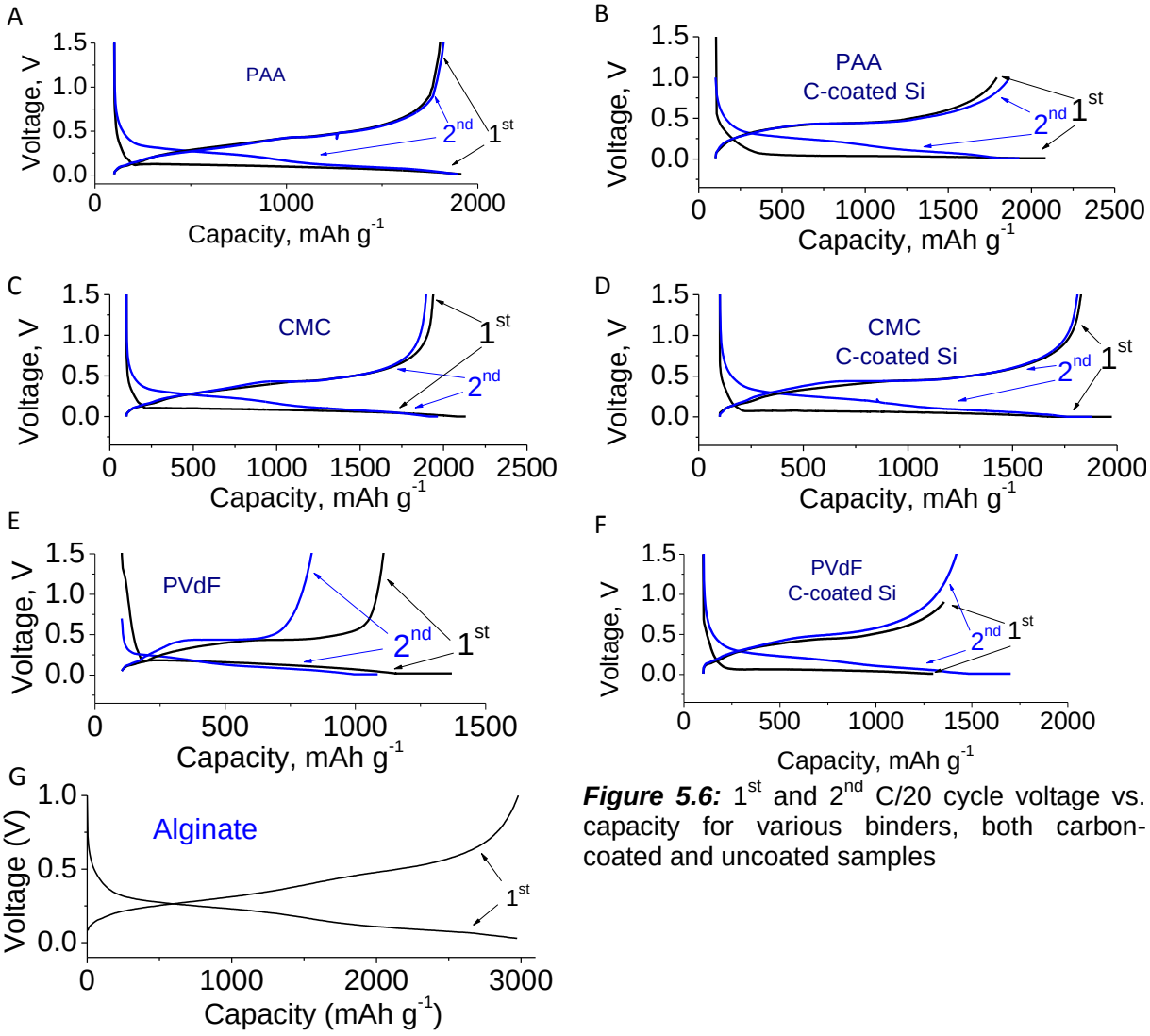

Figure 5.6: 1st and 2nd C/20 cycle voltage vs. capacity for various binders, both carbon-coated and uncoated samples

Comparatively, we saw a significant degration in capacity in the electrodes with a Na-CMC binder, particularly in the electrodes with uncoated nano-Si particles (Figure 5.6c). The Na-CMC binder does, however, exhibit a slightly higher capacity than the PAA binder in the first cycle. We speculate that this is a product of the smaller quantity of carboxylic functional groups in the binder, which results in less coating of the particle, and therefore exposes a larger percentage of

the particle's surface area to the electrolyte. PVDF showed the worst performance, with low capacity and rapid capacity fading. The uncoated Si nanoparticles exhibited the worst performance. The C coating may improve capacity by bridging Si particles directly, providing electrical connectivity for several cycles, even after the binder began to fail under the stress of cycling. Uneven coating of the particles by PVDF may also have had an impact on the electrode's performance, preventing Li ions from accessing a significant fraction of the active particles.

Differential capacity vs. voltage curves for the alginate-based electrode (Figure 5.7) show one broad Li insertion peak at ~0.21 V and two Li extraction peaks at 0.33 and 0.51 V, all of which are often observed in Si anodes.[48] The other binders exhibit similar reaction kinetics. These are similar to those observed in our studies of our granular nanocomposites, suggesting analogous reaction kinetics. The source of the difference in peak position between the insertion and extraction curves is unclear from a review of the literature, but it is generally modeled by the use of a thermodynamic (rate independent) hysteresis. A small Li extraction peak is also visible at ~0.17 V, presumably corresponding to Li deintercalation from the C conductive additives.

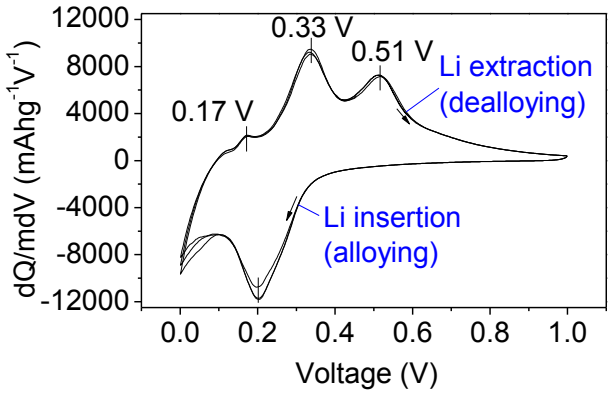

Figure 5.7: Differential capacity vs. voltage graph for uncoated nano-Si electrode with alginate binder

In Figure 5.8, we show the Li insertion and extraction capacities for electrodes based on all 4 different binders charged and discharged at a C/20 rate. Alginate and PAA exhibit superior performance compared to both the state-of-the-art Na-CMC and more conventional PVDF binders. Both the C-coated and uncoated nano-Si anodes showed excellent stability for the first 6-8 cycles (Figure 5.8a). However, as we increase the number of cycles, the Coulombic efficiency drops, leading to rapid degradation in the case of uncoated Si. This suggests a loss of electrical contact, possibly due to the mechanical or interfacial failure of the binder. However, the carbon-coated nano-Si particles with PAA or alginate binder have significantly improved anode stability, resulting in retention of 94% of initial capacity after 20 cycles. In this case, the small fading of capacity may be a result of the degradation of the surface of the Li counter electrode (and resulting increase in impedance). This performance is exceptional compared to other binders whose performance is reported in the literature, especially considering the relatively low binder content (15%) and the full lithiation and delithiation of the electrodes, which produces extreme stresses on the electrode.

Compared to the alginate- and PAA-based electrodes, the Na-CMC and PVDF-based electrodes (Figure 5.8b,c) show dramatically lower performance. These binders show loss of capacity after even the first cycle. While carbon-coated samples have somewhat improved stability, the level of anode degradation is still extreme – 42% and 58% of capacity is lost after 20 cycles in the case of the Na-CMC binder (for uncoated and C-coated Si respectively), and 13% and 16% of capacity is lost after 20 cycles in the case of the Na-CMC binder (for uncoated and C-coated Si respectively). The PAA and Na-CMC-based electrodes exhibit Coulombic efficiency in excess of 90% during the first cycle, despite the small particle size (and its correspondingly high specific surface area). The average Coulombic efficiency over 20 cycles

was highest in the electrode with alginate binder or PAA binder and C-coated Si, at ~97% (Figure 5.8a). More thorough electrode dehumidification could further improve the efficiency.

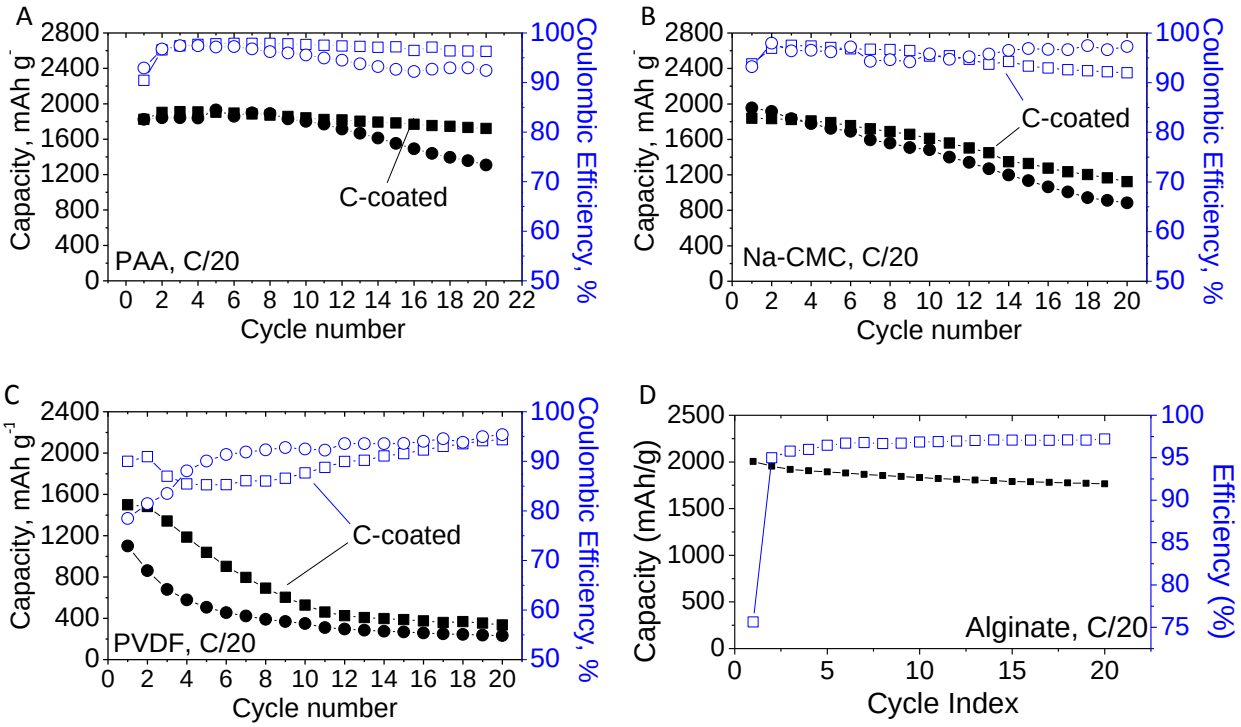

Figure 5.8: Electrochemical performance of nano-Si electrodes with various different binders cycled at C/20; a) PAA, b) Na-CMC, c) PVDF, d) Alginate

When the electrodes are cycled at faster charge/discharge rates, we find the binder used produces a significant difference in performance. We tested each of the binders in electrodes with 15 wt% binder, using active material with a 3:1 Si:C ratio. The carbon in the electrode was a mixture of carbon black and purified exfoliated graphite, rather than a carbon coating. These cells were initially cycled twice at C/20 to improve the quality of the SEI, then cycled at least 100 times at C/1 or C/2. Batteries made with PVDF (Figure 5.9c) exhibited the worst

performance in most respects, with reversible discharge capacity dropping to under 1000 mAh/g almost immediately, and dropping below to less than 700 mAh/g in under 50 cycles. The efficiency for the first C/1 cycle was high, at 90%. The efficiency for subsequent cycles was also relatively high, being 98.6% for the cycles 4-50, and 99.2% for the last 50 cycles. The electrode made with Na-CMC binder (Figure 5.9b) retains its capacity longer, with capacity over 1000 mAh/g for the first 20 C/1 cycles, and retaining capacity over 700 mAh/g for more than 50 cycles. The efficiency for the first C/1 cycles is worse than that of the PVDF-based electrode, however dropping to ~67%. Subsequent cycles perform better, albeit not as well as the PVDF – the Coulombic efficiency is only 97.2% for cycles 4-50. After cycle 50, the average Coulombic efficiency is equivalent to that of the PVDF-based electrode. The electrode made with PAA (Figure 5.9a) performs substantially better – they exhibit reversible discharge capacity over 1000 mAh/g for up to 196 cycles. The first-cycle efficiency is equivalent to that of the PVDF-based electrode, and the average efficiency up to cycle 50 and from cycles 50 to 196 are also equivalent – 98.6% and 99.2% respectively. The alginate-based electrode exhibits the best performance of all. It demonstrates stable reversible discharge capacity over 1000 mAh/g for more than 400 cycles, with minimal capacity fading. The efficiency for the first C/1 cycle is ~94%, better than any of the other binders tested. The efficiency for cycles 4-50 is 98.6%, equivalent to the PVDF-based electrode, and the efficiency of subsequent cycles is substantially superior, at 99.7%. Overall, the alginate exhibits superior performance in every respect.

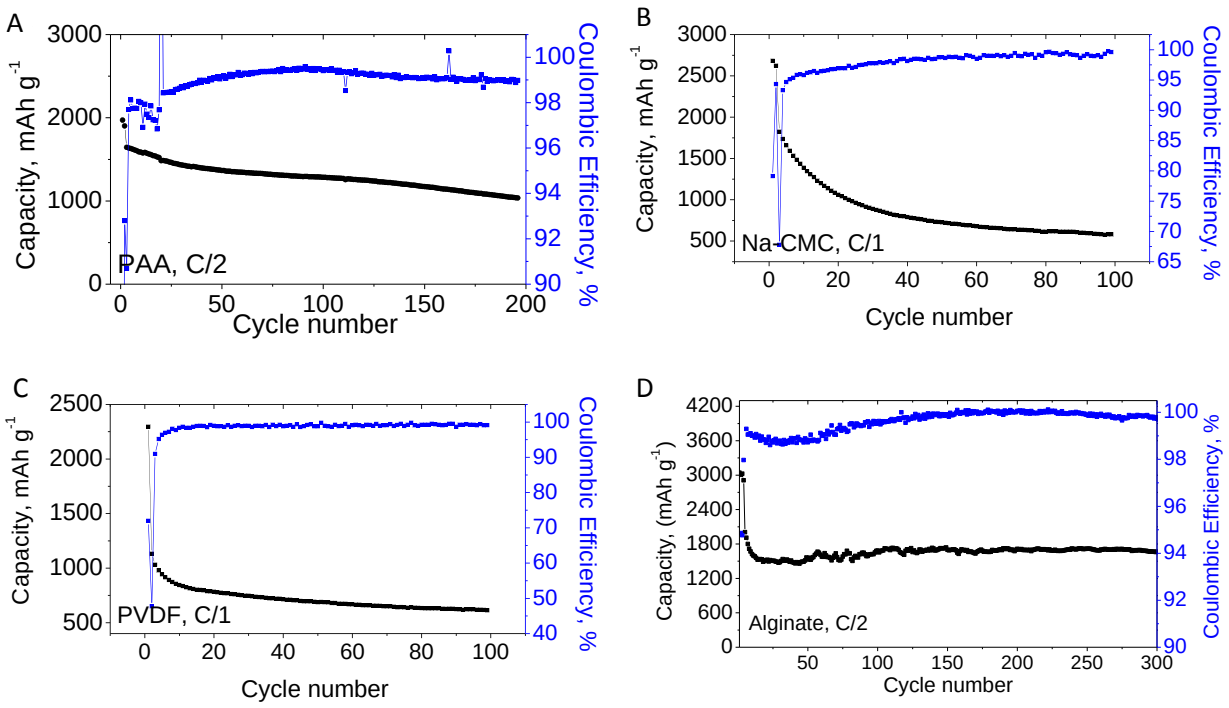

Figure 5.9: Electrochemical performance of nano-Si electrodes with various different binders cycled at C/20; a) PAA, b) Na-CMC, c) PVDF, d) Alginate

Given that the mechanical properties and active functional groups of alginate, PAA and Na-CMC are similar, we can assume that the high concentration of carboxylic functional groups in alginate and PAA are a significant factor in their superior performance. It is our theory that the superior performance of alginate and PAA binders is a product of strong hydrogen bonding between the carboxylic (COOH) groups in the binder and the OH groups on the Si (or C) surface. The unbonded carboxylic groups may further contribute to performance by forming ionically conductive COOLi groups during initial Li insertion, which become part of the SEI, leading to improved solid electrolyte interphase (SEI) quality. This prevents excessive SEI growth, thereby reducing impedance within the electrode and improving anode electrical connectivity. The performance of these binders might be improved by increasing their elasticity. This increase in elasticity could assist battery performance by (a) making the SEI more elastic and deformable

without reducing stability, thereby preventing SEI disintegration caused by extreme volume changes, and by (b) helping maintain binder integrity through multiple cycles, thereby improving the performance of the electrode.

XPS data can give us better insight into the surface properties of our system, including the SEI. For this purpose, we have performed XPS studies on our alginate and PAA electrodes before and after cycling (Figure 5.10) Comparing the C1s high-resolution scan for our alginate samples at the 10^{th} and 200^{th} cycle (Figure 5.10d), we see that the composition of the SEI has not changed significantly as a result of cycling, suggesting that the SEI is highly stable. The PAA electrodes, however, undergo significant changes between the 10^{th} and 100^{th} cycle, exhibiting significantly higher content of molecules with unstable carbonate chemical states after extensive cycling. These states heavily correspond with lithium alkyl carbonates and semicarbonates, which typically dissolve more easily in liquid carbonate electrolytes. With a less stable SEI, these compounds can dissolve easily into the solution, where they become electrochemically inactive. This indicates that the PAA electrode exhibits a overall less stable SEI, which may explain its reduced Coulombic efficiency. The SEI of the PAA electrode also contains a greater initial water content, compared to the alginate electrode. Higher H_2O contents can potentially result from the decomposition of unstable carbonates or from trace quantities of water leftover from insufficient electrode dehumidification. (Figure 5.10b, e) Other differences between the SEI of the two electrodes visible in the high-resolution scans include a overall higher content of lithium hexafluorophosphate ($LiPF_6$) in the SEI of the PAA electrode and a lower LiF content (Figure 5.10c, f). Under normal circumstances, the electrolyte salt is broken down during electrolyte decomposition to form a range of different phosphates. A higher content of $LiPF_6$ in the SEI may indicate incomplete decomposition of electrolyte during cycling, a potential signal

of lower SEI stability. Lower LiF content generally indicates a SEI with less overall LiF, implying lower stability, since LiF is an effective passivating agent. Alternatively, lower LiF content may indicate a thicker SEI, which could conceal the presence of LiF, since LiF tends to form at the interface between the SEI and the electrode, rather than in the porous outer layer of the SEI. [59] A thicker SEI will typically increase electrode impedance and polarization resistance, potentially reducing Coulombic efficiency. These differences hint at some of the potential factors accounting for the differences between the performance of PAA and alginate. There are similar correlations between SEI stability and improved Coulombic efficiency in CMC binders found in the literature; however, significant improvements in efficiency require relative binder quantities several times higher than those used in our PAA and alginate electrodes. These results are summarized in Figure 5.10.

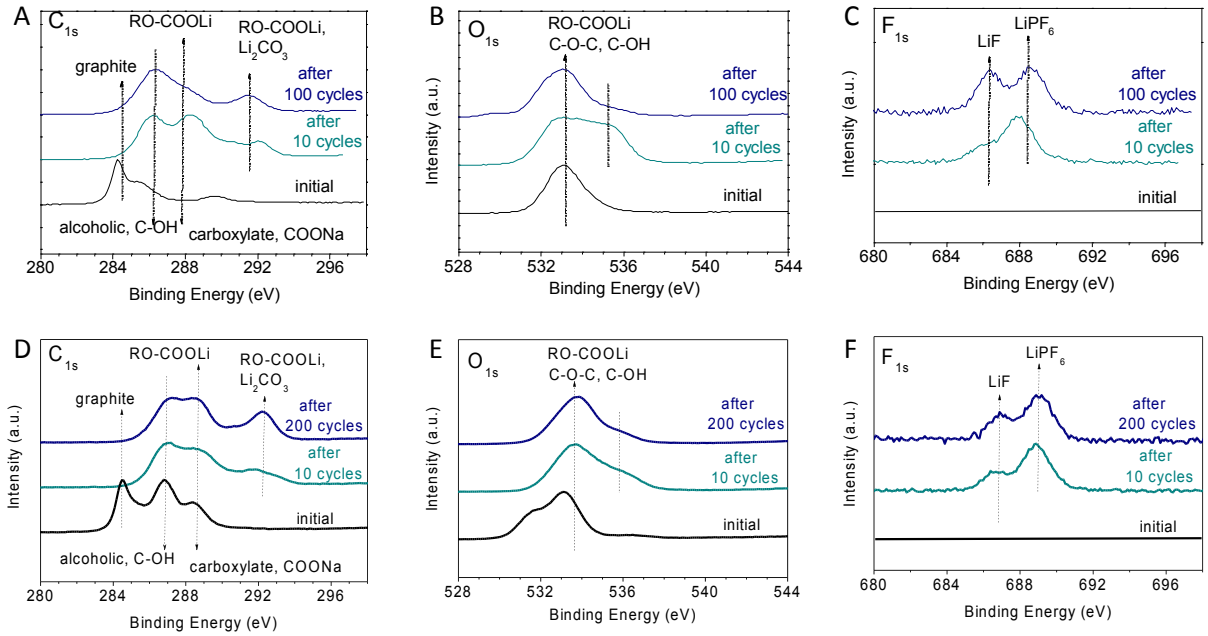

Figure 5.10: XPS spectra for PAA C1s (a), O1s (b), and F1s (c) initially, after 10 cycles and after 100 cycles, as well as alginate C1s (d), O1s (e), and F1s (f) initially, after 10 cycles and after 200 cycles

Conclusion

In conclusion, we have demonstrated for the first time that alginate and PAA may serve as effective binders for Si-based Li-ion battery anodes. These materials exhibit many of the beneficial properties of Na-CMC, such as a high elastic modulus and low interaction with and absorption of carbonates. These materials exhibit a higher concentration of carboxylic functional groups, which we believe may favorably affect their performance. Carbon coatings on the surface of Si nanoparticles produce significant improvements in anode stability for all three of the binders studied. Coulombic efficiency for the PAA batteries demonstrated high Coulombic efficiency, in the range of 97-98% after the first cycle, with capacity degradation of less than 0.3% per cycle. Coulombic efficiency for the alginate batteries was even higher, ~99% per cycle, with equivalent capacity retention. With further improvements in binder properties, we may be able to demonstrate better capacity retention as well as improved SEI stability and Coulombic efficiency.

5.3 Impact of Surface Stresses on SEI Performance

Approach

The quality of the solid-electrolyte interphase (SEI) has a strong impact on the performance of a lithium-ion battery. Much of the early research done on Li-ion batteries was focused on producing electrolytes which would produce a stable SEI during cycling. When E. Peled first theorized the existence of the SEI, he hypothesized that the thickness of the SEI would be limited by the electron tunneling range, but that this thickness could be increased by cracks, holes or grain boundaries at which an increased degree of electronic leakage could occur.[54] In the most current models of the structure of the SEI, the SEI is considered to be

composed of two layers: a dense inner layer comprised primarily of inorganic species produced primarily by salt reduction (such as Li_2CO_3 and LiF) and an porous outer layer comprised of organic, possibly polymeric species, including a range of lithium alkyl carbonates and semicarbonates. The defects which may permit the undesirable, unrestricted growth of the SEI can be common in either of these layers.[55, 56] When the growth of SEI is not limited, the performance of the battery is significantly impacted. When the SEI is chemically or structurally unstable, the electrolyte will be decomposed continuously, cycle after cycle, reducing the efficiency of the cell significantly.[52] Furthermore, if the SEI thickness increases too greatly, the ionic impedance of the electrode will increase dramatically. As previously described, a study led by D. Guyomard showed that the contribution of the SEI resistance to electrode polarization due to increases in interphase thickness during cycling was the primary factor in capacity loss in nano-Si based electrodes, rather than any losses of electronic contact caused by binder failure.[58] Silicon-based electrodes are particularly susceptible to unrestricted SEI growth, as stresses produced by the expansion of the silicon active material can result in dramatic increases in SEI defect population. Si-based electrodes require more flexible SEIs than graphitic electrodes, which experience little mechanical stress but are potentially vulnerable to exfoliation caused by the intercalation of solvent between SEI layers.[97] High tensile stresses caused by lithium deintercalation have been found to cause the progressive propagation of cracks in cylindrical graphitic active particles. As these cracks propagate, the thickness of the SEI increases, as the greater size of the defect permits easier electron conduction, facilitating the passivation of the electrode.[98] In silicon, the stresses placed on the surface of the electrode by alloying and dealloying will also have an effect on the defect population of the SEI. However, the impact of these stresses is poorly understood – the effect of different degrees of stress on the

quality of the SEI has not been investigated to date. Certain stress levels may have different impacts on the electrode passivation and the integrity of the SEI. In order to better understand the impact of internal stresses on the composition of the SEI, we have opted to analyze the SEI of carbon-coated spherical nano-silicon samples. By varying the thickness of the carbon coating, we can control the stresses on its outer surface produced by lithiation. Thicker carbon shells will produce lower degrees of surface stress, since the overall diameter of the composite nanoparticle will change less. By analyzing the composition of the SEI and the sample's polarization resistance, we can investigate the effect of stress on the performance of these particles.

Experimental Methods

The primary active material of our electrodes was Si nanopowder (NP-Si-L50, 98 % purity, MTI Corporation, USA). In most of the electrodes, these nano-Si samples were then coated with carbon. This process was implemented by chemical vapor deposition at atmospheric pressure and a temperature of 700 C, using propylene as a precursor gas. The surface area, pore size and particle size data of the coated and uncoated particles were determined by analyzing nitrogen adsorption and desorption isotherms collected at 77 K using relative pressures of 0.0002-0.99 P/P_0, via a TriStar II 3020 (V1.03) surface area and porosity measurement system (Micromeritics Inc. , USA), effective for measurements of specific surface area (SSA) and pore size distribution (PSD) in the range of 2-100 nm. These analyses were performed on 50-100 mg of each powder, which was prepared by drying the powder under a vacuum at 80^O C for at least 12 h, followed by degassing under a N_2 gas flow at 300^O C for at least 2 h prior to weighing and gas sorption measurements. SSA and PSD were calculated using the Brunauer-Emmett-Teller and Barrett-Joyner-Halenda methods, respectively. Micromeritics DataMaster software was

used to perform the calculations. Isotherm measurements in the relative pressure range of P/P_0 from 0.05 to 0.3 was used for multi-point BET calculations. The size of the coated and uncoated particles was determined using the BET specific surface area. The average particle size of the uncoated particles was determined to be ~25 nm. Three different thickness of carbon were used, producing three different samples – one with a 11 nm C coating (total Si content 60%), one with a 16 nm C coating (total Si content 46%), and one with a 24 nm C coating. Annealed carbon black was also used, as a control sample. This material was coated with additional carbon using the same CVD process as the nano-Si samples to ensure matching surface chemistry.

We used PAA (Sigma-Aldrich, USA) with molecular weight of 450000 g/mol dissolved in a ethanol-H_2O mixture as a binder. All of the electrodes (other than those based on sodium alginate) contained 15 wt. % of binder and 85 wt% of active material – either uncoated nano-Si, nano-Si with a C coating ranging from 11 to 24 nm in thickness, or annealed carbon black with a CVD-produced carbon coating. No additional conductive additives were used. The electrode slurries were mixed at 600 rpm using a laboratory stirrer, after an ultrasonic bath was used to ensure effective nanoparticle dispersion. After mixing, the slurries were cast onto an 18 μm Cu foil (Fukuda, Japan) in a 75 μm thick layer. Subsequently, the cast electrodes went through a multi-stage drying process: first being dried in air at room temperature, followed by drying at 60^{O} C for at least 4 hours. Subsequently, they were degassed in vacuum at 70^{O} C for 2 hours inside an Ar-filled glove box with <1 ppm of oxygen and water (Innovative Technology, Inc., USA), avoiding exposure to air prior to cell assembly.

We used a commercial electrolyte, composed of 1M $LiPF_6$ salt in a mixture of ethylene carbonate – diethyl carbonate – dimethyl carbonate (EC:DEC:DMC = 1:1:1 vol. %) (Novolyte Technologies, USA). The counter electrode used was lithium metal foil (1 mm thick, Alfa Aesar,

USA). We used 2016 stainless steel coin cells for electrochemical measurements. We spotwelded the Cu foil current collector to the coin cell to improve the electrical contact. We calculated charge and discharge rates assuming a theoretical capacity of 4200 mAh/g for the Si and an experimentally determined capacity of 320 mAh/g for the CVD-produced C and 150 mAh/g for the carbon black, determining the capacity of the electrode based on the ratio of Si to C in it. We cycled the cell between 0.01 and 1.99 V vs. Li/Li^+. We calculated Coulombic efficiency as $100\% \cdot (\frac{C^{dealloy}}{C^{alloy}})$, where C^{alloy} and $C^{dealloy}$ are the capacity of the anodes for Li insertion and extraction. We used Arbin SB2000 (Arbin Instruments, USA) and Solartron 1480 (Solartron Analytical, USA) multi-channel potentiostats for electrochemical measurements. A Solartron 1287A single-channel potentiostat, combined with a 1255B Frequency Response Analyzer, was used for Electrochemical Impedance Spectroscopy (EIS) studies. The cells studied via EIS were initially subjected to 2 C/20 cycles to promote the development of a stable SEI, and were then tested via EIS between frequences of 65 kHz and .01 Hz, at an AC bias of 0.01 V. Testing occurred for each cell at 2, 10, 30, 50, 100 and 200 cycles. The circuit model used to analyze the impedance data is shown at right, in Figure 5.11. This model incorporates resistor, constant phase elements, and Warburg resistance elements, representating cell or polarization impedance, electrical double layer impedance, or diffusion-related impedance respectively. \

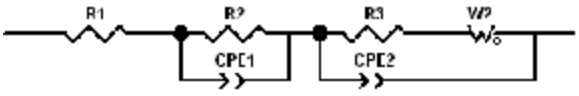

Figure 5.11: Equivalent circuit model used to interpret EIS data gathered from tested cells

X-ray photoelectron spectroscoply (XPS) characterization was performed using a Thermo K-Alpha XPS system (Thermo Scientific, USA) equipped with an Al Kα radiation as a source, with

an energy resolution of 1 eV for the survey scans and 0.1 eV for high-resolution scans of individual characteristic peaks. The X-ray gun produced a 400 μm spot size, and an electron flood gun was used to minimize charging. The system vacuum level was below 10-8 Torr during the data collection. An emission angle of 90o was used. After being cycled, the cells were disassembled in a glove box and the electrodes were removed and stored in DMC to avoid exposure to oxygen. While the samples were being loaded into the machine, additional DMC was poured on top of the sample to prevent oxidation before the test. High resolution TEM observations were carried out using on a Titan S/TEM microscope (FEI, Netherlands), equipped with a SuperTwin objective lens with a Cs of 1.2 mm. This microscope has a point resolution of 0.245 nm and an information limit of 0.08 nm. It operates at 200 kV.

Results

In order to be assured that the structural integrity of the carbon coating remains unaffected by the high stresses produced by lithiation and delithiation, we have characterized our samples via TEM before and after cycling. The sample being studied is the 60% Si (11 nm C coating) C-coated nano-Si electrode, before being converted into an electrode and cycled, and after 50 C/2 cycles. The results are shown below, in Figure 5.12. Here, we see that the C coating thickness is approximately equivalent to what our BET measurements predicted for this sample, at ~11 nm thick. The coating thickness appears fairly uniform over most of the sample, and there are no visible cracks in the C coating. After cycling, the dimensions of the particle and the thickness of the carbon coating do not appear to have changed significantly. There still are no large visible cracks or evidence of delamination in the carbon coating, indicating that the CVD-produced C layer was well-adhered and able to survive the extreme volume changes produced by

Li-ion insertion and extraction. Any cracks which may have been produced during Si expansion appear to have healed during the contraction of the Si-Li alloy core of the nanoparticle.

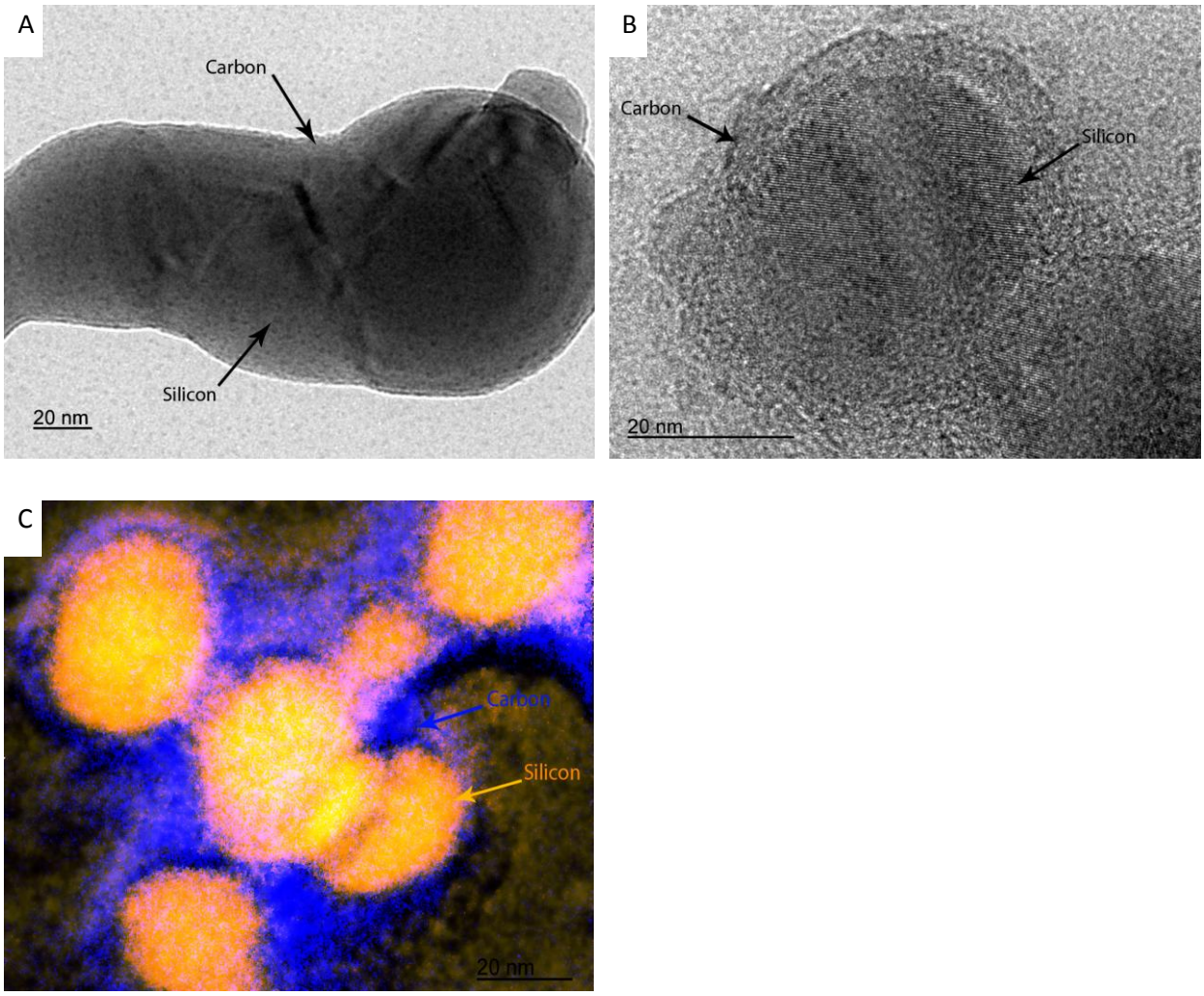

Figure 5.12: Transmission electron micrographs of 60% Si C-coated nano-Si, a) before cycling, b) after 50 C/2 cycles, and c) a spectrographic map of C and Si in (b)

Electrochemical performance data, acquired as previously described, is shown below in Figure 5.13 for the samples cycled at C/2 for 200 cycles before disassembly. Each of these cells was cycled initially twice at C/20 to promote stable SEI development. From this data, we see that

the nano-Si electrode exhibits rapid fading, dropping to a capacity that is only a small fraction of theoretical levels within less than 50 cycles. The Coulombic efficiency of the nano-Si based electrode is highly unstable, spiking up as the cell loses capacity (up to 50 cycles), and then dropping once the capacity stabilizes at a low level. All of the C-coated nano-Si samples exhibit roughly similar behavior: initially stable capacity for ~30-50 cycles, followed by a spike or plateau in capacity, followed by a slow decline in capacity. The 60% Si nanocomposite (11 nm C coating) exhibits the highest capacity, while the 46% Si (15.7 nm coating) and 32% Si (24 nm coating) samples have roughly even capacity. The 60% Si sample exhibits the fastest capacity fading, while the other two samples exhibit roughly the same degree of fading. This unusual behavior may be a product of either SEI or binder failure effects, but it is consistent across all of our samples. All three of the C-coated nano-Si electrodes exhibit similar Coulombic efficiency as well – initially stable efficiency, with a drop in efficiency corresponding to the electrode's spike in capacity, followed by a slow recovery to initial levels of efficiency. The carbon black electrode (0% Si) exhibits low, but constant capacity and excellent, constant efficiency. This is typical of any electrode based on carbonaceous materials.

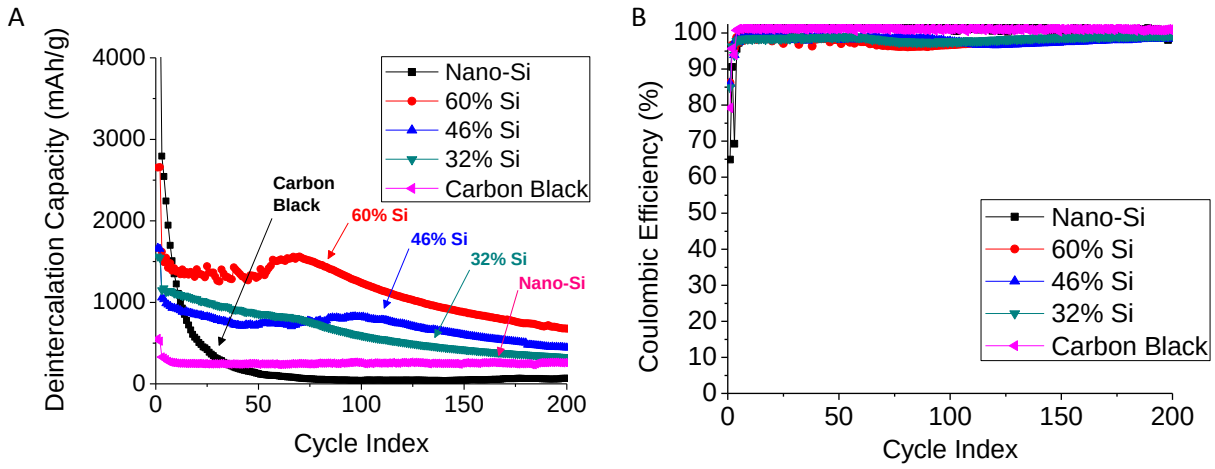

Figure 5.13: Electrochemical performance of C-coated nano-Si electrodes and control samples; a) reversible lithium deintercalation capacity of samples, b) Coulombic efficiency of samples

The chemical stability of the SEI may be impacted by the ratio of stable carbonates (such as Li_2CO_3) to less stable carbonates or semicarbonates (such as lithium alkyl carbonate). The ratio of the integrated energies of these peaks, derived from high-resolution XPS scans, is shown below, in Figure 5.14.

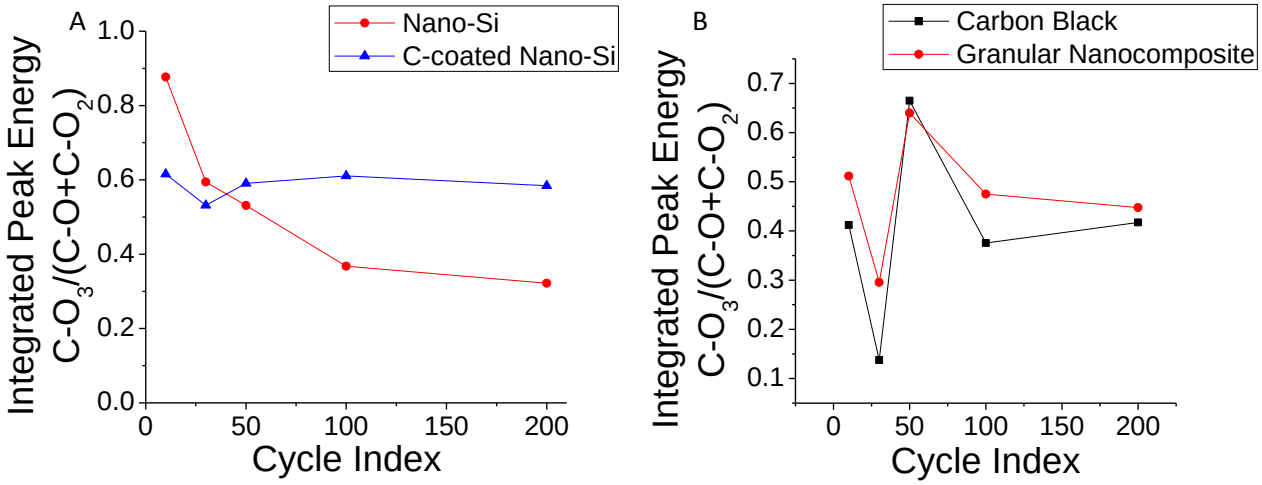

Figure 5.14: Ratio of integrated peak energy for $C\text{-}O_3$ to sum of C-O and $C\text{-}O_2$ peaks for several different samples, gathered via high-resolution XPS scans

Several patterns are immediately apparent from this graph. Comparing the organic composition of the nano-Si electrode to that of the average of the C-coated nano-Si electrodes in Figure 5.14a, we see that the nano-Si electrode experiences a rapid decline in $C\text{-}O_3$ peak content with increasing cycling, eventually leveling out. This is to be expected, since without the stress-reducing effects of the carbon coating, the expansion produced by lithiation will prevent the development of a chemically stable SEI. The carbon-coated nano-Si samples undergo small changes with cycling, but none of them suffer the massive drop in chemical stability we see in the uncoated nano-Si sample. They possess high long-range chemical stability, by comparison to

the uncoated nano-Si electrode. The final integrated peak energy ratio (at the 200th cycle) is high, and roughly the same as the integrated peak energy ratio at 10 cycles. While there are differences between the 3 C-coated nano-Si samples, the thickness of the carbon coating appears to have only a limited effect on this parameter. In Figure 5.14b, we compare our pure carbon control sample and the granular nanocomposite we described in Section 4.3. The pure carbon sample experiences dramatic initial changes, but the electrode SEI does not change composition significantly between 100 and 200 cycles, and the final integrated peak intensity ratio of the SEI is high. The granular nanocomposite behaves similarly to the pure carbon sample – this is to be expected, since both electrodes are composed partially of carbon black, and neither type of electrode particle experiences a net change in volume during lithium insertion. Since both electrodes experience minimal surface stresses, the composition of their SEI changes in extremely similar ways.

While measuring the thickness of the SEI in-situ is difficult, due to its multi-layer nature and the changes occurring in it at various stages during the lithium insertion and deinsertion process, it is possible to analyze the evolution of its thickness by studies changes in the SEI's LiF content. Lithium fluoride is generally found only in the innermost layer of the SEI, which is relatively dense and inorganic, compared to the porous, organic outer layer of the SEI. As the thickness of the porous, organic outer layer changes, the apparent LiF content of the SEI detected by the XPS will change, since XPS is an extremely surface-sensitive technique. The normalized atomic % of LiF detected in the SEI is shown in Figure 5.15 below.

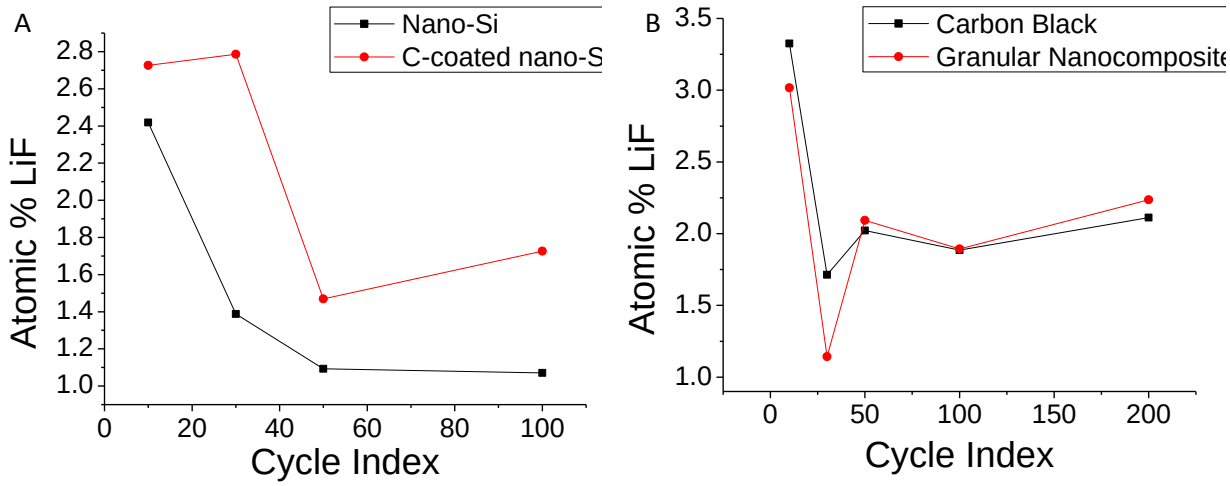

Figure 5.15: Ratio of atomic % LiF for several different samples, gathered via high-resolution XPS scans, offset for ease of study

From Figure 5.15a, we can see that the LiF content of the SEI decreases dramatically in the uncoated nano-Si samples over its 100 cycle lifetime, indicating a substantial increase in SEI thickness. This indicates a failure in electrode passivation by the SEI, presumably due to the high surface stresses in the SEI produced by expansion of the Si nanoparticle. The C-coated nano-Si electrode samples experience a slower and less dramatic reduction in LiF content, indicating a somewhat more mechanically stable SEI. The final LiF content of the SEI in the coated samples at 200 cycles, although not as high as it was initially, is still more than half of the initial content at 10 cycles. In the coated samples, the final content of LiF in the SEI is lowest in the 60% Si C-coated nano-Si sample, indicating a thick SEI. This suggests that the carbon coating is not yet thick enough to buffer the stresses of Li expansion and ensure mechanical stability for the SEI, resulting in the unrestricted growth of the SEI. The other C-coated nano-Si electrodes, however, experience minimal changes in their LiF content over their lifetime, indicating a mechanically stable SEI. This suggests that a carbon coating with a thickness of at least 15.7 nm is enough to buffer the stresses of expansion for our nano-Si samples, preventing defect formation in the SEI

and enabling it to efficiently passivate the electrode. The pure carbon and granular nanocomposite samples, shown in Figure 5.15b, behave similarly to the C-coated nano-Si samples with thicker coatings. This is to be expected, since they experience no net volume changes, and therefore should have SEIs with stable thicknesses.

Additional information regarding the condition of the electrode SEI can be derived from impedance spectroscopy data. The electrode's impedance to the transfer of Li^+ ions into the active material is one of the major contributors to its polarization resistance, and an excessively thick SEI is a major contributor to ion transfer impedance. By analyzing the impedance of the SEI using EIS as a function of electrode mass (and therefore thickness, since electrode density is similar between all of the samples), we can estimate the contribution of the SEI to impedance for each of the samples over a number of cycles. Each of the samples was tested under conditions identical to those previously described. An example of our EIS data, taken from the 32% Si sample at 50 cycles, is shown in Figure 5.16a.The polarization resistance values determined using EIS data and this model are shown in Figure 5.16b.

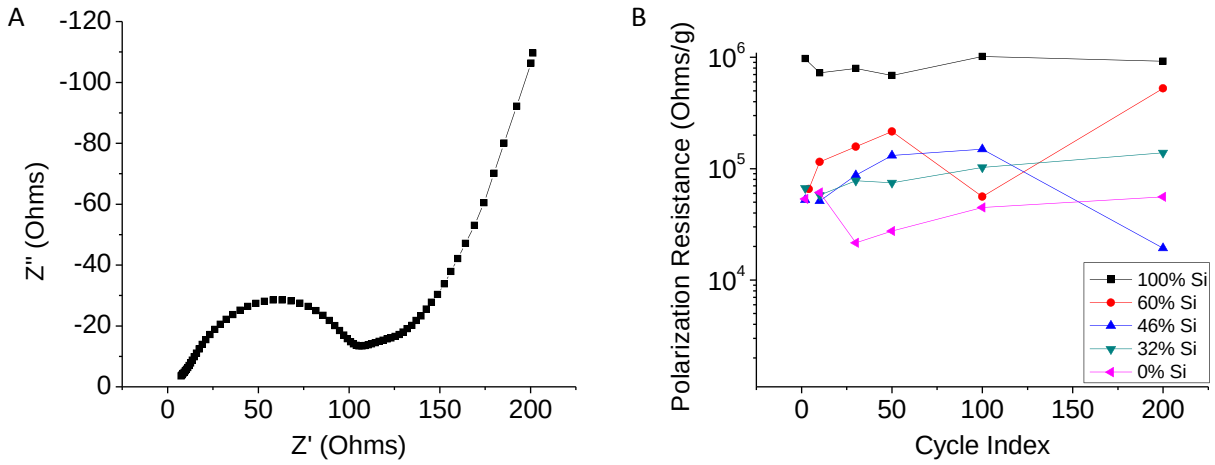

Figure 5.16: Electrochemical impedance data from C-coated nano-Si cells. a) EIS data from 32% Si (24 nm C coating) C-coated nano-Si electrode at 50 cycles; b) Specific polarization resistance of electrodes as a function of cycle

From the specific polarization resistance of our electrodes in Figure 5.16b, we can find several trends. First, the specific polarization resistance of the uncoated nano-Si electrode is dramatically higher – by approximately an order of magnitude - than that of the other electrodes. This increase in resistance is presumably due to the thicker SEI of the uncoated nano-Si electrode and the degradation of the binder, producing a loss of electrical contact. The carbon black electrode, meanwhile, possesses lower polarization resistivity than any of the other electrodes at any cycle other than the 200th, where the 46% Si electrode appears to possess lower resistance. The coated samples, however, exhibit significant differences in their properties. Electrodes with higher %Si tend to possess higher polarization resistance at any given cycle, though there are exceptions – all of the C-coated nano-Si electrodes have roughly the same polarization resistance at 2 cycles. From the 2nd to the 50th cycle, the resistance curves of the 60% Si and 46% Si electrode have similar shapes, with specific resistance increasing steadily from cycle to cycle. Meanwhile, the 32% Si electrode exhibits similar behavior to the C-coated carbon black electrode, although its resistance is somewhat higher.

Conclusion

Examining our data, we can draw several important conclusions. The chemical stability and conductivity of the SEI of a nano-Si active material is improved dramatically by the addition of a carbon coating of even modest thickness. However, if the coating is not thick enough, the stresses of Li insertion and deinsertion will still produce defects in the SEI, enabling electron tunneling and promoting further growth in the SEI during cycling, and ultimately limiting the electrochemical performance of the SEI. In the case of our nano-Si samples, we find that the coating must be of at least ~15 nm thickness to maintain mechanical stability in the SEI.

Although the high stresses produced by lithium insertion and deinsertion will still tend to produce an SEI with a high defect population, the SEI thickness will be kept relatively low by its limited electronic conductivity. If the C coating is too thin, even the stable inner layer of the SEI will be affected by the high stresses. It is therefore possible to find a certain optimal C coating thickness and concomitant level of surface stress, which will minimize the thickness of the porous outer layer of the SEI without reducing the specific capacity of the electrode excessively. With more intensive investigation, we may be able to find this optimal level, thereby further enabling the intelligent design of carbon-silicon composite electrode materials.

6. Structural and Mechanical Properties of Nanocomposite Anodes

6.1 Overview

Rational design of Si-C nanocomposites can be assisted by a more comprehensive understanding of the internal structural and mechanical changes occurring within them during lithiation and delithiation. With more sophisticated models, we can improve the design of electrode materials with less extensive experimentation, by applying information gathered from both models and empirical studies to a range of different nanocomposites. In order to perform useful simulations, we must have a better understanding of the mechanical properties produced by lithiation of silicon, which we have gathered through ex-situ nanoindentation of silicon thin films at a range of different Li-Si compositions. We have applied this information to lattice-based spring and finite elements models which simulate both the plastic deformation of lithiated thin films and the evolution of strain throughout Si-C core-shell nanoparticles. These models give us a better understanding of the mechanical and structural changes occurring within nanocomposite materials during lithium insertion.

6.2 Ex-Situ Nanoindentation of Lithiated Silicon

Introduction

The primary challenge to the commercialization of Si anodes for Li-ion batteries is the difficulty of maintaining the integrity of both the Si electrodes and the solid-electrolyte interphase (SEI) on Si. This problem is caused by the dramatic expansion of the material during battery operation. A number of investigators have examined the lithiation behavior and phases present in silicon films and powders of a variety of thicknesses and particle sizes. [52, 86, 99-107] They found that the morphology and dimensions of the anode material had a significant effect on the phases forming during lithiation and the voltages at which these phases formed.

Among the important observations was the amorphization process occurring during the initial lithiation stages, when silicon particles and thin films would transform into an amorphous phase. Interestingly, particles and films of sufficiently large size would partially crystallize into the $Li_{15}Si_4$ phase when the material was sufficiently lithiated, while particles and films below this critical size would remain amorphous throughout the entire lithiation process, and could be lithiated to $Li_{22}Si_5$. Another important observation was the room-temperature deformation in Si during reversible electrochemical alloying with Li.[108] In that study the lithiated Si particles were found to mechanically deform and adopt to the shape of the rigid carbon outer shell. When stable Si nanoparticle anodes are produced with rigid binders, one may expect that a similar type of deformation may take place during the expansion of the particles into the differently shaped electrode pores.[86, 109, 110] The endurance of the Si-binder or Si-C interfaces, critical for stable anode operation, must exceed the amplitude of the interfacial stresses caused by the initial expansion of Si particles, which are, in turn, dependent on the plasticity and elastic modulus of the lithiated Si particles. Note that the mechanical properties of Si and Li differ quite dramatically – while pure Si is a brittle ceramic, pure Li is a soft metal with very low hardness and small elastic modulus. Therefore, simple predictions about the mechanical properties of Si-Li alloys are not easy to make. Unfortunately, little experimental data is available on the mechanical properties of Si lithiated to various degrees. Such information is, however, crucial for the design and successful implementation of stable Si-based anodes.

Density functional theory (DFT) has been recently used to characterize the mechanical properties of lithiated silicon.[111] Shenoy et al. calculated the modulus and Poisson ratios of both amorphous and crystalline Li-Si phases at a range of different concentrations.[111] The study found that the Young's modulus calculated for amorphous and crystalline Li-Si alloys

decrease with increasing Li fraction from 0 to 100%. The only exception is the $Li_{15}Si_4$ crystalline phase, which shows significantly lower modulus than both $Li_{13}Si_4$ and $Li_{22}Si_5$ crystalline phases. Interestingly, for Li fraction changes from 0.5 to 0.76 (LiSi to $Li_{13}Si_4$) the Young's modulus was found to exhibit minimal changes (remained at around ~40 GPa for amorphous alloys and ~90 GPa for crystalline alloys).[111] This observation was explained by the replacement of covalent Si–Si bonds with ionic Li–Si bonds with increasing Li fraction. The charge states of Si, however, varied in the produced alloys quite substantially (from -1 to -4), depending on the Si atomic position and number of Si and Li neighbors, which affected elastic properties of the phases.

Two research groups have recently attempted to experimentally characterize changes in Si properties during electrochemical reaction with Li.[106, 112] Using electrochemical strain microscopy, a new characterization method, Kalinin et al. were able to directly map the lithiation/delithiation process with a nm-level resolution.[106] By detecting contrasts in surface strains with a SPM tip, the investigators were able to determine that Li-ions initially saturated low-density areas in the Si anode during lithiation. In the initial charging process, the grain boundaries rapidly became heavily lithiated; subsequently, the lithiated areas expanded inward into the higher-density areas as the anode approached full lithiation.[106] Sethuraman et al. proposed a very interesting method to perform *in-situ* measurements of the stress in thin Si-Li alloy film during lithiation and delithiation by monitoring changes in the curvature of substrate using a multi-beam optical sensor.[112] Strain in the film was calculated by assuming that the film thickness would vary linearly with the state of charge, thereby determining the corresponding volumetric changes. The biaxial modulus was then determined using the Stoney equation. While the authors concluded that the biaxial modulus could be approximated by the rule of mixtures, they observed rather small changes in the modulus when Li fraction changes in

the range from 0.3 to 0.75. Interesting, a broad peak in modulus was observed at Li fraction of ~0.6 (the modulus of the alloys having Li fraction of 0.3 and 0.75 was lower than for alloys having Li fraction in between these values).[112]

In this study, we employed depth-sensing indentation (nanoindentation) measurements to acquire direct *ex-situ* experimental values of the Young's modulus and hardness of nanocrystalline Si films at various stages of lithiation. The obtained results suggest some deviation in the Young's modulus from the predictions of a simple rule of mixing, which agrees with the actual data collected in prior theoretical and experimental studies, but disagrees with the simplified conclusions of their authors. In contrast, the hardness values of Si-Li alloy seem to exhibit a linear decrease with increasing the fraction of the inserted Li.[111, 112]

Experimental Methods

In order to avoid substrate effects in our nanoindentation measurements, thick (~ 6 μm) Si foil was used in our experiments. Due to the relatively high thickness requirement, Si film was deposited using chemical vapor deposition (CVD) at a relatively high temperature of 750 ^{o}C. Silane (SiH4) diluted in Ar (5 wt. %) was selected as a precursor gas. The deposition was performed at a low-pressure (~ 10 Torr) to achieve high coating uniformity.[104, 113] Amount of the deposited Si was determined using a high precision (0.01 mg) analytical balance. Carbon-coated nickel foils (~ 120 μm) were used as substrates for Si deposition and as current collectors for electrochemical measurements. The C deposition on Ni was employed in order to avoid a chemical reaction between Ni and Si and the formation of Si-Ni alloys at the elevated temperature (750 ^{o}C), at which Si deposition took place. The Ni foil samples were first cleaned

with ethanol and then coated with a thin (~10 nm) layer of C deposited by decomposing propylene (C3H6) at atmospheric pressure and 700 ^{o}C.

A Panalytical X'Pert PRO Alpha-1 diffraction system (Pananalytical, Netherlands) equipped with the incident beam monochromator was used for X-Ray Diffraction (XRD) studies. These studies used only the Kα1 component of Cu radiation in order to improve the overall quality of the collected powder diffraction data. An accelerating voltage of 45 kV, current of 40 mA, 2θ-step of 0.03 and a hold time of 80 sec was selected. X'Pert HighScore Plus software (Pananalytical, Netherlands) was used for spectral analysis. Scanning electron microscopy (SEM) measurements were performed using Leo 1530 microscope (LEO, Osaka, Japan, now Nano Technology Systems Division of Carl Zeiss SMT, USA) operated at a 10 kV accelerating voltage and a 5 – 7 mm working distance.

For electrochemical Li insertion experiments, Si film - coated Ni foil electrodes were cut and assembled into 2016 lithium-ion coin cells inside an Ar filled glovebox (<1 ppm of oxygen and H2O, Innovation Technology, USA). To maintain good electrical contact, Ni foil was spot-welded into the cell. Before cell assembling, the Si-coated Ni foil samples were dried in vacuum for 24 hours at 100 ^{o}C. A Celgard 2325 membrane (Celgard, USA) was used as a separator, and 1M lithium hexafluorophosphate ($LiPF_6$) salt, dissolved in ethylene, dimethyl, and diethyl carbonate (1:1:1 wt. % solution), was used as an electrolyte (Novolyte Technologies, USA). Li foil (electrochemical grade, Alfa Aesar, USA) of 1 mm in thickness was used as a counter electrode.

Li insertions into Si films were performed in a series of two steps, using a Solartron Model 1480A potentiostat. First, a constant current was applied at a slow C/40 rate (full lithium insertion in 40 hours). After this step, the sample was allowed to stay at an open circuit potential

for at least four hours. This was followed by the constant potential step, at which a potential was applied to the cell until the current dropped to 1-5% of the C/40 current applied during the constant current step. The potential was determined by the composition of Li-Si which we aimed to achieve. For Li-Si alloys with high fraction of Li (> 0.3), the constant current / constant potential cycles were repeated multiple times in order to achieve uniform distribution of Li of the desired concentration.

To prepare samples for mechanical measurements, the lithiated Si-on Ni electrodes were removed from the coin cell in an argon dry box and mounted on a straight stainless steel razor blade substrate using a CrystalBond thermoplastic polymer adhesive (70 ºC melting point, Ted Pella Inc, USA). Great care was taken in order to avoid a reaction of lithiated Si with air or moisture during the time between cell disassembly and depth-sensing indentation measurements inside a nanoindenter chamber filled with Ar. After mounting on a rigid stainless steel substrate, the samples were dipped into an anhydrous dimethyl carbonate (DMC) filled vial, placed inside a double-walled Ar-filled container and sealed. Before indentation, ultra high purity Ar (99.9999 %, Air Gas, USA) was purging the sealed indentation chamber at 0.5 scfm for 15 minutes and continued for the duration of the experiments. During the short (~10 s) transfer of the samples from the container to the Ar-filled nanoindenter chamber, the samples were coated with a ~ 1 mm layer of DMC, which evaporated in the chamber in about 30 min during a continuous Ar purge.

Depth-sensing indentation measurements were performed on a Hysitron TI 900 TriboIndenter (Hysitron, USA). A diamond cube corner tip (Northstar radius <40 nm) was used for the measurements. Calibration was performed using a polycarbonate standard with elastic modulus 3.1 GPa and a hardness of 200 MPa, and a 6 coefficient fitting curve. Indentations were

done using max loads of 6000-8500 µN. The loading and unloading rates ranged from 300 to 350 µN/s and were the same for loading and unloading. 16 indentations were made in each sample using the same experimental parameters and spaced 10 um apart.

Reduced modulus values were calculated from the unloading curve using the methods developed by Oliver and Pharr.[114] Elastic contact theory predicts a relationship between the

$$E_r = \frac{S}{2\beta}\sqrt{\frac{\pi}{A_p(h_c)}}$$

modulus and stiffness due to an indentation as follows:

where S is the stiffness and the slope at the point of unloading, E_r is the reduced modulus and A_p is the projected area of contact determined by indentation depth (h_c). Area was determined by calibration of the tip geometry as a function of penetration depth h_c determined by:

$$A_p(h_c) = 2.698h_c^2 + C_1h_c^1 + C_2h_c^{1/2} + C_3h_c^{1/8} + C_4h_c^{1/16} + C_5h_c^{1/32}$$

E_r accounts for the effects of a non-rigid indenter and is determined by:

$$\frac{1}{E_r} = \frac{(1-\nu_i^2)}{E_i} + \frac{(1-\nu_s^2)}{E_s}$$

where the terms E and v represent modulus and Poisson's ratio, respectively, with the subscripts *i* and *s* representing the indenter and sample. Stiffness measurements were made by fitting the unloading of an indent to a power law function using regression analysis:

$$P = A(h - h_f)^m$$

where P is the load, h is the indenter displacement, h_f is the permanent deformation caused from the indent. A and m are modeling constants with A being material dependent and m depending on the indenter geometry. This allows the slope at the initial unloading to be calculated analytically and reduces the dependence of the method on the amount of creep occurring in the samples. While localized stresses such as those produced during nanoindentation may create concentration gradients and local variations in mechanical properties, these effects were not considered in our calculations.[112]

The hardness was calculated using the area function shown above and the maximum load of the indent, as shown below:

$$H = \frac{P_{max}}{A_p}$$

Results & Discussion

Figure 6.1a shows the cross-sectional micrograph of the deposited Si film. The films' thicknesses obtained from SEM were in a good agreement with what we obtained from the mass changes observed in the sample after CVD deposition, assuming the density of the deposited Si to be 2.3 g/cm3. XRD confirmed the formation of nanostructured Si. In contrast to Si CVD deposited at 500 °C, which showed XRD-amorphous microstructure, the deposition performed for the current studies at 750 °C revealed distinct Si peak formation. [104, 113] Figure 6.1b shows a typical high-resolution portion of the XRD pattern for the as-deposited unlithiated Si thin film. The broad Si peak visible at 28.7 corresponds to diffraction from the {111} family of planes. Using an instrumental standard and the Scherrer method, the average grain size can be calculated as 74 nm.

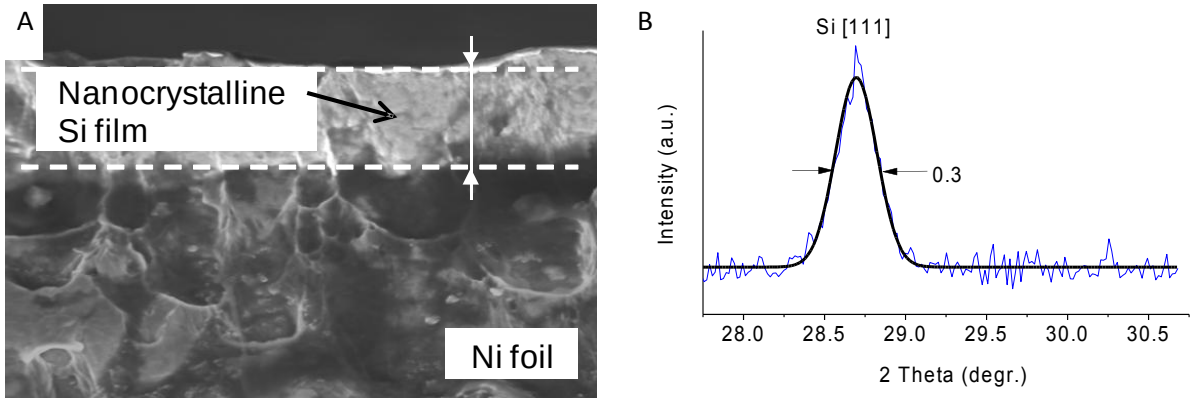

Figure 6.1: (a) Cross-sectional SEM micrograph of a CVD-deposited Si film on C-coated Ni foil substrate, (b) high-resolution X-ray diffraction spectrum of the Si film

Figure 6.2a shows an example of the galvanostatic Li insertion profile for the produced Si film anodes. The shape of the profile is similar to the profiles previously reported in literature for other Si electrodes. In contrast to intercalation-type electrode materials, these profiles do not exhibit horizontal plateaus and cover a larger potential range. The following constant potentials were selected for the electrochemical alloying: 0.174 V (for LiSi), 0.137 V (for $Li_{1.68}Si$), 0.078 V (for $Li_{2.61}Si$) and 0.010 V (for $Li_{3.75}Si$). Please note that Li losses due to SEI formation (no more than 1%, estimated) were neglected in our calculations of the alloys' composition. The large Si film thickness and high Si capacity justifies this assumption.

Examples of typical load vs. displacement curves for nanoindentations on lithium-silicon thin films are presented in Figure 6.2b. These graphs show the load-unload behavior for pure Si films and for Si films lithiated to different final compositions. We can see the progressive transformation of the material as more lithium is inserted. At the same value of the applied load the nanoindenter tip penetrates to larger depth for higher Li content, indicating a systematic reduction in hardness upon Li insertion into Li-Si alloy. The slope of the unloading curve also decreases with increasing degree of lithiation, suggesting a reduction in Young's modulus.

Unlike previously investigated amorphous Si thin films, we did not observe "pop-out" on the unloading curves for any of the produced samples, including the as-deposited Si.[115] In pure Si these "pop-out" features are associated with phase transformations (often from an amorphous to a crystalline phase) beneath the indenter induced by pressure changes and accompanied by an abrupt volume increase.[115-117] Our observation may suggest the lack of pressure-induced amorphous-to-crystalline and crystalline-to-crystalline transformations in our indentation experiments on electrochemically produced Li-Si alloys. Interestingly, in roughly every 4th-5th experiment (independently on the degree of lithiation) we observed an "elbow" in the unloading curves (Figure 6.2c). In pure Si this feature is associated with crystalline-to-amorphous phase transformations.[116] If this is also true for Li-Si alloys, then this observation suggests the presence of nanocrystalline grains not only in the produced Si (Figure 6.2c) but also in all the lithiated films.

Figure 2d shows the load vs. displacement curves for the $Li_{1.08}Si$ sample taken at varying loads. While some variation in the loading curves is observed, the slopes of the unloading curves are commonly very similar, indicating high degree of homogeneity of the elastic modulus throughout the sample. The slopes of the unloading curves were used to determine the average Young's modulus of our samples, according to the procedure describe in the experimental section. Figure 6.2e shows the changes in the Young's modulus as a function of the volume fraction of lithium in the film, calculated assuming theoretical values for the density and molar mass of Li and Si. For comparison purposes, we have also included a theoretical measurement of the Young's modulus based on a linear rule of mixtures, as shown below:

$$E = E_{Li}V_{Li} + E_{Si}V_{Si}$$

where V_{Li} and V_{Si} are the volume fractions of Li and Si, respectively, in the film, and E_{Li} and E_{Si} are the experimentally determined Young's modulus of microcrystalline Li and nanocrystalline Si films respectively. Note that the atomic and volume fractions are very similar (no more than 4% difference). In addition, we added to the graph the DFT-calculated values for several crystalline and amorphous Li-Si alloys [111] and the experimental values from [112].

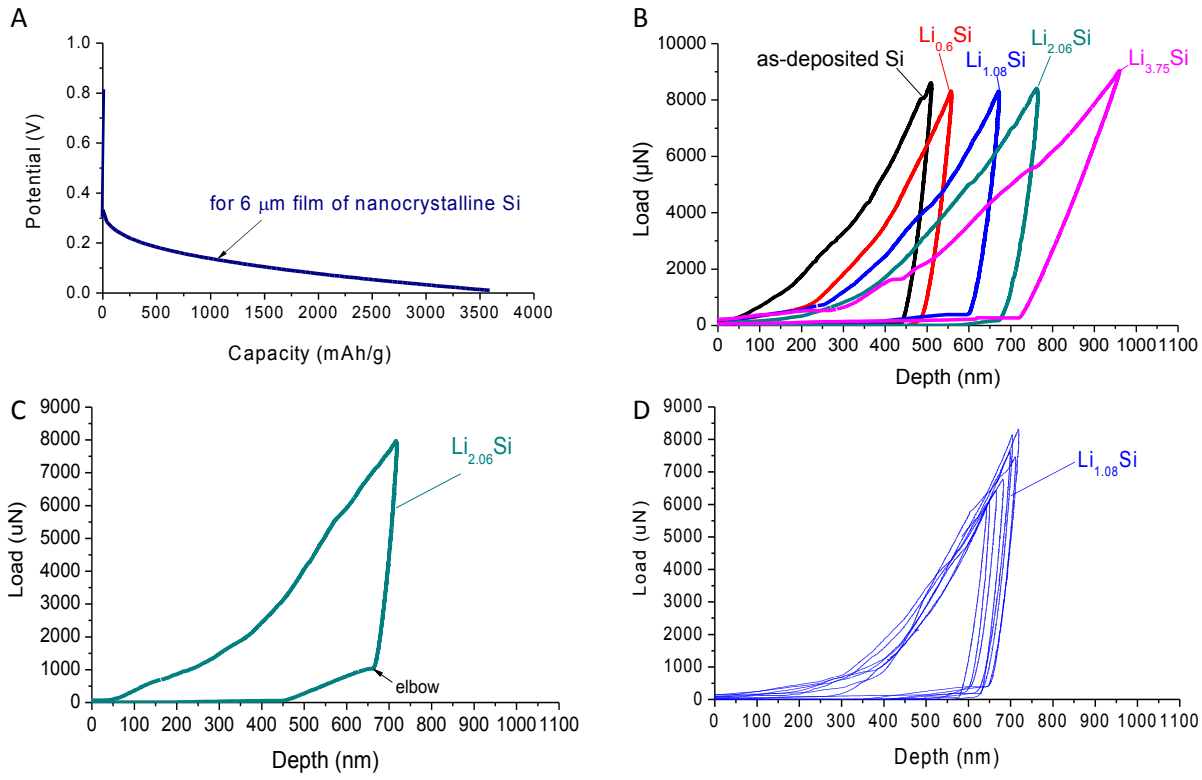

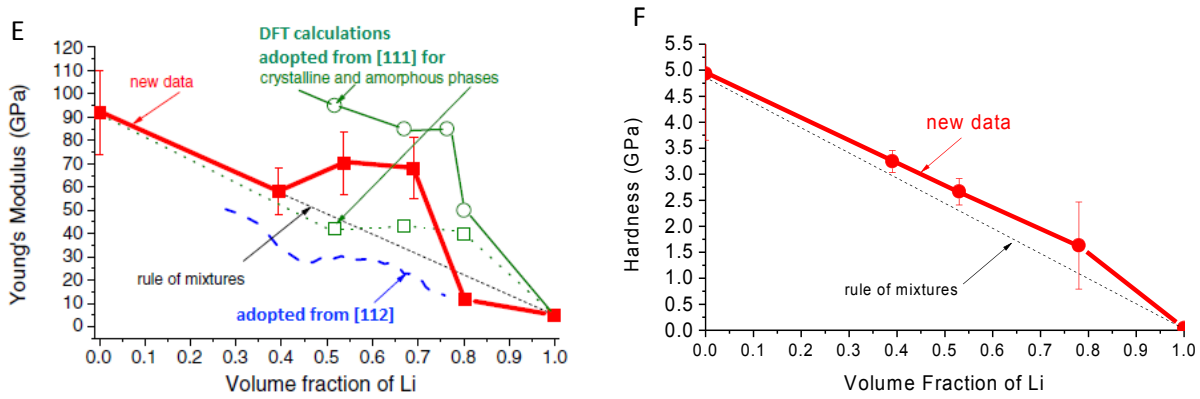

Figure 6.2: (a) Electrochemical profile for lithium insertion into nanocrystalline Si film, (b) load-displacement curves for Si film samples at various stages of lithiation; (c) a load-displacement curve with an "elbow" in the unloading curve; (d) load-displacement curves for Si film lithiated to Li1.08Si; (e) Young's modulus of Li-Si alloys as function of volume fraction of Li; (f) hardness of Li-Si alloys as function of volume fraction of Li

The Young's modulus of nanocrystalline Si film measured from the load-unload curves was found to be 92 GPa, close to the values reported for amorphous (90 GPa) silicon.[111] The Young's modulus of Li was determined to be 5 GPa, consistent with the value reported in the Goodfellows catalog.[112] Our experiments show when the thin film is lithiated to $Li_{0.6}Si$, the modulus decreases linearly to a value of 58 GPa, as would be predicted by the rule of mixtures. Interestingly, however, higher degree of lithiation to ~$Li_{1.08}Si$ and $Li_{2.06}Si$ leads to the increase in the Young's modulus. A similar increase was also observed in [112], although the absolute values of the Young's modulus is higher in our measurements. Specifically, in this range the Young's modulus remains constant at ~70 GPa, significantly exceeding the linear rule of mixtures. This value, however, is an average between the DFT-predicted Young's modulus for amorphous and crystalline phases of similar compositions.[111] The value of the Young's modulus is related to the average stiffness of inter-atomic bonds. However, the charge state of individual atoms, the ionic character and the stiffness of individual Si-Li (and, to a smaller degree, the stiffness of Si-Si and Li-Li) bonds as well as the number of such bonds should

strongly depend not only on the Li fraction but also on the position of a particular atom and its surrounding.[111] Therefore, the observed deviations from the rule of mixtures are believed to be reasonable even for nanocrystalline or amorphous films. Another interesting observation was the steep decrease in Young's modulus from ~70 GPa to ~12 GPa for samples lithiated to a maximum level ($Li_{3.75}Si$ or Li15Si4). A somewhat similar (yet, smaller in magnitude) decrease was predicted for crystalline phase but not for amorphous one.[111] We propose that such sharp decrease in Young's modulus could be related to the formation of Li-reach areas in the grain boundary regions within the sample, which may control the overall elastic properties of the sample.[106] It is also possible, that vacancies or microvoids could form within the film after the Li insertion, when the film partially transforms from amorphous $Li_{3.75}Si$ to the thermodynamically more stable (nano)crystalline $Li_{15}Si_4$ phase, which would also decrease the Young's modulus. Changes in the hardness of the nanocrystalline Si film upon lithiation, as estimated from the load vs. displacement curves, were observed to exhibit few features (Figure 2f). The hardness varies linearly with the volume fraction of Li in the film. The fully lithiated film remains considerably harder than Li metal and retains about 30% of the hardness of the as-deposited Si.

Conclusion

Having successfully analyzed the Young's modulus and hardness of Si and Li-Si alloys at various stages of lithium insertion, we now have information useful for a range of different modeling efforts. This information can be used to better understand the deformation of composite anode particles during lithium insertion and extraction. It can also be used to better understand the stresses produced during expansion of these particles in confined spaces. We will

use this information to quantify the surface stresses produced during lithium insertion and extraction. This information will be useful in applying the results of our analysis of changes occurring in SEI composition with differing levels of surface stress to a wide range of nanocomposite materials.

6.3 Modeling Structural Changes During Nanocomposite Lithiation

Introduction

The structural and microstructural changes occuring within anodes of Li-ion battery anodes during Li insertion and deinsertion are an area of extensive current investigation. The reason for this is that mechanical degradation is one of the major factors limiting the performance of Si as a Li-ion battery anode material. The extreme volume changes produced by Si expansion during Li insertion and deinsertion create stresses which damage both the binder and the active material, leading to rapid loss of capacity. It is possible to improve the performance of Si-based anodes, however, via rational design of electrode materials. Modeling the mechanical effects of Li insertion and deinsertion on the active material is essential to this effort.

The evolution of stresses within single electrode particles has been extensively modeled. A study initiated by Y.T. Cheng found that the charging conditions have a significant impact of the evolution of stress during Li insertion and deinsertion. During potentiostatic charge and discharge, the magnitude of stresses – as well as the strain energy – at any location within an active particle increases initially, then decreases over time, whereas these factors tend to reach a steady-state value during galvanostatic control.[118] Further investigations developed analytical solutions permitting analysis of the evolution of stresses within a single electrode particle during

Li insertion and deinsertion. These models took into account both the stresses produced by Li insertion and those produced by diffusion, as well as the impact of charging conditions on stress distribution in a steady-state equilibrium.[119] The evolution of stress within silicon in particular was investigated by R. Chandrasekaran. This model accounts specifically for the large volume changes occurring within Si nanoparticles during Li insertion and deinsertion, as well as the amorphization process produced by Li alloying. The study analyzed the effects of particle size and charging parameters as well as kinetic parameters such as Li^+ diffusivity and the path dependence of Li^+ alloying thermodynamic potential.[103]

The evolution of stress in active material other than spherical nanoparticles has also been modeled. One study, led by R. Deshpande, modeled Li insertion and deinsertion in Si nanowires. This analysis focused specifically on diffusion-induced stresses, on the basis that they would be the primary factors in inducing crack propagation. This study found that surface energy and surface stresses can have a powerful effect in mitigated diffusion-induced stresses, particularly in smaller nanowires, and that surface strain energy was a significant contributor to the total strain energy of the system.[120] Stress evolution in thin films has also been studied. One study analyzed the nucleation of cracks by diffusion induced stresses, much like the previous analysis of Si nanowires. As before, this study found that the evolution of stress in thin films would become manageable, allowing the electrode to become crack-tolerant, if the thickness of the active material was below a certain critical size. While localized deformation occurs during Li insertion, upon deinsertion the deformation would be fully recoverable, preventing crack propagation. As in previous studies, surface stresses were found to be an important factor governing the critical length scale of the electrode.[121]

Certain studies have analyzed the mechanical behavior of the entire electrode, not just the

active anode material. An investigation led by R.E. Garcia used finite elements to study both positive and negative electrodes in a cell with a C anode and a Mn_2O_4 cathode. This model produced a detailed description of the spatial distribution of both electrochemical potential and Li^+ ion concentrations throughout the modeled cell. As in previous models of single particles, the active material particles in this model experienced both compressive surface and bulk tensile stresses simultaneously during Li insertion. This model captured the effects of electrode microstructure on cell performance, showing that an electrode with an active material particle size distribution that was both small and relatively homogeneous would exhibit both higher specific capacity and power, as predicted by experimental results.[122] A subsequent study, led by J. Christensen, modeled stress distribution within porous electrodes, finding that porosity – particularly in thick electrodes – could potentially lead to nonuniform stress distributions, which in turn could produce particle fragmentation and electrode disordering. This study also found that in porous electrodes with large-volume-expansion active materials, both pressure diffusion and nonlinear lattice expansion were important in its electrochemical and mechanical response of active material particles. In conventional electrode materials, however, only nonlinear lattice expansion had a significant effect.[123] Other studies have focused specifically on silicon as a subject of investigation. One study, led by A.F. Bower, formulated a new finite elements-based model which treated the mechanical response of the electrode material as plastic deformation, rather than being purely elastic. This has produced a more accurate model of the changes occuring within the electrode, since it has been extensively demonstrated in our own studies that Si thin films and nanoparticles tend to deform plastically during Li deinsertion. This model also accounts for the effect of stress on electrochemical potential within the cell. This model showed that the Si thin film deformed as a viscoplastic material, and that the stresses produced within the

electrode impacted the rest potential of the cell, in addition to the potential of reactions during Li insertion and deinsertion.[124]

We have developed two simple models for better understanding the results of our research. The first is a model for the deformation of Si during electrochemical alloying and de-alloying with Li in a nano-confined space. We have applied this model to the study of the tubular Si-C nanocomposite anode material we developed, which has a Si film deposited on the inner surface of a C backbone, which supplies both mechanical support and electrical conductivity. These studies will help us model the effect of Si film thickness on the microstructural changes of the nanocomposite particles and their electrochemical performance. We have also developed a simple model for quantifying the evolution of stresses throughout a Si-C composite nanoparticle during Li insertion. We have used this model to simulate the production of surface stresses during the expansion of a C-coated nano-Si particle for a variety of different coating thicknesses. This model will help us apply our previous studies on the impact of surface stresses on the composition of stability of the SEI to a wide variety of other nanocomposite materials.

Experimental Methods

To model the expansion of and contraction of the Si-Li alloy film, we have developed a simple lattice-based spring model (LSM) which simulates a viscoplastic material.[125] This model represents a solid material as a network of springs with Hooke's constant k and rest length l_0. These springs connect together a network of point masses. Elastic deformation of the Li-Si alloy film corresponds to the compression and extension of the springs. The network is assumed to yield plastically at a yield strain ε_y, which is modeled by changing the spring rest length l_0 to satisfy the following constitutive law:

$$\sigma = \begin{cases} E\varepsilon, & |\varepsilon| < \varepsilon_y \\ E\varepsilon_y sign(\varepsilon), & |\varepsilon| > \varepsilon_y \end{cases}$$

Here, σ is the stress to which the material is being subjected and E is the material's Young's modulus. In our simulations, we set $\varepsilon_y = 0.005$. The process of Li insertion and extraction is modeled by gradual changes in the rest length, l_0. The nanocomposite particle is modeled as a two-dimensional shell, constructed from concentric layers of uniformly distributed nodes. Each individual layer contains 157 LSM nodes. The radial layers are separated by a distance equal to the average distance between the nodes within each of the layers in contact with one another. The springs comprising the LSM network connect the nearest and next-nearest neighbor nodes. Within this spring arrangement, the Poisson's ratio of the solid is $\upsilon = 0.25$, and the Young's modulus is $E = 5k/2l_0$. Since we are only interested in the difference between the initial and final states of the nanocomposite particle in this investigation, we have assumed that the Young's modulus is constant; changes in the modulus during lithiation will be relatively unimportant in determining its post-delithiation microstructure. The elastic energy associated with a node at any given position r_i is $E = 0.5\Sigma_j k(r_{ij} - l_0)^2$, where r_{ij} is the length of the spring between two neighbor nodes. This elastic energy produces a force $F = \partial E/\partial r$. We model the microstructural changes occurring in the nanocomposite particle as a procession of a series of equilibrium states, since Li insertion and extraction are relatively slow processes. Since the deformation of the Li-Si alloy film is limited by repulsive interatomic forces, the system is modeled as a set of overdamped springs. This model is achieved by introducing a dissipative force, where the spatial positions of each node is iterated using the velocity Verlet algorithm until the forces on each node are balanced.

In order to model the expansion of C-coated nano-Si particles, we use a commercial finite

element method program (ANSYS) to simulate the particle's mechanical expansion. Finite element analysis solves partial differential equations to model a range of different mechanical, thermal, electrical or magnetic phenomena, without producing numerical instability from small errors that can render the output of the model meaningless. This software permits us to analyze the impact of the large deformations and strains produced during expansion of the nano-Si core particle. We have used the results of our previous investigation on the mechanical properties of lithiated Si thin films to determine the mechanical properties of the simulated nanoparticle. The carbon coating is assumed to have an elastic modulus of 140 GPa and a Poisson ratio of 0.26, appropriate for graphitic carbon. Its mechanical properties are assumed to remain unchanged during lithiation.[126] The Si nanoparticle has an initial radius of 25 nm, and is assumed to be spherical. To save processing time, the particle is only simulated in two dimensions, and only 1/4 of the circular cross-section of the particle is used. Symmetric boundary conditions are used to maintain accuracy. The Li insertion process is simulated by thermal expansion. In particular, we adjust the thermal expansion coefficient to match the volume change and change in materials properties from our experimental data. The outer carbon shell is assumed to remain adhered to the surface of the inner Si core. Since Li insertion is a relatively slow process, we model the evolution of the shell as proceeding through a series of equilbrium states. These assumptions permit us to apply a static analysis. After the expansion, the final strain experienced by the outer surface of the carbon shell is obtained from the simulation. The total mechanical and thermal von Mises stress is used, since lithiated Si tends to behave viscoplastically, rather than principle strain criteria, which are used primarily in materials exhibiting brittle behavior. We did not apply a model for plastic deformation, since the precise form of plastic deformation by which the C outer shell accommodates the extreme expansion of the Si-Li alloy core is unknown. Five different

particles with identical carbon shell thicknesses are simulated.

Results & Discussion

Our computational model of an viscoplastic ring contained within a circular constraint is shown in Figure 6.3. This model simulates a 33% Si by weight nanocomposite particle. Here, we assumed the the volume changes in the tube will be compensated entirely by the internal pore space, leading to no net changes in either particle thickness or tube length. In this model, we see that the Si tube is initially attached to the walls of the pore (Figure 6.3a). During the insertion of Li, the rigid matrix restricts the expansion of the inner tube, forcing the Si-Li alloy film to expand inward, decreasing the internal diameter of the cylinder (Figure 6.3b). This inward expansion is accompanied by plastic deformation, as per the formula described previously. This model assumes that the adhesion between the Si and C surfaces is low enough to be broken by the stresses produced during Li insertion and extraction, as demonstrated for a nanocomposite particle of these dimensions and composition by our previous experiments. As a result, when Li is extracted from the alloy shell, the tube does not return to its initial geometry, but instead shrinks to a small size. During this contraction, the inner tube separates from most of the matrix wall, except for a small area which maintains strong adhesion and electrical contact (Figure 6.3c). During Li insertion in consecutive cycles, the separated tube will expand outwards until its outer diameter matches the size of the pore. After the first cycle, Li insertion and deinsertion shifts the tube between its expanded and contracted configurations (Figs. 6.3b-c). Only the first Li insertion causes a permanent change in the microstructure of the electrode material; subsequent cycles produce only reversible changes.

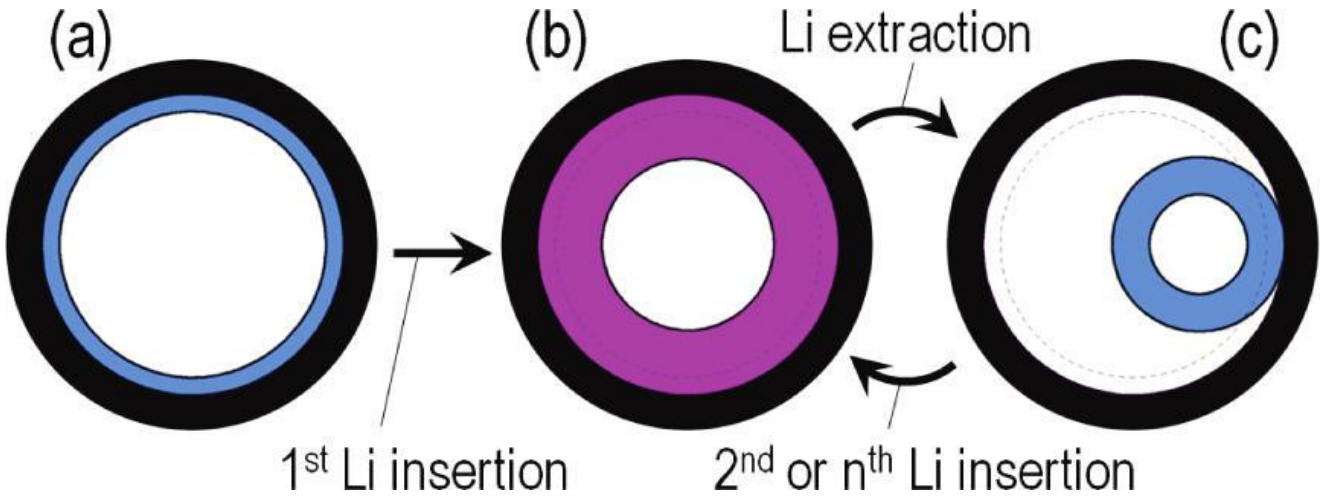

Figure 6.3: Results of lattice-based spring model of shape changes occuring in a Si thin film inside a rigid C tubular nanopore (a) before Li insertion, (b) at full Li insertion, and (c) after complete Li extraction

Our finite element method model of a Si-C core-shell nanoparticle at full lithium intercalation is shown in Figure 6.4 below. The model shown in Figure 6.4a simulates a Si-C core-shell nanoparticle with a carbon shell coating of 11 nm thickness. In this model, we see that the highest strains occur at the interface between the Si core and the C shell; the rest of the C shell experiences smaller strains, with the minimum C shell strains occurring at the outer surface of the nanoparticle. Strains within the Si core itself are high, due to the high elasticity of the fully lithiated Si. The graph shown in Figure 6.4b shows the Von Mises mechanical strain on the outer surface of the carbon shell – in an actual electrode, the interface between the electrode active material and the solid-electrolyte interphase. We see from this graph that the strain at the outer surface of the nanoparticle decays exponentially with increasing C shell thickness, producing diminishing returns in strain reduction with increasing C shell thickness. Although the model predicts strains for very thin C coatings, these results may not be possible to duplicate experimentally, since very thin C coatings are likely to fracture during lithium insertion, due to their brittle nature.

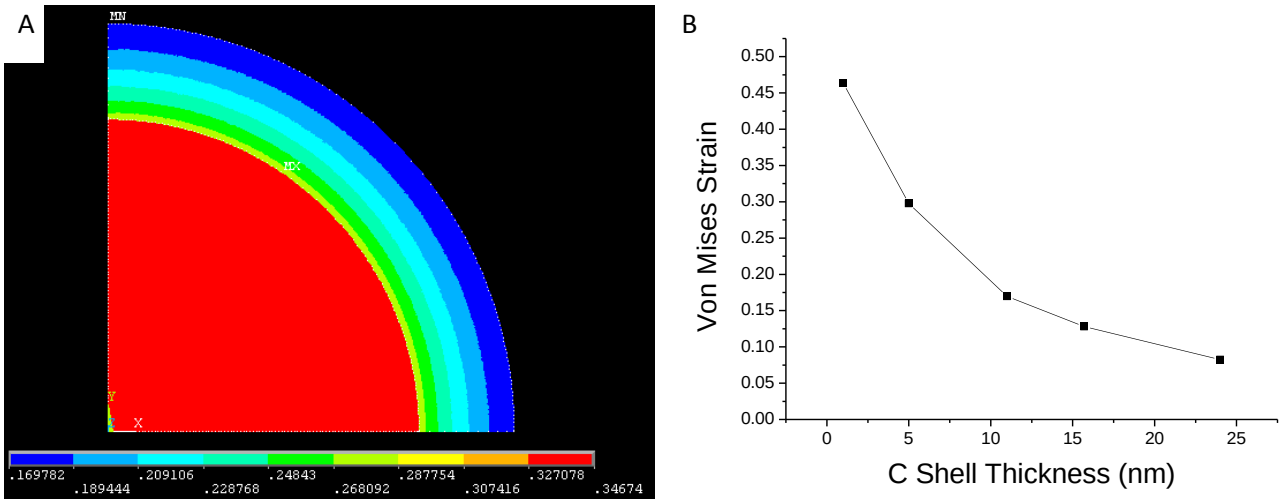

Figure 6.4: Results of finite elements method simulation of C-coated nano-Si nanoparticles. a) Visual representation of distribution of Von Mises mechanical and thermal strains within fully lithiated nanoparticle; b) Von Mises strain on C shell outer surface for a range of different C shell thicknesses

The Von Mises strain, shown in Figure 6.4a above, is comprised of multiple different individual strains. The two primary strains on the C shell produced by the expansion are a compressive strain parallel to the radius (the 3rd principle strain) and a tensile strain on the C shell perpendicular to the radius (the 1st principle strain). These strains are both factored into the calculations used to determine the Von Mises strain, which is the best method available for calculating the net strain on the shell. These strains as a function of radial distance from the center of the Si-C core-shell nanoparticles are shown below, in Figure 6.5. From this figure, we can see that the strains within the Si-Li core is invariant with distance – a product of our assumption in this model that the core nanoparticle will be lithiated uniformly. The strain on the outer shell, however, drops off significantly with distance. The strains at the Si-C interface are extremely high, with ~45% total elongation, but the strain on the outer surface is low enough that the net elongation is just 8%. The compressive 3rd principle strain drops off much faster than the

normal 1st principle strain, such that at the nanoparticles surface the compressive strains are virtually eliminated and the Von Mises strain is determined almost entirely by the elongation normal to the radius.

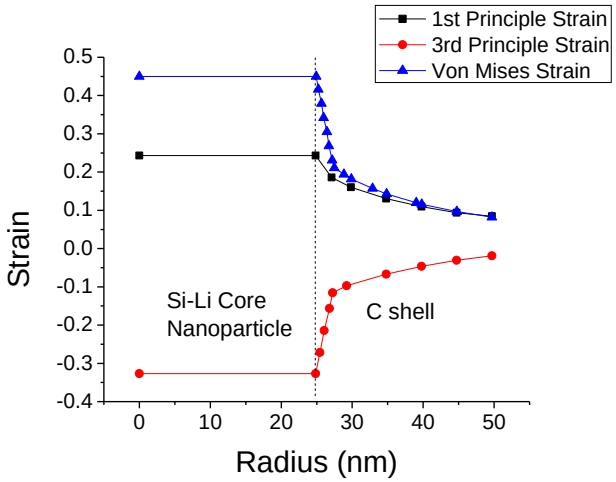

Figure 6.5: Strain within lithiated Si-C core-shell nanoparticles as a function of radial distance from the nanoparticle's center, including normal (1st principle), radial (3rd principle) and net (Von Mises) elongation.

Conclusion

It is possible to model the process of Li insertion and deinsertion into Si thin films or nanoparticles using numerical methods. Both lattice-based spring models and finite element models have proven effective in modeling this reaction. Our lattice-based spring models have successfully simulated the irreversible structural changes occurring in Si thin films during Li insertion and deinsertion within a rigid cylindrical pore. These simulations have demonstrated that Li-Si alloys undergo deformation behavior best understood as viscoplastic, rather than exhibiting the brittle behavior of pure Si. It has also demonstrated that this deformation can be treated as fully reversible after the first Li insertion/deinsertion cycle. Our finite elements analysis has successfully modeled the expansion of Si-C core-shell nanoparticles with a range of different C shell thicknesses, and has derived the total mechanical von Mises strain throughout

the nanoparticle at full Li insertion. These strain values can be correlated to our previous analysis of SEI composition and stability via XPS, indicating the effects of various degrees of quantified strain on the performance of an electrochemical cell. We can therefore develop new models using this methodology to predict the SEI composition and stability of new nanocomposite materials, enabling us to better design electrode materials. All of this information can be used in future modeling efforts.

7. Conclusion

In order to develop a better understanding of the fundamental properties of Si-C nanocomposite electrodes, we have studied a range of different electrode materials of our own design. We have successfully produced Si-C nanocomposite electrode materials via a templating process. These materials are produced via chemical vapor deposition of silicon and carbon thin films onto an alumina template with cylindrical pores, which is then etched away via HF. These materials incorporated a Si thin film which provided excellent capacity and a C outer shell that provided electrical conductivity as well as a mechanical backbone. Our studies of this material showed it to have high reversible capacity at both C/20 and C/1 rates, with excellent capacity retention, cycle life and Coulombic efficiency. We analyzed the impact of Si film thickness and pore space. Our studies of this material demonstrated the importance of internal porosity to electrode cyclability. Due to their internal void space, the active material was able to buffer the expansion of the Si electrode material without any net change in volume, preventing damage to the electrode and maintaining mechanical stability. Our investigation also revealed the unusual structural changes occurring within the active material – during Li insertion and deinsertion, the Si thin film would deform plastically. This occurred in electrodes where the film was thick enough that internal stresses could overcome the adhesion between Si and C during Li insertion. These deformations reduced the capacity of the cell by exposing part of the C shell to electrolyte, causing SEI growth there, which increased the impedance of the electrode. We also studied the effect of microstructure and crystallinity of Si thin films. We found that annealing the active material could improve its capacity, since annealing would remove some of the internal stresses and improve adhesion. As a result, annealed samples suffered less extreme deformation during Li insertion/deinsertion. Blocking direct access of electrolyte to the pore also improved capacity

at slow charge/discharge rates, by reducing the impedance of the active material, but the capacity at during faster charge/discharge rate, since Li diffusion was reduced.

In our investigation of self-assembled granular nanocomposites, we have developed methods for producing and characterizing a new form of nanocomposite electrode material. This methodology produces a granular internally porous Si-C nanocomposite material via self-assembly of Si-nanoparticle-decorated C particles, induced via chemical vapor deposition. The internal pores of this material permit the expansion of the Si nanoparticles, which are deposited on branching, chain-like C particles which provide electrical conductivity and form the structural backbone of the granular particle. This material exhibits extremely high capacity at both C/20 and C/1 rates, with excellent reversibility. It also exhibits low capacity fading and extremely long cycle life. The kinetics of the material were significantly superior to graphitic anode materials – the nanocomposite electrode retained a much higher percentage of its capacity when cycled at C/1 and 8C rates than a graphite electrode did. Examination of the composition of the SEI via XPS at various points during the cell's cycle life revealed that the electrode possesses excellent long-term stability, with a final composition after 200 cycles highly similar to its initial composition after just 10 cycles.

In addition to our study of various synthesis methods, we have performed more general studies on the effects of various electrode fabrication parameters on performance. We have studied the impact of binders on conventional nano-Si electrodes with conductive additives. We investigated four different binder materials – PVDF, which is a typical binder for commercial Li-ion graphitic electrodes, CMC, which is a common electrode material used in the literature for nano-Si electrodes, and two new materials: PAA and alginate, which have an extremely high percentage of carboxyl groups, which we believe to improve the performance of Li-ion

electrodes. We studied the binder-electrolyte interaction by testing the swellability of binder films in an atmosphere of carbonate vapor. We found that the PAA and alginate binder films showed the lowest swellability, indicating minimal binder-electrolyte interaction. We also tested the mechanical properties of binder films before and after immersion in carbonates, and found that while PVDF films dropped significantly in stiffness after immersion, Na-CMC and PAA films changed little, and alginate films didn't change at all. Our electrochemical studies of electrodes made with these materials showed that the alginate-based electrodes exhibited the highest capacity, with the best capacity retention and Coulombic efficiency. Carbon-coating the nano-Si particles also seemed to produce better results in terms of both capacity and efficiency, rather than adding more conductive additives. Analysis of the SEI properties of the PAA and alginate electrodes via XPS showed that the alginate electrodes exhibited superior performance, maintaining the same SEI composition between 10 and 200 cycles. The PAA electrode material showed poorer results, with the 200-cycle SEI composition being significantly different than the 10-cycle composition. These results show that the carboxyl group content of binders can have a significant impact on their performance as an electrode material. Binders with higher carboxyl group content improve electrode capacity, efficiency, and cycle life.

We also investigated the impact of different thicknesses of carbon coating on electrode performance. Different shell thicknesses will affect the performance of Si-C core-shell nanoparticles. As the C shell becomes thicker, the surface stresses on the outer surface of the nanoparticle will diminish, affecting the composition and stability of the SEI. We produced Si-C core-shell nanoparticles with three different C shell thicknesses – 11 nm, 15.7 nm, and 24 nm. We tested these samples, along with control Si and C nanoparticles. We found that nanoparticles with very thin or very thick C shell thicknesses tended to exhibit the best performance, and that

electrodes with very thin or moderate C shell thicknesses tended to exhibit poorer Coulombic efficiency. Electrodes made with nanoparticles of moderate C shell thickness exhibited poorer performance. Examining SEI composition via XPS for our samples, we found that the nano-Si active materials with any degree of carbon coating exhibited greater chemical stability than those without, but that only those with C shell thickness equal to or greater than ~15 nm maintained constant SEI thickness over most of the lifetime of the electrode. The granular nanocomposite exhibited excellent SEI stability, similar to the pure carbon electrode we tested, suggesting that complete lack of net volume change in the active material is key to optimal stability. Nanocomposite electrode materials should be designed with C shells thick enough to minimize surface stresses, thereby improving SEI stability and Coulombic efficiency.

In order to improve the rational design of electrodes, we must build up an extensive base of knowledge to enable modeling of nanocomposite materials. Modeling will permit us to develop nanocomposite electrodes more efficiently. We have studied the mechanical properties of silicon thin films at various stages of lithium insertion via nanoindentation. We deposited a 6 μm thick film of Si onto a C-coated Ni foil, and then inserted Li into it electrochemically. We then placed these films into an inert atmosphere nanoindenter. Our investigation revealed the elastic modulus of the electrode material to be substantially higher than previous in-situ measurements from the literature made via optical beam sensors had suggested, and to be mid-way between crystalline and amorphous estimates of the modulus made via DFT calculations. We also found that the modulus of the Si thin film dropped precipitously at full lithiation, possibly due to the formation of micro-voids within the film. The hardness of the film corresponded to a linear rule of mixtures, as would be expected from an amorphous solid solution.

These measurements have provided us with valuable information for our modeling efforts. We have developed models for both our template-derived tubular nanocomposites and for Si-C core-shell nanoparticles. Our models of template-derived tubular nanocomposites have successfully simulated the deformation of the Si thin film within these nanoparticles. The success of this simulation indicates that the viscoplastic model we used for the deformation behavior of the film is an accurate estimation of the real properties of lithiated silicon. Our models of Si-C core-shell nanoparticles, incorporating our measurements of the mechanical properties of lithiated Si, allow us to quantify the evolution of stresses within nanocomposite particles during Li insertion. These measurements can be combined with our previous studies of changes in SEI composition with changing C shell thickness to predict the optimal shell thickness for maximization of electrode capacity and cyclability.

In conclusion, we have studied the influence of a variety of different factors on the performance of Li-ion battery electrodes. We have developed a valuable base of information to help the future development of rationally designed Si-C nanocomposite electrode materials. With this information, future research efforts can select the optimal film or particle size and pore size for their materials, as well as select an appropriate binder for use in their electrodes. This information will help the development of commercially viable Si-C nanocomposite electrodes, enabling the development of Li-ion batteries with higher energy and power density.

References

[1] M.S. Whittingham, Electrical Energy Storage and Intercalation Chemistry, Science, 11 (1976) 1126-1127.

[2] S.C. R. Jasinski, Thermal Stability of a Propylene Carbonate Electrolyte, J. Electrochem. Soc., 117 (1970) 218.

[3] R.K. D. Fauteux, Rechargeable Lithium Battery Anodes: Alternatives to Metallic Lithium, J. Applied Electrochem., 23 (1993) 1-10.

[4] A. Hérold, Recherches sur les composes d'insertion du graphite, Soc. Chim. Fr., 187 (1955) 999.

[5] R.R. Agarwal, Phase Changes and Diffusivity in the Carbon-Lithium Electrode, J. Power Sources, 25 (1989) 151-158.

[6] M.M. Thackeray, Lithium Insertion into Manganese Spinels, Mat. Res. Bull. , 18 (1983) 461-472.

[7] Y.G. D. Aurbach, J. Langsam, The Correlation Between Surface Chemistry, Surface Morphology, and Cycling Efficiency of Lithium Electrodes in a Few Polar Aprotic Systems. , J. Electrochem. Soc., 136 (1989) 3198.

[8] T.F.R. R.D. Rauh, S.B. Brummer, Efficiencies of Cycling Lithium on a Lithium Substrate in Propylene Carbonate, J. Electrochem. Soc., (1978) 186.

[9] J.L.G. K.M. Abraham, D.L. Natwig, Characterization of Ether Electrolytes for Rechargeable Lithium Cells, J. Electrochem. Soc., 129 (1982) 2404.

[10] M.M. K. Takata, T. Yamashita, Conductivity of the LiBF/Mixed Ether Electrolytes for Secondary Lithium Cells, J. Electrochem. Soc., 131 (1984) 2821.

[11] K.X. S.S. Zhang, T.R. Jow, Understanding Formation of Solid Electrolyte Interface Film on LiMn2O4 Electrode, J. Electrochem. Soc., 149 (2002) A586.

[12] R.A. Wiesboeck, Tetraacetonitrilolithium Hexafluorophosphate, Tetraacetonitrilolithium Hexafluoroarsenate, and Method for the Preparation Thereof, in: U.P. Office (Ed.), vol. 3,654,330, 1972.

[13] U.Heider, Liquid Electrolyte Systems for Advanced Lithium Batteries, Proceedings of 1997 Battery Technology Symposium, (1997).

[14] Y.K. J.B. Goodenough, Challenges for Rechargeable Li Batteries, Chem. Mater., 22 (2010) 587-603.

[15] K. Xu, Nonaqueous Liquid Electrolytes for Lithium-Based Rechargeable Batteries, Chem. Rev., 104 (2004) 4303-4417.

[16] P.B. R. Selim, Some Observations on Rechargeable Lithium Electrodes in a Propylene Carbonate Electrolyte, J. Applied Electrochem., 121 (1974) 1457.

[17] W.S. Harris, Electrochemical Studies in Cyclic Esters, in, vol. Ph. D., University of California, Berkeley, CA, 1958.

[18] Y.C. C.A. Angell, Crystallization and vitrification in aqueous systems. , J. Microsci., 141 (1986) 251.

[19] U.v.S. R. Fong, J.R. Dahn, Studies of Lithium Intercalation into Carbons Using Nonaqueous Electrochemical Cells, J. Electrochem. Soc., 137 (1990) 2009.

[20] M.D.R. G. Pistoia, B. Scrosati, Study of the Behavior of Ethylene Carbonate as a Nonaqueous Battery Solvent, J. Electrochem. Soc., 117 (1970) 500.

[21] A.M.C. F. Coowar, P.G. Bruce, and C.A. Vincent, Improving the Performance of Graphite Anodes in Rechargeable Lithium Batteries, J. Power Sources, 75 (1998) 144-150.

[22] J.M.T. D. Guyomard, Rechargeable LiMnO/Carbon Cells with a New Electrolyte Composition, J. Electrochem. Soc., 140 (1993) 2490.

[23] S.S. Zhang, A Review on Electrolyte Additives for Li-ion Batteries, J. Power Sources, 162 (2006) 1379-1394.

[24] T.A. T. Sasaki, Y. Iriyama, Suppression of an Alkyl Dicarbonate Formation in Li-ion Cells, J. Electrochem. Soc., 152 (2005) 2046-2050.

[25] H.J.S. C. Korepp, T. Fujii, 2-Cyanofuran – a Novel Vinylene Electrolyte Additive for PC-based Electrolytes in Li-ion Batteries, J. Power Sources, 158 (2006) 578-582.
[26] A.Y. K. Miura, and M. Tanaka, Electric States of Spinel LixMn2O4 As A Cathode Of The Rechargeable Battery, Electrochimica Acta, 41 (1996) 249-256.
[27] K. Mitzushima, LixCoO2 (0< x≤ 1): a New Cathode Material for Batteries of High Energy Density, Mat. Res. Bull., 15 (1980) 783.
[28] J.M.T. G.G. Amatucci, L.C. Klein, CoO, The End Member of the LiCoO Solid Solution, J. Electrochem. Soc., 143 (1996) 1114.
[29] S. Levasseur, Evidence for structural defects in non-stoichiometric HT-LiCoO2: electrochemical, electronic properties and 7Li NMR studies, Solid State Ionics, 128 (2000) 11.
[30] G.P. G.A. Nazri, Lithium Batteries: Science & Technology, Springer, New York, 2004.
[31] K.S.N. A.K. Padhi, and J.B. Goodenough, Phospho-olivines as Positive-Electrode Materials for Rechargeable Lithium Batteries. , J. Electrochem. Soc., 144 (1997) 1188-1194.
[32] S.S. S. Okada, M. Egashira, J. Yamaki, M. Tabuchi, H. Kageyama, T. Konishi and A. Yoshino., Cathode Properties of Phospho-Olivine LiMPO4 for Lithium Secondary Batteries, J. Power Sources, 97-98 (2001) 430-432.
[33] B. Samar, Rechargeable Battery. , in: U.P. Office (Ed.), vol. 4304825, USA, 1981.
[34] K.K. T. Tran, Lithium intercalation/deintercalation behavior of basal and edge planes of highly oriented pyrolytic graphite and graphite powder. , J. Electroanalytic Chem., 386 (1995) 221-224.
[35] J.S. C. Lampe-Onnerud, P. Onnerud, R. Chamberlain, B. Barnett. , Study on High Performing Carbon Materials, J. Power Sources, 97-98 (2001) 133-136.
[36] C.K. M. Endo, K. Nishimura, T. Fujino, K. Miyashita, Recent Development of Carbon Materials for Li-ion Batteries, Carbon, 38 (2000) 183-197.
[37] S.C. Lai, Solid Lithium-Silicon Electrode, J. Electrochem. Soc., 123 (1977) 1196-1197.
[38] A.N. Dey, Electrochemical Alloying of Lithium in Organic Electrolytes, J. Electrochem. Soc., 118 (1971) 1547.
[39] J.H. Ryu, Failure Modes of Silicon Powder Negative Electrode In Lithium Secondary Batteries, Electrochem. Solid State Lett., 7 (2004) 306.
[40] W.-R. Liu, Effect of Electrode Structure on Performance of Si Anode in Li-ion Batteries: Si Particle Size and Conductive Additive, J. Power Sources, 140 (2005) 139.
[41] S. Ohara, A thin film silicon anode for Li-ion batteries having a very large specific capacity and long cycle life. , J. Power Sources, 136 (2004) 303.
[42] W.N. RA Huggins, Decrepitation Model For Capacity Loss During Cycling Of Alloys in Rechargeable Electrochemical Systems, Ionics, 6 (2000) 57.
[43] C.S. Wang, Insertion in Carbon-Silicon Composite Materials Produced by Mechanical Milling, J. Electrochem. Soc., 145 (1998) 2751.
[44] C.W. U. Kasavajjula, A.J. Appleby, Nano- and bulk-silicon insertion anodes for lithium-ion secondary cells. , J. Power Sources, 163 (2007) 1003-1039.
[45] A.M.Wilson, Lithium Insertion in Pyrolyzed Siloxane Polymers, Solid State Ionics, 74 (1994) 249.
[46] M. Holzapfel, A new type of nano-sized silicon/carbon composite electrode for reversible lithium insertion, Chem. Comm., (2005) 1566-1568.
[47] W.R. Liu, Electrochemical Characterizations on Si and C-Coated Si Particle Electrodes for Lithium-Ion Batteries, J. Electrochem. Soc., 152 (2005) A1719.
[48] H.P. C.K. Chan, G. Liu, K. McIlwrath, X.F. Zhang, R.A. Huggins, Y. Cui, High-performance lithium battery anodes using silicon nanowires, Nature Nanotechnology, 3 (2008) 31.
[49] L.F. Cui, Ruffo, R., Chan, C. K., Peng, H. L. & Cui, Y, Crystalline-amorphous core–shell silicon nanowires for high capacity and high current battery electrodes, Nano Lett., 9 (2009) 491-495.

[50] W.R. Liu, Yang, M. H., Wu, H. C., Chiao, S. M. & Wu, N. L. , Enhanced cycle life of Si anode for Li-ion batteries by using modified elastomeric binder., Electrochem. Solid State Lett., 8 (2005) A100-A103.
[51] J. Li, Lewis, R. B. & Dahn, J. R., Sodium carboxymethyl cellulose—a potential binder for Si negative electrodes for Li-ion batteries, Electrochem. Solid State Lett., 10 (2007) A17-A20.
[52] S.D. Beattie, Larcher, D., Morcrette, M., Simon, B. & Tarascon, J. M., Si electrodes for Li-ion batteries—a new way to look at an old problem., J. Electrochem. Soc., 155 (2008) A158-A163.
[53] D. Mazouzi, Lestriez, B., Roue, L. & Guyomard, D. , Silicon composite electrode with high capacity and long cycle life. , Electrochem. Solid State Lett., 12 (2009).
[54] E. Peled, The Electrochemical Behavior of Alkali and Alkaline Earth Metals in Nonaqueous Battery Systems The Solid Electrolyte Interphase Model, J. Electrochem. Soc., 126 (1979) 2047-2051.
[55] A.H. A.M. Andersson, H. Siegbahn, U. Jansson, K. Edstrom, Electrochemically lithiated graphite characterised by photoelectron spectroscopy, J. Power Sources, 522 (2003) 11921.
[56] D.G.a.G.A. E. Peled, Advanced Model for SEI Electrodes in Liquid and Polymer Electrolytes, J. Electrochem. Soc., 144 (1997) L208-L210.
[57] M.T. T. Yoshida, S. Morikawa, C. Ihara, H. Katsukawa, T. Shiratsuchi, J. Yamaki, Degradation Mechanism and Life Prediction of Lithium-Ion Batteries J. Electrochem. Soc., 153 (2006) A576-A582.
[58] N.D. Y. Oumellal, D. Mazouzi, N. Dupr e, J. Gaubicher, P. Moreau, P. Soudan, B. Lestriez, D. Guyomard, The failure mechanism of nano-sized Si-based negative electrodes for lithium-ion batteries, J. Mater. Chem., 21 (2011) 6201-6208.
[59] M.H. Kristina Edstrom, Daniel P. Abraham, A new look at the solid electrolyte interphase on graphite anodes in Li-ion batteries, J. Power Sources, 153 (2006) 380-384.
[60] Y.G. D. Aurbach, M. Benzion, P. Aped, The behaviour of lithium electrodes in propylene and ethylene carbonate: The major factors that influence Li cycling efficiency J. Electroanalytic Chem., 339 (1992) 451-471.
[61] J.C. Vickerman, Surface Analysis: The Principal Techniques, John Wiley & Sons, 2009.
[62] P.M. P. Verma, P. Novak, A review of the features and analyses of the solid electrolyte interphase in Li-ion batteries, Electrochimica Acta 55 (2010) 6332-6341.
[63] M.D.L. D. Aurbach, E. Levi, A. Schechter, Failure and Stabilization Mechanisms of Graphite Electrodes, J. Phys. Chem. B 101 (1997) 2195-2206.
[64] Y.W. P.B. Balbuena, Lithium-ion batteries: solid-electrolyte interphase, Imperial College Press, 2009.
[65] G.V.Z. G. Chen, T.J. Richardson, G. Liu, P.N. Ross, Anodic Polymerization of Vinyl Ethylene Carbonate in Li-Ion Battery Electrolyte, Electrochem. Solid State Lett., 8 (2005) A344-A347.
[66] R.D. L. El Ouatani, C. Siret, P. Biensan, S. Reynaud, P. Iratbal, D. Gonbeau, The Effect of Vinylene Carbonate Additive on Surface Film Formation on Both Electrodes in Li-Ion Batteries, J. Electrochem. Soc., 156 (2009) A103-A113.
[67] S.J.H. K. Tasaki, Computational Study on the Solubility of Lithium Salts Formed on Lithium Ion Battery Negative Electrode in Organic Solvents, J. Phys. Chem. C, 114 (2010) 8076-8083.
[68] M.M.F. D.P. Abraham, S.-H. Kang, D.W. Dees, A.N. Jansen, Effect of electrolyte composition on initial cycling and impedance characteristics of lithium-ion cells, J. Power Sources, 180 (2008) 612-620.
[69] G.M.G. Whitesides, B., Self-assembly at all scales., Science, 295 (2002) 2418 - 2421.
[70] A.K.e.a. Boal, Self-assembly of nanoparticles into structured spherical and network aggregates., Nature, 404 (2000) 746-748.
[71] S.M. Iveson, Litster, J. D., Hapgood, K. & Ennis, B. J., Nucleation, growth and breakage phenomena in agitated wet granulation processes: A review., Powder Technol., 117 (2001) 3-39.
[72] S.e.a. Nijhawan, An experimental and numerical study of particle nucleation and growth during low-pressure thermal decomposition of silane., J. Aerosol Sci., 34 (2003) 691-711.

[73] A. Becker, Huttinger, K.J., Chemistry and kinetics of chemical vapour deposition of pyrocarbon—III—pyrocarbon deposition from propylene and benzene in the low temperature regime, Carbon, 36 (1998) 201-211.
[74] M.N.K. Obrovac, L. J., Reversible cycling of crystalline silicon powder., J. Electrochem. Soc., 154 (2007) A103-A108.
[75] H.C. Kim, J., Superior lithium electroactive mesoporous Si-carbon core-shell nanowires for lithium battery anode material., Nano. Lett., 8 (2008) 3688-3691.
[76] A.A. Zakhidov, Carbon structures with three-dimensional periodicity at optical wavelengths., Science, 282 (1998) 897-901.
[77] C.Y. Jiang, Markutsya, S., Pikus, Y. & Tsukruk, V. V., Freely suspended nanocomposite membranes as highly sensitive sensors, Nature Mater., 3 (2004) 721-728.
[78] Y.M. Kang, et al., Impedance study on the correlation between phase transition and electrochemical degradation of Si-based materials., Electrochemistry Communications, 9 (2007) 1276-1281.
[79] J. Shim, et al., Electrochemical analysis for cycle performance and capacity fading of a lithium-ion battery cycled at elevated temperature., Journal of Power Sources, 112 (2002) 222-230.
[80] I. Kim, P.N. Kumta, and G.E. Blomgren, Si/TiN nanocomposites - Novel anode materials for Li-ion batteries., Electrochemical and Solid State Letters, 3 (2000) 493-496.
[81] I.S.a.P.N.K. Kim, High capacity Si/C nanocomposite anodes for Li-ion batteries., Journal of Power Sources, 136 (2004) 145-149.
[82] J. Li, et al., Effect of heat treatment on Si electrodes using polyvinylidene fluoride binder., Journal of the Electrochemical Society, 155 (2008) A234-A238.
[83] Z.H. Chen, L. Christensen, and J.R. Dahn, Large-volume-change electrodes for Li-ion batteries of amorphous alloy particles held by elastomeric tethers, Electrochemistry Communications, 5 (2003) 919-923.
[84] L.B. Chen, et al., Binder effect on cycling performance of silicon/carbon composite anodes for lithium ion batteries., Journal of Applied Electrochemistry, 36 (2006) 1099-1104.
[85] H. Buqa, et al., Study of styrene butadiene rubber and sodium methyl cellulose as binder for negative electrodes in lithium-ion batteries., Journal of Power Sources, 161 (2006) 617-622.
[86] B.Z. A. Magasinski, I. Kovalenko, B. Hertzberg, R. Burtovyy, C.F. Huebner, T.F. Fuller, I. Luzinov, G. Yushin, Toward Efficient Binders for Li-Ion Battery Si-Based Anodes: Polyacrylic Acid, ACS Appl. Mater. Interfaces, 2 (2010) 3004-3010.
[87] O.D. Smidsrod, K. I., Alginates: chemistry and physical properties., Carbohydrates European, 14 (1996) 6-13.
[88] A.J.E. de Kerchove, M., Formation of Polysaccharide Gel Layers in the Presence of Ca2+ and K+ Ions: Measurements and Mechanisms, Biomacromolecules, 8 (2006) 113-121.
[89] D.J. I. Luzinov, P.D. Bloom, V.V. Sheares, V.V. Tsukruk, Bilayer nanocomposite molecular coatings from elastomeric/rigid polymers: fabrication, morphology, and micromechanical properties, Macromolecular Symposia, 167 (2001) 227-242.
[90] K.H. C.X. Liang, Improvements of the physical properties of fibroin membranes with sodium alginate, Journal of Applied Polymer Science, 45 (1992) 1937-1943.
[91] X.D. Fan, et al., Study on molecular interaction behavior, and thermal and mechanical properties of polyacrylic acid and lactose blends., Journal of Applied Polymer Science, 82 (2001) 1921-1927.
[92] N.M. Antonova, The Mechanical Properties of a Composite Coating with a Polymer Matrix Based on Sodium Carboxymethylcellulose and Aluminum Powder, Russian Journal of Non-Ferrous Metals, 50 (2009) 419-423.
[93] Z.H. Liu, P. Marechal, and R. Jerome, Blends of poly(vinylidene fluoride) with polyamide 6: interfacial adhesion, morphology and mechanical properties., Polymer, 39 (1998) 1779-1785.

[94] C.K. Chan, et al., Structural and electrochemical study of the reaction of lithium with silicon nanowires, Journal of Power Sources, 189 (2009) 34-39.
[95] M.N.a.L.J.K. Obrovac, Reversible cycling of crystalline silicon powder., Journal of the Electrochemical Society, 154 (2007) A103-A108.
[96] J.a.J.R.D. Li, An in situ X-ray diffraction study of the reaction of Li with crystalline Si, Journal of the Electrochemical Society, 154 (2007) A156-A161.
[97] M. Winter, The Solid Electrolyte Interphase-The Most Important and the Least Understood Solid Electrolyte in Rechargeable Li Batteries, Zeitschrift für Physikalische Chemie 223 (2009) 1395-1406.
[98] V.B.S. R. Grantab, Location- and Orientation-Dependent Progressive Crack Propagation in Cylindrical Graphite Electrode Particles, J. Electrochem. Soc., 158 (2011) A948-A954.
[99] J.C. H. Kim, Superior Lithium Electroactive Mesoporous Si@Carbon Core-Shell Nanowires for Lithium Battery Anode Material, Nano Lett., 8 (2008) 3688-3691.
[100] H.L.P. C.K. Chan, G. Liu, K. McIlwrath, X.F. Zhang, R.A. Huggins, Y. Cui, High-performance lithium battery anodes using silicon nanowires, Nature Nanotechnology, 3 (2008) 31-35.
[101] L.J.K. M.N. Obrovac, Reversible cycling of crystalline silicon powder, J. Electrochem. Soc., 154 (2007) A103-A108.
[102] H. Kim, B. Han, J. Choo, J. Cho, Three-Dimensional Porous Silicon Particles for Use in High-Performance Lithium Secondary Batteries, Angewandte Chemie-International Edition, 47 (2008) 10151-10154.
[103] R. Chandrasekaran, Magasinski, A., Yushin, G. & Fuller, T. F., Analysis of Lithium Insertion / De-Insertion in Silicon Electrode Particle at Room Temperature., J. Electrochem. Soc., 157 (2010) A1139-A1151.
[104] A.A. B. Hertzberg, G. Yushin, Deformations in Si-Li Anodes Upon Electrochemical Alloying in Nano-Confined Space, J. Am. Chem. Soc., 132 (2010) 8548-8549.
[105] P.D. A. Magasinski, B. Hertzberg, A. Kvit, J. Ayala, G. Yushin, High-performance lithium-ion anodes using hierarchical bottom-up approach, Nature Materials, 9 (2010) 353-358.
[106] N. Balke, Real Space Mapping of Li-Ion Transport in Amorphous Si Anodes with Nanometer Resolution, Nano Lett., 10 (2010) 3420-3425.
[107] A.J.A. U. Kasavajjula, Nano- and bulk-silicon insertion anodes for lithium-ion secondary cells, J. Power Sources, 163 (2007) 1003-1039.
[108] J.R.D. T.D. Hatchard, In Situ XRD and Electrochemical Study of the Reaction of Lithium with Amorphous Silicon., Journal of the Electrochemical Society, 151 (2004) A838-A842.
[109] R.B.L. J. Li, J.R. Dahn, Sodium carboxymethyl cellulose - A potential binder for Si negative electrodes for Li-ion batteries, Electrochemical and Solid State Letters, 10 (2007) A17-A20.
[110] J.S. Bridel, Azais, T., Morcrette, M., Tarascon, J. M. & Larcher, D., Key Parameters Governing the Reversibility of Si/Carbon/CMC Electrodes for Li-Ion Batteries., Chem. Mater., 22 (2010) 1229-1241.
[111] P.J. V.B. Shenoy, Y. Qi, Elastic softening of amorphous and crystalline Li–Si Phases with increasing Li concentration: A first-principles study, J. Power Sources, 195 (2010) 6825-6830.
[112] V.A. Sethuraman, In situ measurement of biaxial modulus of Si anode for Li-ion batteries, Electrochem. Comm., 12 (2010) 1614-1617.
[113] A. Magasinski, P. Dixon, B. Hertzberg, A. Kvit, J. Ayala, G. Yushin, High-performance lithium-ion anodes using hierarchical bottom-up approach, Nature Materials, 9 (2010) 353-358
[114] G.P. W. Oliver, An improved technique for determining hardness and elastic modulus using load and displacement sensing indentation experiments, J. Mater. Res., 7 (1992) 1564-1583.
[115] J.E.B. R. Rao, S. Ruffell, J.S. Williams, Nanoindentation-induced phase transformation in crystalline silicon and relaxed amorphous silicon, Microelectronics Journal, 38 (2007) 722-726.

[116] V. Domnich, Y. Gogotsi, S. Dub, Effect of phase transformations on the shape of the unloading curve in the nanoindentation of silicon, Applied Physics Letters, 76 (2000) 2214-2216.
[117] Y.G.G. A. Kailer, K.G. Nickel, Phase transformations of silicon caused by contact loading, J. Appl. Phys., 81 (1997) 3057-3063.
[118] Y.-T. Cheng, Verbrugge, M.W., Evolution of stress within a spherical insertion electrode particle under potentiostatic and galvanostatic operation, J. Power Sources, 190 (2009) 453-460.
[119] Y.-T. Cheng, Verbrugge, M.W., Diffusion-induced stress, interfacial charge transfer, and criteria for avoiding crack initiation of electrode particles, J. Electrochem. Soc., 157 (2010) A508-A516.
[120] R. Deshpande, Cheng, Y.-T., Verbrugge, M.W., Modeling diffusion-induced stress in nanowire electrode structures, J. Power Sources, 195 (2010) 5081-5088.
[121] T.K. Bhandakkar, Gao, H.J., Cohesive modeling of crack nucleation under diffusion induced stresses in a thin strip: Implications on the critical size for flaw tolerant battery electrodes, Int. J. Solid Struct. , 47 (2010) 1424-1434.
[122] R.E. Garcia, Chiang, Y.-M., Carter, W.C., Limthongkul, P., Bishop, C.M., Microstructural modeling and design of rechargeable lithium-ion batteries, J. Electrochem. Soc., 152 (2005) A255-A263.
[123] J. Christensen, Modeling diffusion-induced stress in Li-ion cells with porous electrodes, J. Electrochem. Soc., 157 (2010) A366-A380.
[124] A.F. Bower, Guduru, P.R., Sethuraman, V.A. , A finite strain model of stress, diffusion, plastic flow, and electrochemical reactions in a lithium-ion half-cell, J. Mech. Phys. Solids, 59 (2011) 804-828.
[125] G.A.C. Buxton, C. M.; Cleaver, D. J. , A lattice spring model of heterogeneous materials with plasticity, Modelling and Simulation in Materials Science and Engineering 9(2001) 485.
[126] B.K. Gupta, Bhushan, B. , Micromechanical properties of amorphous carbon coatings deposited by different deposition techniques, Thin Solid Films, 270 (1995) 391-398.